Downscaling silicon resonant MEMS and NEMS sensors: devices, transduction, non-linear dynamics and applications

Sébastien Hentz

INSTITUT NATIONAL des SCIENCES APPLIQUÉES de LYON

HABILITATION A DIRIGER DES RECHERCHES

Discipline: Mécanique / Physique

présentée par

Sébastien HENTZ

le 5 septembre 2012

Titre:

Downscaling silicon resonant MEMS and NEMS sensors: devices, transduction, non-linear dynamics and applications

---

JURY

M. Skandar Basrour	**Professeur UJF Grenoble**	**Rapporteur**
M. François Berger	**Professeur UJF - CHU Grenoble**	**Examinateur**
M. Lionel Buchaillot	**Directeur de Recherche CNRS IEMN Lille**	**Examinateur**
M. Régis Dufour	**Professeur INSA de Lyon**	**Président**
M. Adrian Ionescu	**Professeur EPFL**	**Rapporteur**
M. Stephen Purcell	**Directeur de Recherche CNRS UCB Lyon I**	**Rapporteur**

Habilitation préparée au sein du CEA-LETI, MINATEC et parrainée par le Laboratoire de Mécanique des Contacts et des Structures UMR INSA-CNRS 5259.

Contents

[1] Details can be found in Hentz *et al.* (2007)
[2] Details can be found in Kacem *et al.* (2008*b*;*a*), Pinto (2009), Pinto *et al.* (2009), Colinet *et al.* (2009)
[3] Details can be found in Hentz *et al.* (2008*a*)
[4] Details can be found in Robert *et al.* (2009), Juillard *et al.* (2010), Kacem *et al.* (2012*c*)

[5] Details can be found in Colinet *et al.* (2010), Duraffourg *et al.* (2008), Ollier *et al.* (2012)
[6] Details can be found in Mile *et al.* (2010), Fanget *et al.* (2011), Arcamone *et al.* (2011), Bargatin *et al.* (2012)
[7] Details can be found in Karabalin *et al.* (2009), Ivaldi *et al.* (2010; 2011*b*;*a*)
[8] Details can be found in Kacem *et al.* (2011*b*)
[9] Details can be found in Kacem *et al.* (2009), Kacem & Hentz (2009)
[10] Details can be found in Kacem *et al.* (2012*b*; 2011*a*)
[11] Details can be found in Kacem *et al.* (2010)
[12] Details can be found in Kacem *et al.* (2012*a*)
[13] Details will be found in Hanay *et al.* (2012)

Acknowledgement

Let me first say that the committee's careful review of my work has been duly appreciated. I thank all its members for the time they devoted to this process, doorway to a new phase for me.

This *Habilitation* work and all the activities described in this manuscript would not have been possible without the hard work of many students in the first place, and my sincere thanks go to them. I tried to cite all of them in the manuscript as they deserve, I hope I did not forget anyone.

It would not have been possible either without the help and expertise of many people, in many different fields: device physics, data processing, electrical measurements, electronics, CMOS co-integration, fabrication, but also the project leaders and program managers. Some of them will be cited along the following description, but many of them are not and I apologize for this. I would like to thank all of these people, as well as everyone I am working alongside daily in the group and in particular the fabrication persons, who are facing the "clean-room wall" every day so that people like me can have fun with new devices...

I would also like to thank the management for allowing me to pursue this *Habilitation*, and in particular Marc for giving me the right incentive to start writing.

My thanks go as well to our Life Sciences close partners, Christophe Masselon from IRTSV, F. Berger and A. Bouamrani from Clinatec.

Long-standing partnerships had obviously a tremendous influence on the orientation of my work: I would like to thank Pr. Régis Dufour and Sébastien Baguet from INSA-Lyon, Pr. Lionel Buchaillot and Bernard Legrand from IEMN, Pr. Claude-Henri Lamarque from ENTPE-Lyon, Pr. Michael Roukes from Caltech for welcoming me in his group as well as the NEMS-MS team there: Akshay Naik who was a great support, Selim Hanay and Scott Kelber.

Special thanks to Ben and Pedro for their careful proof-reading of the manuscript.

From a more personal point of view, I would like to thank my first son for his patience during the writing time, and of course my wife who did everything she could so that I would write quietly, including waiting for the end of the drafting to give birth to our second son.

Chapter 1

MEMS sensors go nano: general introduction [1]

A large part of the activities described in what follows circle around a small number of questions: what is downscaling beneficial to in sensing? What is the technical and scientific price one has to pay for downscaling? From a general point of view and at a very different scale, those are considerations close to the ITRS roadmap for "More Moore" in the MOS field, and the tremendous research efforts and scientific challenges demanded by the continuity of the Moore's law. Although the sensing field may be included in the so-called "More-Than-Moore" movement, its evolution has been much less formalized than its MOS counterpart. This document will try to show how my activities modestly contributed to this dispersed effort. As an introduction, a first study will be briefly described in this chapter, study which was seminal for those activities as well as which of the group. A number of scientific issues appear along this study: device physics, device structure, transduction, noise modelling, non-linearities. It is a good way to introduce how the document is structured: this is the work of a team, and the –at least partially– chronological order is nothing but a logical way to describe how this work have been part of the evolution of a team's work.

[1] Details can be found in Hentz *et al.* (2007)

1.1 Introduction

Although MEMS history is not so ancient, I will not go into a full review of it, whether in technological, applicative, or design terms. My contribution in the field has started with my hiring at LETI, more or less concomitantly with the publication of Hierold (2004), from whom I borrowed the title of the current chapter. This was a time when the Institute was deeply evolving, growing fast, moving to 24/7 200mm and 300mm wafer process platforms, aiming at low-cost, large volume markets. The MEMS teams had then easy access to up-to-date microelectronics (MOS) tools, with the associated critical dimensions. As taught to students in every VLSI process lecture, cost reduction means size reduction in collective fabrication. Of course, reality shows that the individual operations of assembling with an ASIC and chip-level packaging may represent up to 80% of the price of one device. Soon the possibility of fabricating the MEMS part with microelectronics tools or even better, on actual MOS lines started the quest for a holy grail, the all-integrated system : MEMS and ASIC fabricated on the same die with one process flow and line, including a wafer-level packaging. This is of course a still open quest nowadays, even if impressive progress has been made technology-wise.

One of the first MEMS devices prototyped within this new platform, compliant with the low-cost, large volume market and successfully transferred to the industry was a famous (at least inside LETI) capacitive accelerometer (fig 1.1). Famous and successful because canonical : it was rooted in the large background of LETI in inertial sensing ; as it is an airbag accelerometer, it aimed at a typical large volume market: automotive. It was fabricated on 200mm lines, used wafer-level packaging, but the minimum feature size was around $1\mu m$ (with thickness equal to $20\mu m$), well above what was possible with e-beam lithography.

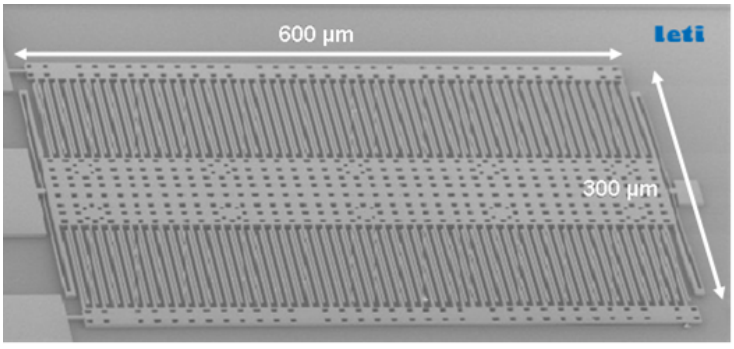

Fig. 1.1 – MEMS accelerometer from LETI cleanrooms in 2002

Within the FP6 MIMOSA project, the sensor group designed an accelerometer which was the result of basically homogeneously shrinking the existing device by orders of magnitude down to process limits (minimum feature size 50nm, thickness 160nm), with no change in operation principles : it still used interdigitated finger combs, differential capacitive readout to transduct the displacement of a suspended and holey (for release) mass, as shown figures 1.2 and 1.3.

The main motivation for fabricating such a device was merely that the means to do so was at hands... Of course, scaling laws are easy to perform : α being the geometrical scaling factor, the sensitive mass scales like α^3, the suspension stiffness scales like α, hence the resonance frequency ω of the equivalent second order oscillator scales like α^{-1}. On the other hand, the total readout

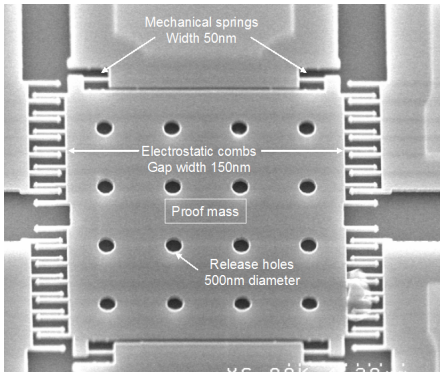

Fig. 1.2 – The Mimosa accelerometer

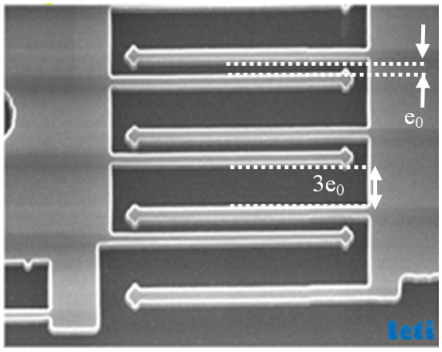

Fig. 1.3 – Zoom on interdigitated fingers

capacitance C_0 scales like α, the mass displacement per unit acceleration scales like $\frac{1}{\omega^2} \propto \alpha^2$ and hence the structure sensitivity in terms of ratio relative capacitance variation over acceleration scales like $\frac{1}{e_0\omega^2} = \alpha$ (where e_0 is the capacitance finger gap). A size reduction of two orders of magnitude will then lead to two orders of magnitude reduction in signal (absolute capacitance) but more importantly, two orders of magnitude reduction in sensitivity. The latter makes it difficult for such a NEMS device to compete with existing and commercial devices, assuming it would produce a decent readout output in the first place. First of all, preliminary experiments showed us it was extremely difficult to measure any capacitance variation at low displacement, or even obtaining a precise value of the total capacitance (around 10fF), due to background noise and parasitics. Secondly, as it was really difficult to understand the response of the structure, questions regarding scale effects arose : at these dimensions, can we still neglect the proximity forces between movable parts? Can we still neglect the geometrical or electrical non-linearities in the design of such NEMS devices?

This is where the scientific fun began ; these considerations imposed a large part of the technological roadmap of the sensor lab, and also a large part of the scientific contribution of its design team, at the time namely my colleague Laurent Duraffourg and myself.

1.2 Modelling

The structure schematic is shown figure 1.4. Compared to the usual and simple model used to design such a device, we added almost naively two ingredients to find out whether or not they could explain the observed behaviour: the mechanical non-linearities as well as proximity (Casimir) forces.

Second Newton equation is applied in the non-galilean referential frame of the substrate to the ensemble holey mass+fingers to give the following simple lumped model:

$$M\ddot{x} = M\gamma + F_{stiffness} + F_{elec} + F_{Casimir} \tag{1.1}$$

where x is the displacement of the mass relatively to the fixed combs, γ is the to-be-measured acceleration of the substrate in the assumed Galilean earth frame, F_{elec} is the electrostatic force applied by the combs, $F_{stiffness}$ is the displacement dependant force applied by the flexure beams, and $F_{Casimir}$ is the Casimir force involved in the combs.

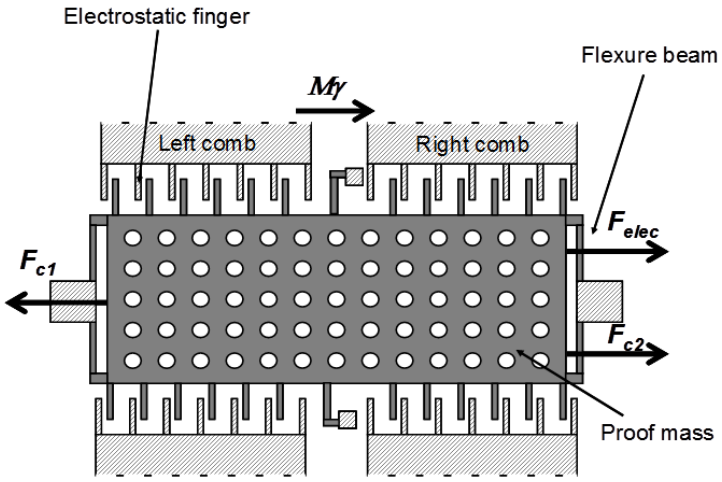

Fig. 1.4 – Schematic and notations for modelling of the Mimosa accelerometer

We have used the usual parallel plate expression for the electrostatic force, considering each finger pair was a parallel plate pair and neglecting the fringing field effect. The following sections describe the other forces.

1.2.1 Non-linear stiffness

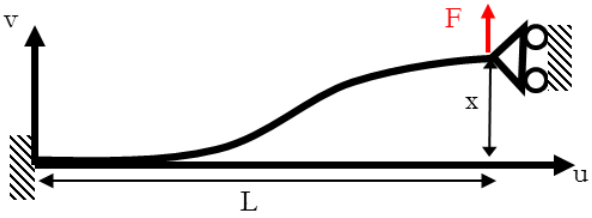

Fig. 1.5 – Model for a flexure beam, boundary conditions

Each flexure beam is assumed to follow the Euler-Bernoulli equation with large deflection stretching, with some amount of residual stress σ and the boundary conditions shown figure 1.5:

$$EI\frac{\partial^4 v(u)}{\partial u^4} - \left(\sigma S + \frac{ES}{2L}\int_0^L \left(\frac{\partial v(\xi)}{\partial \xi}\right)^2 d\xi\right)\frac{\partial^2 v(u)}{\partial u^2} = F\delta(u=L) \tag{1.2}$$

where E is silicon Young's modulus, I is the quadratic modulus, S the section area, δ is the Dirac function. In order to find an explicit solution for equation 1.2, the first linear modal shape has been used, satisfying $\frac{\partial^4 v(u)}{\partial u^4} = \lambda^4 v(u)$ as well as the boundary conditions of figure 1.5. After projecting equation 1.2 on this mode, we find:

$$F = 12.40\frac{EI}{L^3}x + 0.74\frac{ES}{L^3}x^3 + 1.22\frac{\sigma S}{L}x \tag{1.3}$$

This is the expression used for every flexure beam.

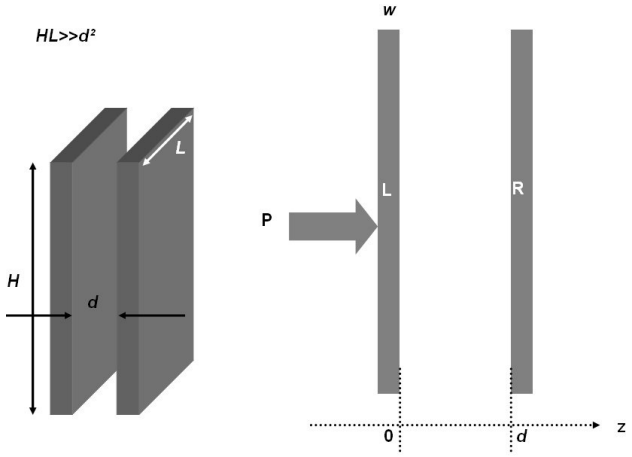

Fig. 1.6 – Two slabs in glance - 3D view and notation definition

1.2.2 Casimir force

The Casimir force is a macroscopic physical manifestation of the zero point energy. This force whose existence was theoretically predicted in 1948 by the Dutch physicist H.B.G Casimir (Casimir 1948) was precisely measured only in 1997 by the American team of S. Lamoreaux (Lamoreaux 1997). Between two uncharged infinite parallel plates with perfect conductivity, separated by a distance d, (see figure 1.6) this force per unit area has the following magnitude:

$$F_c = \frac{\pi^2 \hbar c}{240 d^4} \tag{1.4}$$

Actively studied for macro or microscopic structures (Lamoreaux 1998, Chen *et al.* 2002, Mostepanenko 2003), it is usually modeled for micro or nanosystems either by the ideal formula 1.4 or by an expression specifically defined for the metallic case (Serry *et al.* 1998, Ding *et al.* 2001) which in both cases clearly overestimates its impact for silicon NEMS. The corrections based on "metallic" Drude (relevant for gaps larger than 500nm, far above our NEMS dimensions) and plasma models (Ding *et al.* 2001) are not relevant since the intrinsic part of silicon is forgotten. The model used here and developed by L. Duraffourg takes explicitly into account the finite conductivity of the material as well as the finite thickness of the slab.

On the other hand, the effect of the rugosity (etched walls of the silicon fingers) has been neglected, which was validated thanks to a correction model (Bordag *et al.* 1995). It is also the case for temperature, as the dimensions considered are much below the thermal wavelength equal to $7\mu m$ at ambient temperature (Genet *et al.* 2000).

The model uses a corrective factor to account for finite conductivity and width, defined as:

$$\eta = \frac{\langle \hat{P} \rangle}{F_c} \tag{1.5}$$

where P is the resulting radiation pressure on the cavity. See (Lambrecht *et al.* 2007, Duraffourg & Andreucci 2006) for details on the computation of this factor, as well as the model and its results in general. For the sake of clarity, the corrective factor η is plotted figure 1.7 versus gap d for gold and high doped silicon, in the case of thin and thick slabs. One should notice that the model clearly shows the large influence of the gap, thickness and doping level and thus their potential importance in the NEMS design.

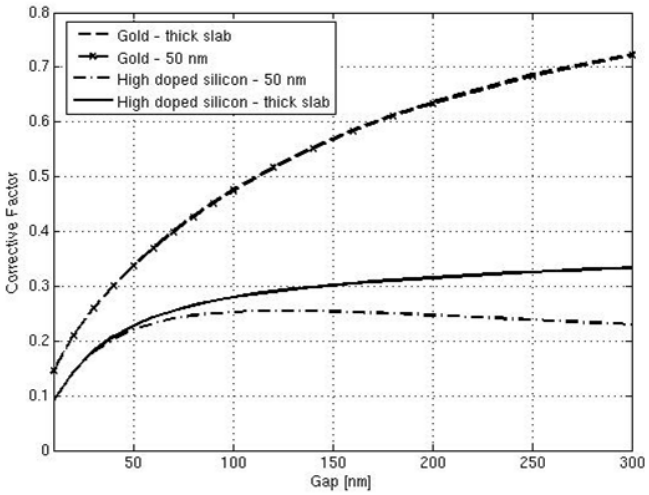

Fig. 1.7 – Corrective factor versus gap for gold and high doped silicon ($10^{20} cm^{-3}$), in the thin and thick slab cases

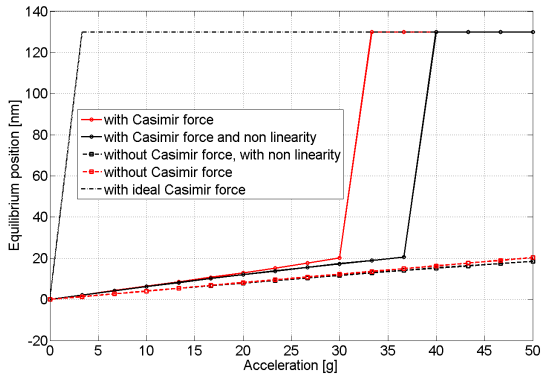

Fig. 1.8 – Equilibrium position versus acceleration for different models

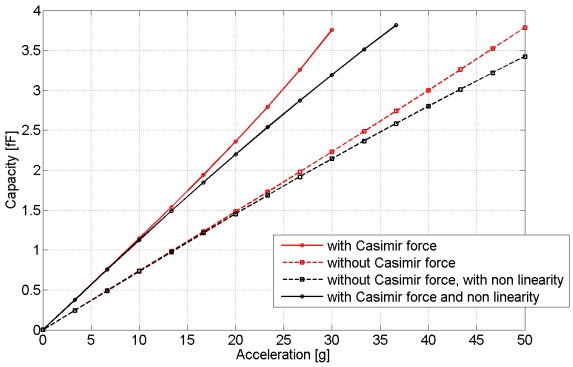

Fig. 1.9 – Capacitance variation versus acceleration for different models

Having shown the potential importance of the Casimir effect with finite conductivity and thickness in our dimension range, the model can be applied to our structure, with the strong assumption that each pair of fingers is a finite slab pair, and that the Casimir force is additive. The global mass equilibrium equation 1.1 is highly non-linear (cubic NL in the stiffness term, and fourth order NL term in the denumerator of the Casimir term) and has been solved by a robust algorithm based on the bisection method.

Figure 1.8 shows the mass equilibrium position versus acceleration for different models. One can firstly note that the use of an uncorrected Casimir model would lead to the conclusion that no stable position could be found. Experiment proves this wrong, as no such instability issue has been encountered. On the other hand, introducing the Casimir effect reduces the sensor dynamic range (as pull-in instability is observed before 50g), which must clearly be taken into account in the design. When also taking into account mechanical non-linearities, this dynamic range increases slightly. Figure 1.9 shows the capacitance variation versus acceleration. The same conclusions may be drawn, and the signal linearity can be better observed than on Figure 1.8. In particular, the stiffening behavior of the mechanical non-linearity is clearly shown, competing with the softening

behavior of the Casimir effect, finally improving the overall linearity when both effects are accounted for.

1.3 Experimentation

Characterization of the device consisted in capacitance variation measurements while varying the mass position by applying a DC voltage in a dedicated prober. Of course, considering the very weak nominal capacitance and variation range before pull-in, the size and fragility of the device, great care had to be taken in shielding the device, in preventing its pollution during operation and in calibrating all parasitic impedances to avoid collapse of the device and to obtain reproducible and reliable measurements. A high frequency voltage – above 1/f corner frequency – was used for capacitance measurement.

Preliminary results are displayed figure 1.10 for a stiff component which was less sensitive to electrostatic shock. The nominal capacitance was measured at 13.26fF, whereas its theoretical value is 13.62fF, which is an unexpectedly good measurement for such a small value. The capacitance variation is roughly equal to 40af (full range), and it seems that the overall noise floor is below 1aF, which confirms the quality of the measurement procedure. The same figure shows the comparison between the experimental data and our model including Casimir force and electrostatic and mechanical non-linearities. It also clearly shows the large influence of the residual stress value, even at low levels, in the structural layer. The latter has been found experimentally to be below the measurement resolution, i.e. roughly 10MPa.

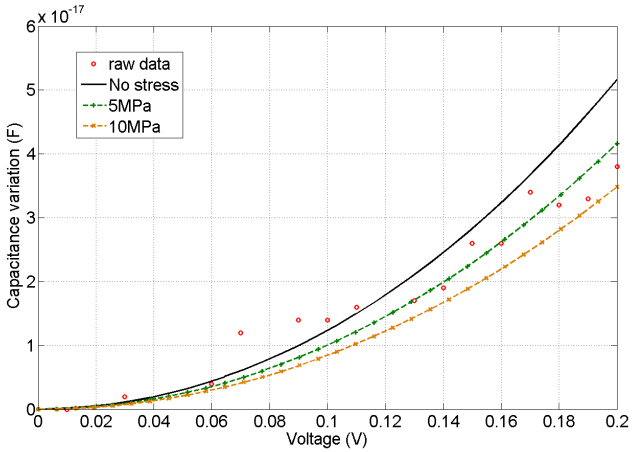

Fig. 1.10 – Experimental data versus model results

1.4 Conclusion and organization of the manuscript

This very first, crude, NEMS attempt in the group produced rather partial results, and raised more questions than they answered. This said, this technology-pushed study was a valuable learning experience, and paved the way for the following years of technological developments and scientific work of the team: at those scales, parasitics become of such a tremendous importance that it is necessary to reduce as much as possible the capacitances between the readout transduction and

the first amplification stage, by changing the paradigm of an ASIC bonded to the mechanical structure: the need for integration became obvious. The same change of paradigm is needed as far as transduction goes: the loss of gain and sensitivity when size decreases needs to be compensated for by the use of transduction principles adapted to the size of the devices. In any case, signals are so weak that a great deal of work had to be performed about noise, its modelling, and its reduction in measurement chains. Finally, even if theory shows that proximity forces are of importance, there never really was a compelling evidence of their experimental observation in our devices (Recent studies have shown such evidence, with more suitable, larger, real-life devices providing for a useful signal (Ardito *et al.* 2011)). On the other hand, experience quickly showed that non-linearities should be dealt with as it would become increasingly harder to avoid them at smaller scales.

This manuscript, divided in four main chapters before some perspectives are given, more or less follows an application-driven structure, as an excuse to describe scientific advances in different fields: downscaling, characterization methods, mechanical structure, non-linear dynamics, transduction for individual devices as well as arrays, noise issues: the first chapter, *Downscaling resonators and inertial sensors*, will describe some of the scientific challenges and advances due to the size reduction of resonators in the context of inertial sensing. This chapter deals with relatively applied activities but beyond know-how acquisition, this work initiated noise studies in our group; it was also transformative for our activities which resolutely turned towards true NEMS. The second one, *VLSI NEMS, transduction and applications*, will describe some of our NEMS devices and their best-suited applications. It explores various transduction types we investigated specifically for those dimensions, as well as the possibility to operate NEMS in large arrays. The third chapter deals with *Non-linear dynamics of MEMS and NEMS*, describing our motivations to work in this field and suggesting ways to increase NEMS dynamic range. Finally the last chapter entitled *NEMS Mass Spectrometry, mass resolution and device noise* describes on-going studies in the biological field and opens the discussion on near future activities before discussing some envisioned research perspectives.

Chapter 2

Downscaling resonators and inertial sensors

2.1 Introduction

As already pointed out, the fabrication means of LETI aim at large volume market devices. Key requirements for the consumer market in particular are of course the cost, low power consumption and supply. Technically, this means a good "accuracy" (which is translated into different specs from manufacturer to manufacturer: resolution or limit of detection or noise density, over as large a bandwidth as possible, and for a given full measurement range) with the highest number of functionalities (number of sensitive axis, electronics included, self-test...) in a very small package, a device easily manufacturable in large volumes with a good yield and an easy integration. A canonical example is the capacitive STm LIS3L02AL accelerometer which has been chosen to equip the Nintendo Wii console "Nunchuk" (game controller) in 2006: it is a 3$ device, $5 * 5 * 1.6mm^3$ package including a 3-axis sensor with analog electronics, 3.3V power supply, with a consumption of around 1mA, +/-2g full range with $50\mu g.Hz^{-1/2}$ resolution over 1.5kHz bandwidth, processed on 200mm wafer lines. In 2010, very similar performances are obtained from the same manufacturer with $3 * 3 * 1mm^3$ package (hence cheaper), including digital electronics, and still based on a capacitance variation measurement. This fast evolution is mostly the result of software changes (Application-Specific Integrated Circuit, ASIC), and not of the process or mechanical structure.

Interestingly, in this application category, the absolute precision does not seem to be an important criterion (sensitivity in V/g may be given with a +/-10% tolerance), and the Limit Of Detection ("LOD", sometimes called resolution) is not the most important requirement. This is not the case for other, more traditional, applications like automotive or navigation, which may be extremely demanding in terms of absolute precision and resolution. Research efforts turned these industrial requirements into a quest for the best acceleration noise floor, see figure 2.1. Of course this figure of merit should be pondered by the size of the mechanical structure. As an example, the work of Chae *et al.* (2004) displays a few mm^2 mechanical structure, as opposed to an order of magnitude lower for the LIS3L02AL.

As can be seen, until the study stops in 2005, most of the transduction principles used here are capacitive. Similar data after 2005 is scarcer, probably because capacitive detection had reached industrial maturity (and left little room for improvement), certainly because the emergence of

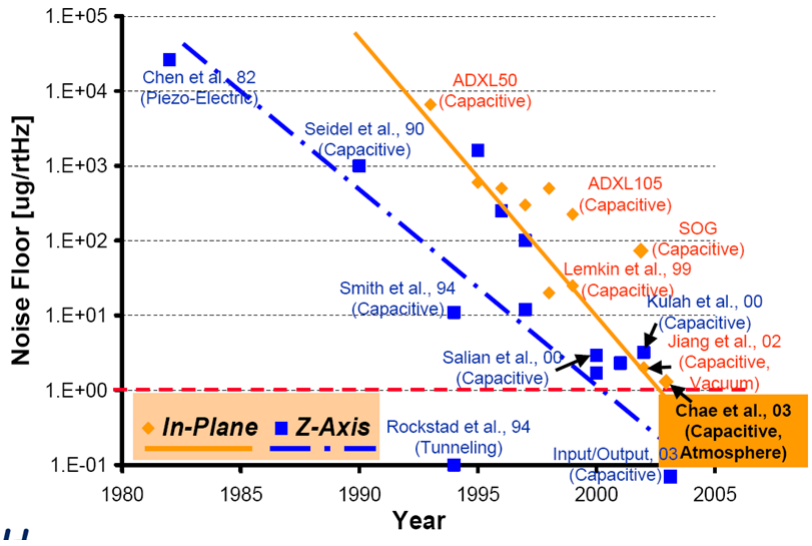

Fig. 2.1 – Accelerometer performances in the litterature

new markets modified the interest for the LOD figure of merit: rather than decreasing cost, the industry was looking for added-value in its sensors: more functionalities (multi-axis sensors, multiple measurands) for the same or slightly higher cost. There was a need for a change in transduction.

Resonant detection is not new of course, and one can cite the work of the ONERA (Le Traon *et al.* 1998), designing high performance accelerometers for navigation applications, mostly piezo-electric, with total size of a few cm and minimum feature size of around $100\mu m$. After having explored different materials (Le Traon *et al.* 2005), the same team (Le Foulgoc *et al.* 2006, Le Foulgoc 2008) went to silicon and an electrostatically actuated resonator to decrease size and cost while retaining high performances, to reach a total size of around a few mm^2 with minimum feature size of a few μm. One can also cite Seshia *et al.* (2002) whose work displays a differential resonant accelerometer with a noise floor of $40\mu g.Hz^{-\frac{1}{2}}$ and a few mm^2.

This chapter will describe first scientific and technical studies in the fields of transduction, characterization methods, technology and noise modelling. From the applicative point of view, those efforts were produced towards the development of LETI's first resonant accelerometer, fabricated on 200mm wafer lines in monocrystalline silicon, with consumer market requirements and in particular with a mechanical footprint less than $0.5mm^2$. This work has been funded by the FP7 MNT-Europ project, and by the French Research Agency (ANR) M&NEMS and NANORES projects.

2.2 $4\mu m$ SOI accelerometers [1]

This work was partly funded by the FP7 MNT-Europ project from 2005 to 2008. Valérie Nguyen was the project leader, and Marie-Thérèse Delaye was in charge of the fabrication.

This was our first attempt in resonant detection, moreover with relatively small MEMS. We started from scratch (with my distant background) with very basic experiments to quickly evaluate the difficulties. This did not give rise to high level science, but rather explored technical challenges. I thought it was still interesting to describe them in the context of this manuscript, as it shows the

[1] Details can be found in Kacem *et al.* (2008*b*;*a*), Pinto (2009), Pinto *et al.* (2009), Colinet *et al.* (2009)

considerable distance we covered from there, with the help of several students.

2.2.1 Process

Preliminary choices made for this first attempt were based on the empirical knowledge of the known working "operation point", the Freescale accelerometer (see Figure 1.1), with slightly reduced dimensions.

The process is described table 2.2.1 : it starts with 200mm SOI, 0.4μm <100> wafers. The top layer is epitaxied to 4μm and doped in-situ to reach a few $m\Omega.cm$. The MEMS level is then RIE etched to define the resonator, sensitive mass, electrodes, anchors and suspensions. Then the silicon is protected by a TEOS oxide layer, before AlSi is deposited for pads and leads. The last step is vapor-HF etching for release.

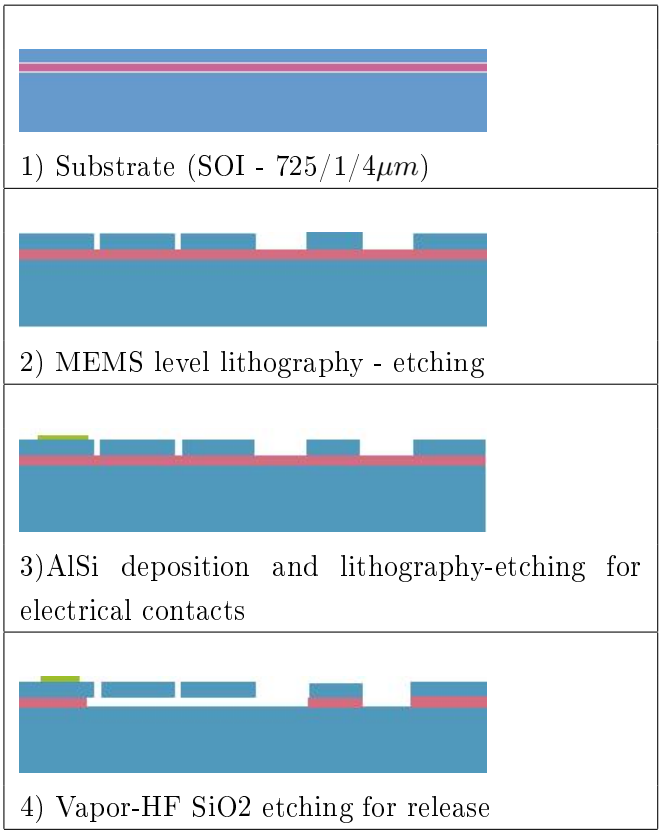

Table 2.1: Process for the MNT-Europ accelerometer

2.2.2 Mechanical structure

First studied designs are shown figure 2.2. The sensitive mass is anchored via flexible suspensions to the substrate and when undergoing a $\underline{y}$ acceleration, applies a longitudinal force on the beam resonator, hence changing its resonant frequency. The suspension has to be flexible enough so the mass can actually move to apply a force, but stiff enough so that the first mode of the mass (usually out of plane) is far above the required bandwidth of the resonator, and so that the structure survives a shock. The suspension also has to be aligned with the centre of gravity of the mass in the $\underline{x}$ direction, to reduce as much as possible the cross-sensitivity (non null read-out under an

acceleration on a transversal axis). Also, the distance between the resonator and the suspension plays the role of lever arm and should be as low as possible to enhance the sensitivity. In order to save time and to not delay the fabrication, a DOE has been defined to test different configurations of mass, stiffness of suspensions, distance suspension/resonator and resonator frequency. Typical mass dimensions vary from 50 to 200μm.

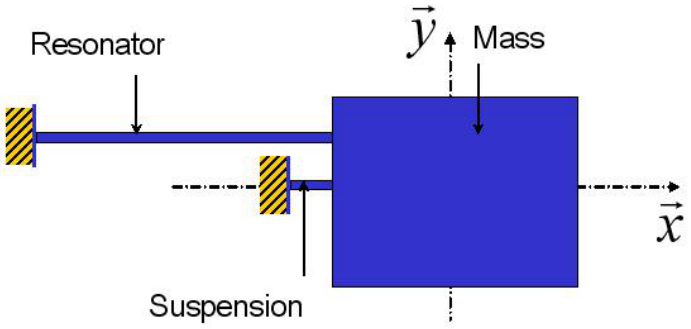

Fig. 2.2 – Simple accelerometer shematic

This design has two drawbacks : first of all, it is greatly advantageous to use a differential readout, that is to say to use two resonators undergoing forces of inverse sign, for both increased linearity and insensitivity to external perturbations (like temperature changes). This can be done either by using two beam resonators on one mass, see figure 2.3, or two similar accelerometers like figure 2.2, but placed head-to-tail. Indeed, if the frequency shift of one resonator is expressed by $\Delta f = a_0 + a_1\gamma + a_2\gamma^2 + ...$, then we have $\Delta f_1 - \Delta f_2 = 2a_1\gamma + 2a_3\gamma^3 + ...$ Non linear terms of even orders vanish, the sensitivity remains linear in much wider acceleration range. Likewise, when both resonators are submitted to the same perturbation (temperature or hygrometry change, ...), their frequency shift should be identical, so their difference is zero. Like for any other sensor, differential measurement is a way to sort out the quantity to be measured among others. In the resonant case though, there is an unavoidable blind zone, due to the lock-in phenomenon (Le Traon *et al.* 2005): the two resonator vibrations are locked in phase because of an acoustic coupling via the substrate, or even the structural layer, and they will only decouple when the two opposite forces applied on them reach a particular threshold. Several precautions may be taken to reduce the coupling : both resonators should not be too close to each other, their anchors should not be directly linked via the structural layer, or a decoupling frame might be used (see Le Traon *et al.* (2005) for example).

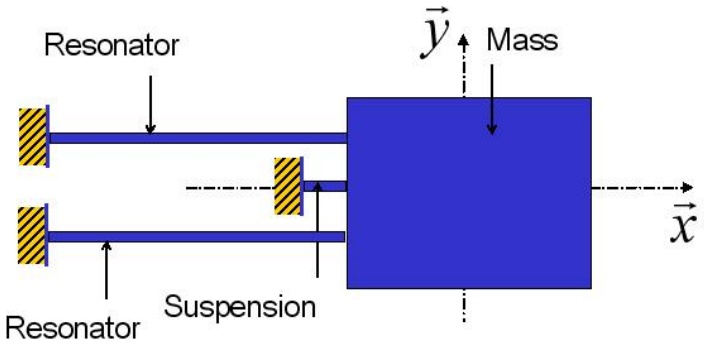

Fig. 2.3 – Differential accelerometer

Secondly, the mass motion is not a perfect rotation around a fixed point, but the suspension bends and stores strain energy which becomes useless to stress the resonator, decreasing the sensitivity. These considerations have led to propose the patented (Hentz *et al.* 2008*b*) design shown figure 2.4.

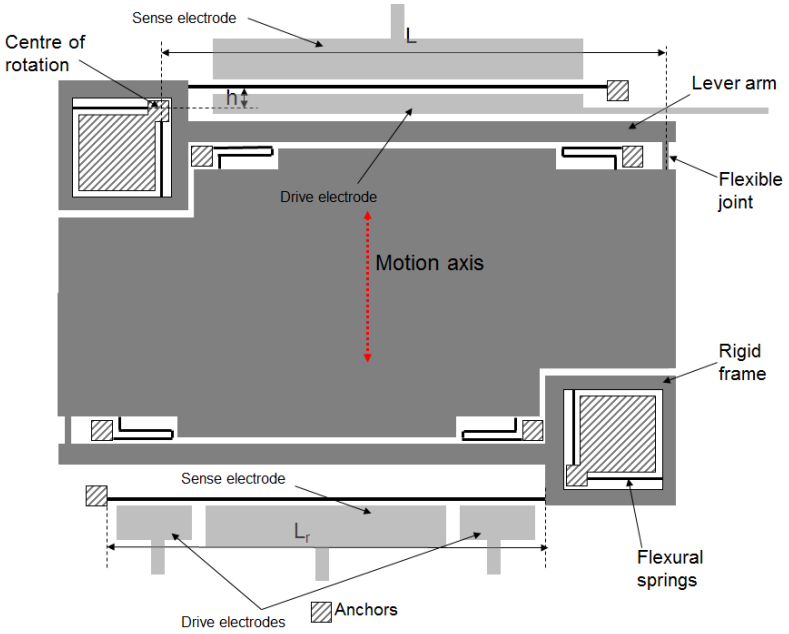

Fig. 2.4 – Improved accelerometer design ; Two different transduction means are shown.

This layout has several advantages:

- It shows a "built-in" differential measurement, with two resonators and one mass
- The sensitive mass motion is a translation, its suspensions already suppress transversal motions
- There is no constraint on the relative position of the resonator and of the mass centre of gravity.
- The link between the resonator and the mass is a rigid arm, in pure rotation : two orthogonal suspension beams are used instead of one ; as their longitudinal rigidity is much higher than their bending stiffness, the only motion left possible is a rotation around a very well controlled point : the intersection point of the two suspension beams. The distance from the resonator to this point can then be made as small as wanted, amplifying with a huge factor the mechanical force applied to the resonator
- it is extremely compact, ie very little surface consuming.

2.2.3 Resonator transduction

Acquiring the know-how for resonant sensing has been a long and difficult process in the context of decreasing the size of the structures. Preliminary structures were fabricated on 4μm SOI wafers, with minimum feature size of 500nm. This seems relatively large compared to nowadays NEMS

devices, but in the context of obtaining a real-world device, it was very challenging as it was close to state of the art research studies (Seshia *et al.* 2002), and far below any commercial resonant device. The electrostatic actuation and capacitive detection have been chosen *a priori*: it was very well known, at least for static (or quasi-static) detection, noiseless, and very easy to fabricate, with no extra materials or mask level requirement; moreover it allows for flexible, in-plane designs which only demands gaps etching in the silicon layer.

Frequencies have been chosen relatively low, between 50 to 500kHz with the goal of developing the necessary experimental set-up and procedures. The idea was to work above the 1/f noise corner frequency of the electronic, but also to facilitate the electrical measurement: figure 2.5 shows the equivalent electrical circuit of a one-port capacitive resonator (only one electrode for actuation and detection).

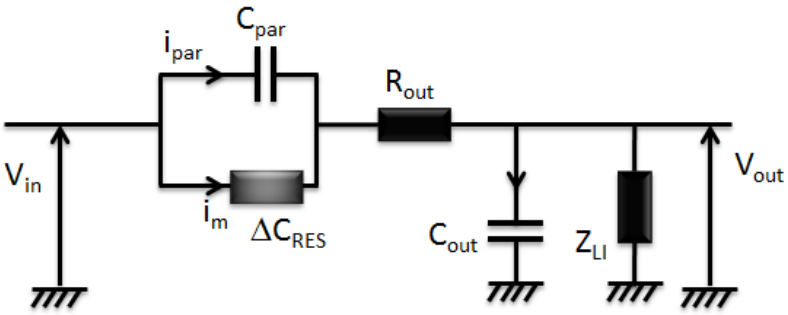

Fig. 2.5 – Small signal schematic of a 1-port capacitive resonator

C_{par} is the parallel "static" capacitance of the resonator at rest, plus an eventual feedthrough capacitance usually negligible in this scheme, in parallel of the device itself, producing the motional current i_m due to the capacitance variation ΔC. C_{out} is the output capacitance (pads, cables...) usually around a few 100pF (impedance below $10k\Omega$ at 100kHz), whereas Z_{li} is the readout device input impedance, typically a 25pF capacitance (impedance around 50 $k\Omega$ at 100kHz) in parallel with a $100M\Omega$ resistance. Neglecting Z_{li}, we have

$$V_{out} = \frac{1}{jC_{out}\omega}\left(i_m + i_{par}\right) = \frac{1}{C_{out}\omega}\left(V_{bias}\Delta C\omega + V_{in}C_{par}\omega\right) \propto \alpha \tag{2.1}$$

where V_{bias} is the DC voltage applied to either the electrode or the beam and α is the scaling parameter: C_{par} scales like the ratio surface over gap, hence like α. Assuming a constant displacement relative to the width of the resonator (consistent with the onset of non-linearities), ΔC also scales like α, ie like ω^{-1}. From this, it is easy to see the difficulty of capacitive measurements at high frequency : the motional current *ie* the useful signal remains constant while the higher the frequency, the more it flows into the output "parasitic" capacitance (which may be considered constant for a given process/readout), the output voltage (and hence the Signal-to-Noise Ratio SNR) linearly decreasing with frequency. Also, the useful signal is added to a "static" current i_{par}, which may be much higher than the useful signal itself ; this is an unwanted background from which the useful signal has to be extracted. They both remain constant with scaling, up to the point when the resonator static capacitance becomes lower than the feedthrough capacitance (parasitics), in which case it is harder and harder to obtain the useful signal, drowned in the background. This is the main reason why relatively low frequencies have been used in these preliminary designs.

The equivalent impedance of the resonator at resonance is a pure resistor, the motional resistance R_m, used as a figure of merit to characterize capacitive resonators (Rantakari *et al.* 2005):

$$R_m = \frac{k_{eff}}{\omega_0 Q \eta^2} \tag{2.2}$$

where k_{eff} is the effective stiffness of the resonator, Q its quality factor and η is the so-called transduction factor $\eta = \frac{V_{bias} C_0}{g}$ (g being the capacitive gap). The gap is at the fourth power in the motional resistance: it is the most important parameter in the capacitive transduction. Research efforts (mainly technological efforts) seek to reduce this motional resistance to a minimum level, eventually down to the commercial 50Ω impedance. The motional resistances of our devices are typically of the order of several $10's M\Omega$ with a few V, which is among the highest measured in the literature. Of course, this is not a very desirable feature and it underlines the challenge it is to even read a signal out of these devices. Bhave (2004) obtained a $4M\Omega$ device which proved impossible to characterize with direct measurement. Seshia *et al.* (2002) used very similar dimensions, frequencies and materials as ours, and had to use CMOS integration, 16V bias and finger combs to sense the resonator's motion.

2.2.4 Experimental characterizations

The electrostatic drive of the resonators were traditionally obtained by adding a DC voltage V_{bias} and an AC voltage V_{ac}. The force per unit surface is then proportional to:

$$F_{elec} \propto (V_{bias} + V_{ac}\cos(\omega t))^2 = V_{bias}^2 + \frac{V_{ac}^2}{2} + 2V_{bias}V_{ac}\cos(\omega t) + \frac{V_{ac}^2}{2}\cos(2\omega t) \tag{2.3}$$

The two first terms are a constant force term, responsible for a DC deflection of the beam (and hence for the change in the motional resistance or say differently, for a change in effective gap), as well as a negative stiffness (appearing in the equation of motion when performing a first order Taylor expansion of the $\frac{1}{(g-w)^2}$ term in the force expression (see chapter 4)). The two last terms are actuation harmonics, both used for measurement purposes. One usually uses the ω term as its amplitude is proportional to both DC and AC voltages: it is easier to produce a high DC voltage (which is desirable to increase the transduction factor η, see equation 2.2). When only one electrode is used for actuation and current detection is carried out through the resonator, the equivalent circuit is which of figure 2.5.

2.2.4.1 Direct electrical measurement

First attempts were performed by François Belmas, a Master student now PhD student close to graduation, with the resonator shown figure 2.6 and an impedancemeter for simplicity sake. An open circuit calibration procedure allowed for the suppression of one part of the background i_0. This scheme proved to hardly give any result. A great difficulty was a downside of the chosen low frequencies, as they meant very slendered beams at these dimensions: it was really tedious to release them without getting them stick to the electrodes, or stick during the experiment because of electrostatic shocks, or even simply with time when stored.

A rare result is shown figure 2.7, obtained with the stiffest resonator (theoretical resonance frequency 437kHz) with high voltages (above 5V DC). The response is highly non-linear and a

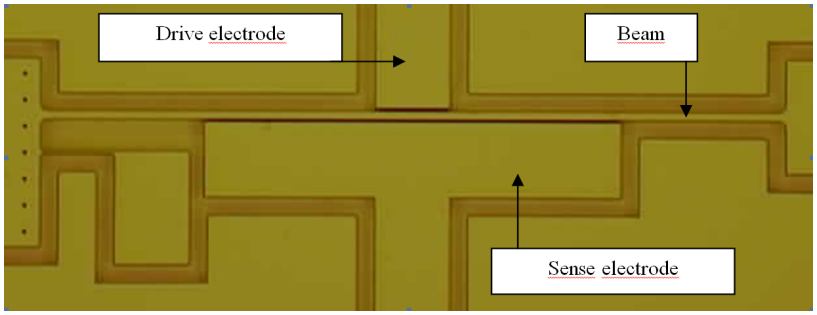

Fig. 2.6 – Optical microscope image of a $200\mu m$ long, $2\mu m$ wide resonator ; only one of the electrodes or both can be used.

100kHz above theoretical predictions. All peaks at lower voltages higher than the background were non-linear, hence its evolution with V_{bias} or V_{ac} could not be easily associated to any linear model: there was no clear signature of mechanical response. Very quickly appeared a need for observing the mechanical motion of the device to lift all doubts relative to the capacitive sensing.

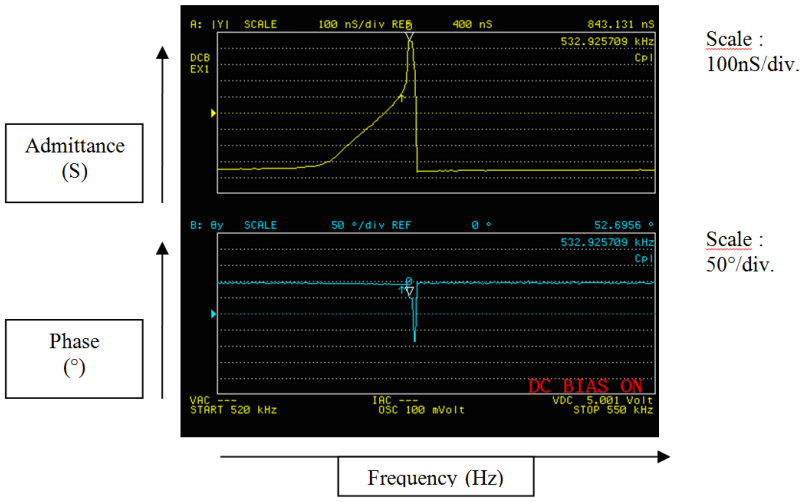

Fig. 2.7 – Frequency response obtained with the impedancemeter at ambient pressure

2.2.4.2 SEM set-up

This was part of the 18 months "Diplôme de Recherche Technologique" degree of Hervé Fontaine (Kacem *et al.* 2008*b*;*a*). Hervé has later been hired as a design engineer at ST Microelectronics. The idea was to perform the electrical characterization of the device, while observing it in an electronic microscope, that is to say in vacuum. A Scanning Electron Microscope was modified thanks to the help of Henri Blanc, technician in the laboratory to include a holder for a PCB board on which the device was bonded, plus a vaccum feedthrough for electrical connections (see figures 2.8, 2.9 and 2.10). This is a similar setup as in Gouttenoire (2009), designed for much smaller devices.

Figure 2.11 shows the bonded resonator inside the SEM chamber while applying a DC voltage to one electrode. The charge accumulation can be visualized by the color change. Again the impedance analyzer has been used to sweep the actuation frequency and observe the beam response. Mechanical resonance was observed thanks to a blurred image of the resonator, see figures 2.12 and 2.13, around

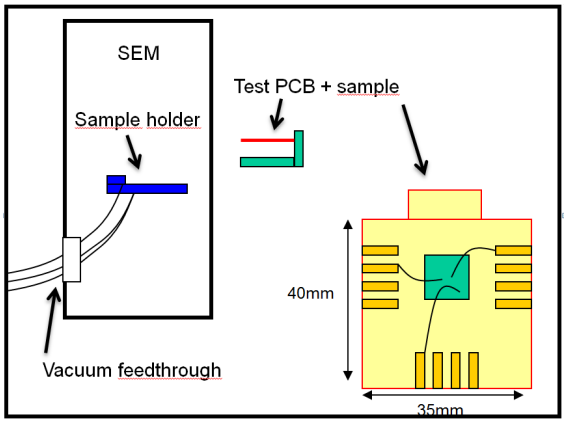

Fig. 2.8 – Schematic of the SEM setup

Fig. 2.9 – Sample introduction in the SEM setup

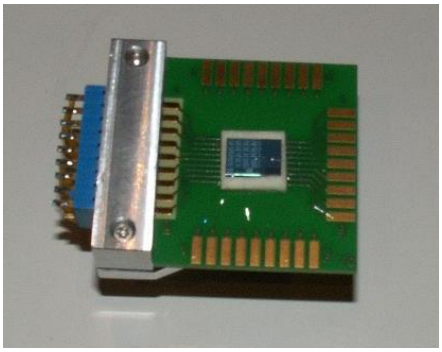

Fig. 2.10 – The PCB test board

the same frequency as the purely electrical measurement, 540KHz. Fabrication uncertainties could not explain such a discrepancy with the theoretical frequency (437kHz), but a residual tensile stress in the silicon top layer as small as 30MPa (within the manufacturer specs) could. Another Master student I advised, Galdric Sibiude, worked on the prediction of the stress state of our structures at the end of the process line, and showed that this value was consistent with the epitaxy step including in-situ doping.

Of course, such a set-up does not allow for simultaneous accurate electrical measurement and SEM observation: for example, self-oscillation of the device was observed when the electron beam was on because of accumulated charges (a similar phenomenon was studied by Gouttenoire (2009)). A significant difference in signal background was observed when the SEM was switched on or off. Nevertheless, this setup allowed us to clearly correlate electrical output with mechanical motion and decorrelate various perturbations, with only eye observation. We even observed the abrupt decrease in amplitude because of NL bistability, both electrically and with SEM images. This experiment clearly helped us in the understanding and in having confidence in our electrical measurements.

2.2.4.3 Stroboscopic optical microscopy

The team of A. Bosseboeuf and F. Parrain at l'Institut d'Electronique Fondamentale d'Orsay (IEF) works on original characterization methods for vibrating nanostructures. In the context of our collaboration funded by the NANORES project, they extended a method of stroboscopic optical microscopy both in the visible range, and in the deep UV range (for more details on this method,

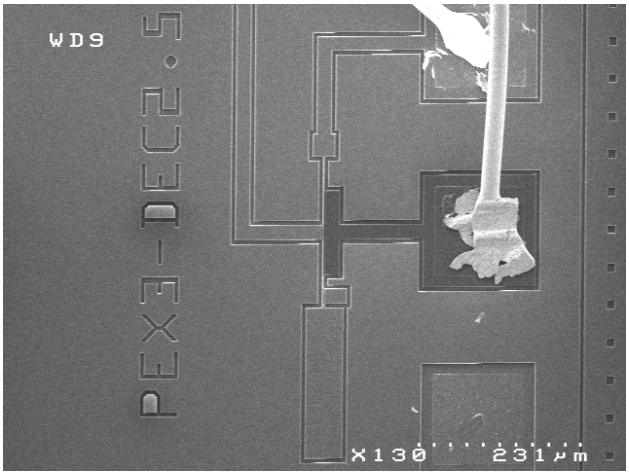

Fig. 2.11 – In-situ SEM picture of the device while applying a constant DC voltage of 10V on one electrode (darker on the picture)

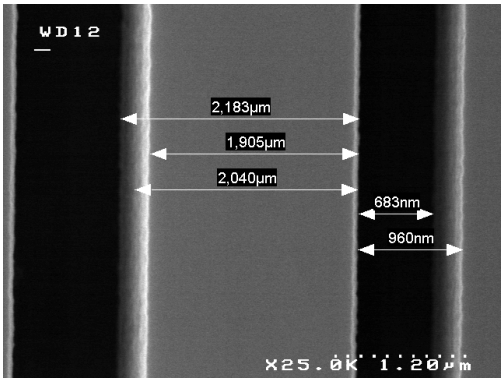

Fig. 2.12 – 438kHz-driven resonator ($1V_{DC}$, $1V_{AC}$) out of resonance

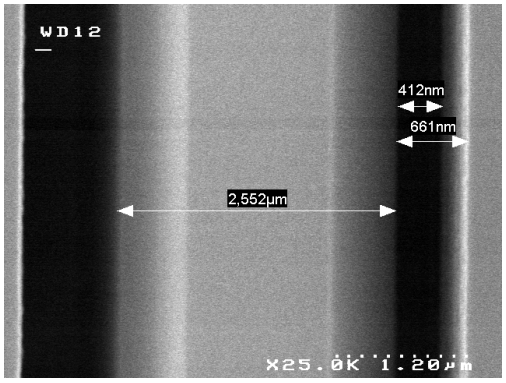

Fig. 2.13 – 440.6kHz-driven resonator ($1V_{DC}$, $1V_{AC}$) at resonance. The blurred area is the motion of the beam.

see (Le Foulgoc *et al.* 2006)). Figure 2.14 shows a typical frequency response obtained with our MNT resonator. Although interpretation of these measurements is not as straightforward as a direct frequency measurement, they do confirm that our device features a mechanical resonance, with both external piezoelectric and internal electrostatic actuation, with a relatively good quality factor (over 10000). The resonance frequency found is around 500kHz, below the electrical frequency (roughly 540kHz). This point was attributed to a stress induced by the clamping onto the holder, but would deserve more thinking. This technique showed a good enough – but not electrically out of reach – resolution (a few 0.1nm) so that it was possible for the first time to obtain a linear peak (with typically $1V_{DC}$ and less than $1mV_{AC}$). Although this piece of news made the resonator potentially useable for sensing purposes, its dynamic range was very narrow, the theoretical onset of non-linearity being around 30nm.

2.2.4.4 Low noise lock-in amplifier characterization

Those measurements were performed with the help of Bruno Reig, staff member in the group.

Through all the above preliminary steps, a good knowledge of the resonator has been gained: Mechanical resonance was definitely observed, and it was necessary to develop a setup with lower

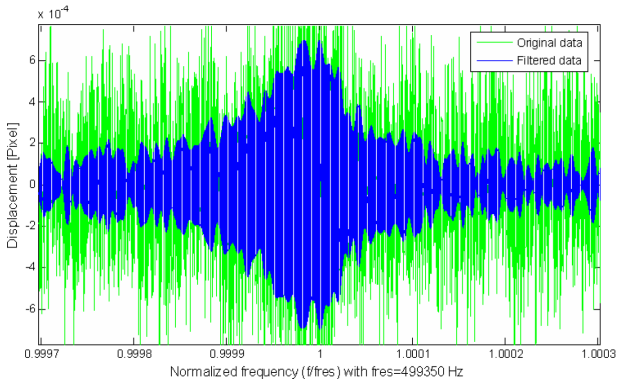

Fig. 2.14 – Frequency response of the resonator by optical stroboscopy

noise floor, and better impedance matching. We went back to purely electrical characterization with low-noise lock-in demodulation techniques, and we used both drive and sense electrodes (We thank Lionel Buchaillot's and Bernard Legrand's team at IEMN for useful discussions and preliminary experiments). AC voltage is applied to the drive electrode which generates the mechanical motion of the resonator, and DC voltage is applied to the beam itself, generating the motional current. The equivalent circuit becomes which of figure 2.15. The detection static capacitance adds up to the much higher output capacitance, and the parallel capacitance C_{par} in equation 2.1 becomes only the direct feedthrough drive-sense capacitance, much smaller than in the 1-port case. The background is then reduced in the total output current. To decrease it even more, we used two techniques:

- post-process background suppression: a measurement is performed with $V_{bias} = 0$. No motional current is produced, only the feedthrough one is measured. The vectorial substraction of the latter in the complex domain is carried out, from which only the motional signal remains.

- 2f measurement feature of the lock-in amplifier: this time the actuation force harmonics used is the 2ω one in equation 2.3. The electric signal in the actuation electrode is then an ω voltage, the resonator's displacement pulsation and hence the output signal is a 2ω harmonics. Direct feedthrough to the output is then reduced to its minimum. Before being multiplied by the output signal for baseband signal demodulation, the lock-in reference signal is obtained by doubling the frequency of the input voltage.

These tricks allow for a much better Signal-to-Background Ratio (SBR). As the dominant source of noise in the measurement chain is the Lock-In input noise here, reducing the cables length from around 1m to a few 10cm and thus reducing the output capacitance, helping with the impedance matching resulting in direct gain in the SNR (see equation 2.1).

Finally a typical 2f frequency response obtained with a 2MHz Signal Recovery LIA 7280 in a vacuum probe station is shown figures 2.16 and 2.17. The response is linear with very reasonable voltages, compatible with CMOS operation. The quality factor is extracted thanks to a Lorentzian fit and varies from 10000 with a few V DC to 30000 and more below 1V. The background is remarkably low (around 100nV), as is also observed in the close-to 180° phase jump at resonance. Noise measurements were very coarse at the time: the noise at resonance was evaluated from amplitude fluctuations out of resonance to roughly $10nV$ with 200ms integration time, that is to

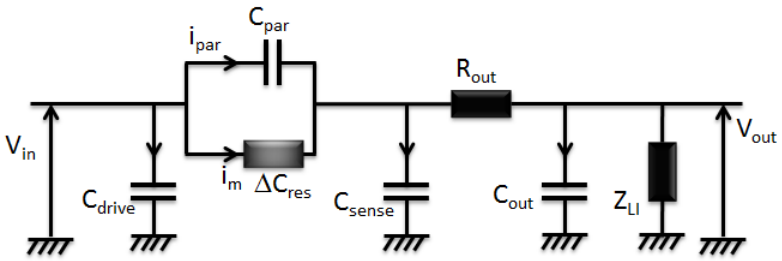

Fig. 2.15 – Small signal schematic of a 2-port capacitive resonator

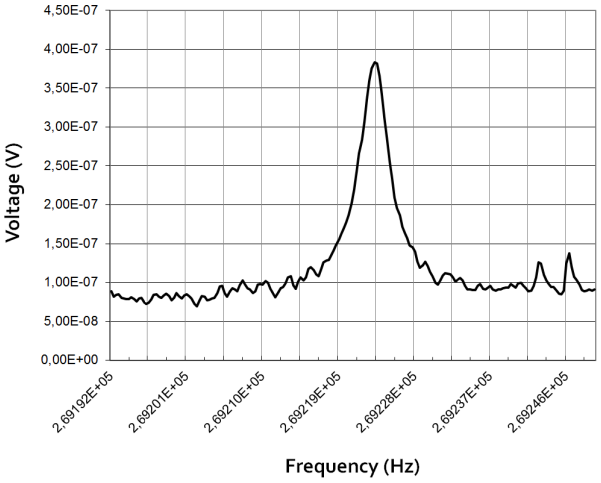

Fig. 2.16 – Amplitude frequency response of the MNT resonator, 2f measurement, $6V_{DC}$, $40mV_{AC}$ and 200ms integration time. The frequency is the drive frequency, half the motion frequency.

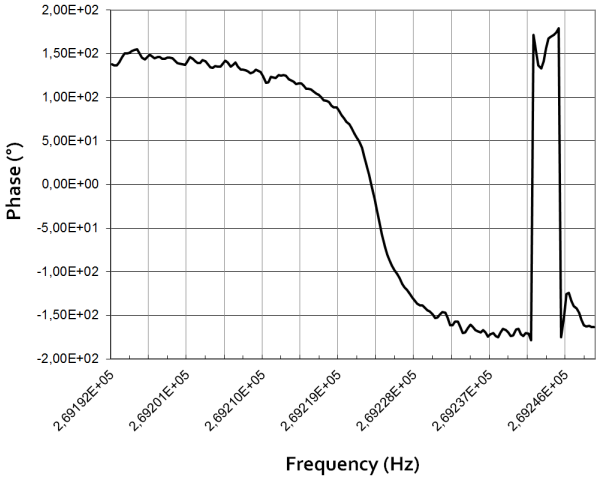

Fig. 2.17 – Phase frequency response of the MNT resonator, 2f measurement, $6V_{DC}$, $40mV_{AC}$ and 200ms integration time. The frequency is the drive frequency, half the motion frequency.

say $4.5nV.\sqrt{Hz}^{-1}$, consistent with the manufacturer's specs ($5nV.\sqrt{Hz}^{-1}$ @ 1kHz). From Robins formula (Robins 1984) (see annex), and assuming a quality factor of 12000, we find the following frequency stability value:

$$\frac{\delta f}{f} \simeq \frac{1}{2Q}\frac{1}{SNR} \simeq 10^{-6} \tag{2.4}$$

Considering the difficulty of such measurements, or said differently, the fact that those devices were poorly designed and little appropriate, this value seemed relatively decent. At this point, there was of course still a lot of work to be done on the resonating device itself, but heartened by the frequency stability obtained, we decided to go on with the assessment of the sensing capabilities of the device, before entering a new design-fabrication-characterization cycle.

2.2.5 Sensor characterization

This work was partly performed by Delphine Pinto, now staff member at LETI, for her 12-months CNAM ("Conservatoire National des Arts et Métiers") thesis (Pinto 2009).

Feedback choice Two straightforward choices were possible: a self-oscillating loop or a Phase-Lock Loop (PLL). The former is the most simple on the principle, suffices to satisfy the Barkhausen

conditions (Colinet *et al.* 2009) both in amplitude and phase. The detection gain of the device has to be high enough to compensate for the energy loss due to damping. In practice, it is also necessary to filter out as abruptly as possible all harmonics away from the resonance so that the oscillator locks onto the right frequency. For the sake of simplicity and genericity, a PLL scheme has been chosen (see its control principle figure 2.18 and its implementation with a sensor figure 2.19). Despite the use of a corrector, it does not bring strong constraints on the resonator's performance and detection gain, and it is easy to implement an external and digital version via LabVIEW for example. This last figure applies to our case, under the condition that the operation point is changed around ω_0 and around a phase difference $\Delta\phi = \frac{\pi}{2}$ so that the beam is kept at resonance. The Voltage Controlled Oscillator (VCO) is either the lock-in internal source or an external AC source controlled by a digital LabVIEW corrector. In our case, H is a simple proportional integrator $H = \frac{P}{s}$ (the phase correction, hence the derivative of the frequency, is proportional to the phase difference in the loop). More complex schemes allowing for noise rejection, speed, accuracy... (Kharrat *et al.* 2008) could be used, which was done later. GPIB connection is used between the computer and the source, which is relatively slow.

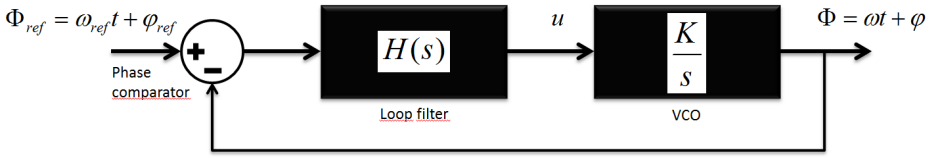

Fig. 2.18 – Principle schematic of a PLL: the phase comparator computes the difference between the global instantaneous reference and output phases ; the loop filter computes the control signal u of the VCO (represented as a proportional-integrator).

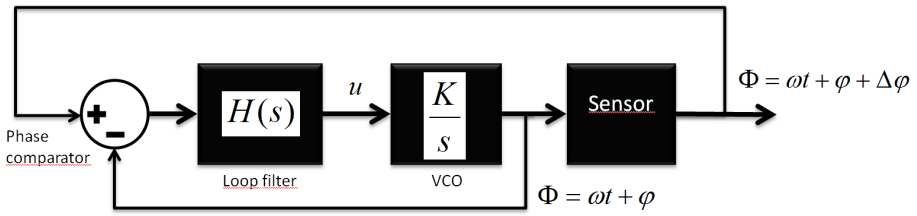

Fig. 2.19 – Principle schematic of a PLL applied to the frequency tracking of a resonant sensor. In this scheme, the feedback is performed only on the phase shift caused by the sensor, as sensor and VCO both operate at the same frequency.

Simulation of an acceleration Some devices included an actuation electrode in close proximity to the seismic mass, so that an electrostatic force could be applied, see an example figure 2.20. This allowed us to simulate the effect of an acceleration, without having to develop a real vibration set-up. Figure 2.21 shows a typical example obtained of the resonance frequency over time, while the mass actuation voltage is varied with 200mV steps, which roughly corresponds to 30mg per step (from linearized expressions of the force applied to the mass), although this experiment clearly went beyond the linear regime. Those measurements proved that our resonant accelerometer was operational, and a few figures could be deduced.

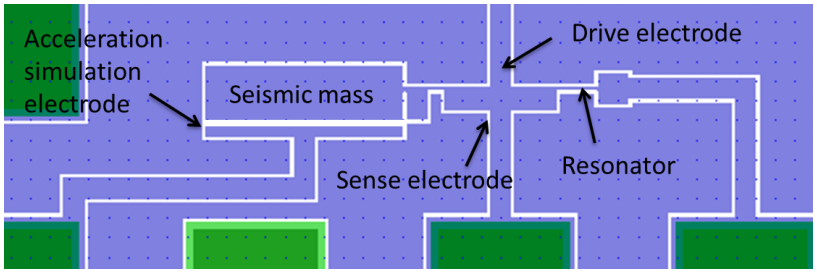

Fig. 2.20 – Layout of an MNT accelerometer (some details are not visible at this scale, see figure 2.2 for the operating principle) with an electrode allowing for acceleration simulation

The PLL response time was on the order of 1s, the measured sensitivity about $40Hz.g^{-1}$, and the crude observation of the frequency fluctuation at short times showed a noise floor around a few 10mHz (with a lock-in integration time of 200ms), that is to say below $1mg.\sqrt{Hz}^{-1}$. This number was one order of magnitude away from the target ($50\mu g.\sqrt{Hz}^{-1}$ resolution) and a 1.5kHz bandwidth. This said, the PLL corrector was extremely basic and did not filter much noise in the loop, the communication between the different apparatus was very slow. Also, the footprint of the mechanical structure itself is around $0.02mm^2$, way below the requirements, even for consumer market. This is most certainly one of the smallest VLSI silicon resonant accelerometer with the highest motional resistance characterized in the literature (Pinto *et al.* 2009).

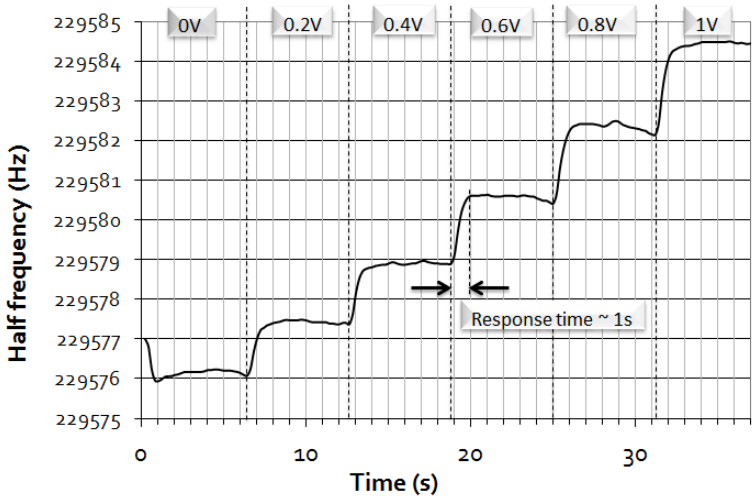

Fig. 2.21 – Typical result of the frequency tracking of a resonator while applying an electrostatic force to the seismic mass. Central frequency 459kHz, Q=35000. 0.2V from position at rest corresponds to an acceleration of 30mg.

There was definitely room for much improvement in a variety of domains: mechanical architecture of the accelerometer, noise modelling of the resonator, transduction principles, characterization methods. This first try gave us enough material and the necessary feedback to fine tune our models and address specific specifications.

2.3 Limit of detection analysis [8]

This study was performed at a time when the inertial market was moving fast and when new categories emerged. As an example, there was a jump in accelerometer use in mobile phones from three percent in 2007 to approximately 33 percent in 2010. While devices with a wide range of performance and cost continue to hit the market, there is a huge difference between high- and low-end systems. At the bottom of the heap are automotive-grade sensors, available as individual sensors or in Inertial Measurement Unit (IMU). Navigation and marine grade represents the top of the line. Determining which type of inertial sensor is right for which application can be a difficult process due to the lack of information available pertaining to the subject. It is true for buyers, for manufacturers, as well as for us. As already mentioned, consumer designs demand small, low-power and multi-axis inertial sensors rather than the high-performance devices required for automotive and medical applications.

In terms of research and development, it was necessary to answer the question as to which group of application may be addressed by the general trend of miniaturization. A proper evaluation of noise sources was needed, at a time when their investigation in the microsystems community was in its infancy (Djuric 2000).

Among the literature experimental achievements, many put forward only the sensor's sensitivity (Aikele *et al.* 2001), whereas the main figure of merit should be the limit of detection (Gabrielson 1993), which extremely few groups measured and even fewer modeled (Seshia *et al.* 2002). Moreover, most of the studies make the assumption that the electronic noise far exceeds the Brownian noise of the structure (Seshia *et al.* 2002). Yet, advances in readout circuits showing better performances (Yazdi *et al.* 2004) combined with the use of smaller and noisier devices demand a global study. Hierold (2004) has shown the effect of the miniaturization on the performances, but again considering that the electronic noise is dominant, and only for the traditional capacitive detection.

In this section, we will compute the LOD for both capacitive and frequential readout, for both thermo-mechanical noise and electronic noise, as well as the sensor grade, that it to say the ratio full range over LOD.

2.3.1 Capacitive sensing

For this sensing, a very similar comb-drive structure as in figure 1.4 is considered and notations are shown figure 2.22.

Readout and noise sources Assuming that the sensor's bandwidth is very low compared to the mass resonance pulsation ω_m, the displacement x of the mass relatively to the fixed combs under an acceleration γ is:

$$x(t) = \frac{\gamma(t)}{\omega_m^2} \tag{2.5}$$

The true capacitance variation can be linearized if $x \ll g_c$. Usually the full range is set by the acceleration γ_{full} over which the sensor output reaches the linearity spec $\mathcal{L}$:

$$\gamma_{full} = g_c \omega_m^2 \sqrt{\frac{\mathcal{L}}{\mathcal{L}+1}} \tag{2.6}$$

[8] Details can be found in Hentz *et al.* (2008*a*)

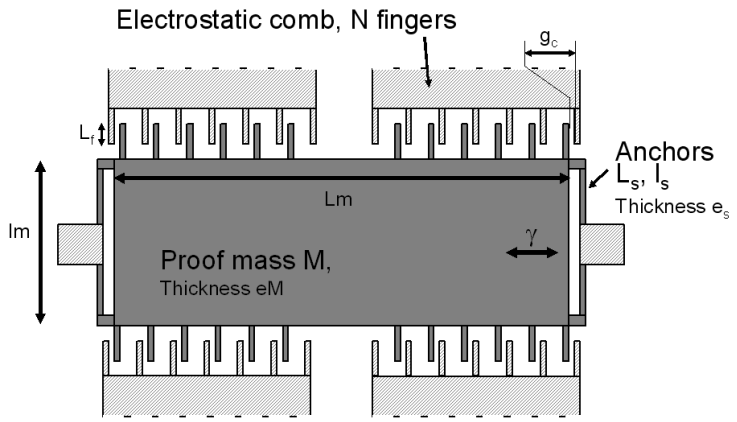

Fig. 2.22 – Studied structure

The LOD will be computed considering both thermomechanical noise and amplifier's noise.

Assuming a mass quality factor Q_m, the force noise power due to thermomechanical fluctuations of the mass is (Djuric 2000)

$$S_f^{th}(\omega) = \frac{2}{\pi} k_B T \frac{M\omega_m}{Q_m} \tag{2.7}$$

As $f = M\gamma$, this force noise power is easily expressed in acceleration $S_\gamma^{th} = \frac{1}{M^2} S_f^{th}$.

Even if not intrinsic to the amplifier and if it depends on the load impedance, the Noise Figure is a convenient quantity we will use here:

$$NF = 10 \log \frac{\text{SNR at input}}{\text{SNR at output}} = 10 \log \frac{\text{output noise power referred to its input}}{\text{noise power at input}} \tag{2.8}$$

The noise power (expressed in force or acceleration) brought by the amplifier is then $S^a(\omega) = \left(10^{\frac{NF}{10}} - 1\right) S^{th}(\omega)$.

Assuming noise sources are uncorrelated and defining the LOD as the rms acceleration noise, the total noise power is the sum of the noise powers and the acceleration variance in the bandwidth BW is computed as

$$LOD = \sigma_\gamma = \sqrt{\int_0^{BW} S_\gamma^{total}(\omega) d\omega} \propto \frac{1}{\sqrt{Q_m}} \sqrt{10^{\frac{NF}{10}} BW} \frac{L_s^{\frac{1}{4}}}{M^{\frac{3}{4}}} \tag{2.9}$$

for a constant flexure beam aspect ratio. The "resolution class" is

$$\frac{LOD}{\gamma_{full}} \propto \frac{1}{\sqrt{Q_m}} \sqrt{10^{\frac{NF}{10}} BW} \frac{1}{g_c} \frac{M^{\frac{1}{4}}}{L_s^{\frac{3}{4}}} \tag{2.10}$$

This very simple model, even if maybe not completely accurate, shows to-be-expected trends: The larger the mass, the lower the LOD. Less expectedly, with a rather weak influence: If the quality factor is assumed to be proportional to the mass (rigorously to its surface), then remains only a power $\frac{1}{4}$. It is equally true for the stiffness of the anchors, which should be low for a good LOD. Of course, the opposite conclusions hold as far as the resolution class is concerned: one would like a very light mass with very stiff anchors. The main conclusion from this first result is that there is very little room left in the design space for orders of magnitude improvement in performance. The new generations of commercial accelerometers most likely took advantage of progress made by manufacturers in the readout electronics (better NF): evergoing progress in the field does not come from efforts on process, transduction or the mechanical structure.

2.3.2 Frequential sensing

To compare performance between capacitive and frequential sensing, we'll model the structure shown figure 2.23. We'll come back later to this choice. It should be seen as a generic structure, comprising a mass M amplifying its inertial force on a resonator by a factor Γ. We'll neglect the rotational rigidity of the anchors compared to the axial rigidity of the resonator.

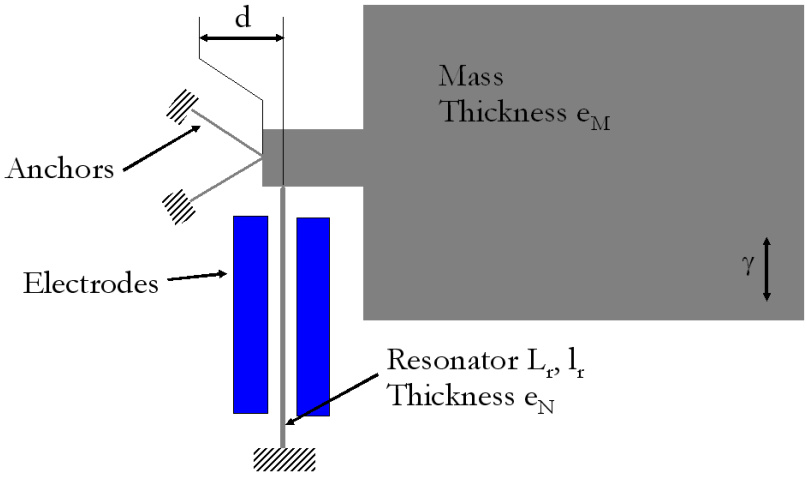

Fig. 2.23 – Studied structure

The resonator frequency can be expressed as $\omega_N = \omega_0\sqrt{1+\Omega N}$. Again, a true sensitivity as well as a linearized sensitivity can be computed, as well as a maximum acceleration γ_{full} for which a linear limit is reached.

The force noise spectral density due to thermomechanical fluctuations of the resonator is

$$S_f^r(\omega) = \frac{2}{\pi} k_B T \frac{m_r \omega_0}{Q} \tag{2.11}$$

It may be assumed without loss of generality that the bandwidth BW used by the PLL readout is very narrow compared with the $-3dB$ bandwidth of the resonator. We will then use its transfer function $\frac{Q}{m_r\omega_0^2}$ at resonance to compute the displacement noise density S_x^r.

The question is now: how much frequency fluctuation does this amplitude noise create? Following Robins (1984), the frequency noise power of a closed-loop system is

$$S_\omega^r(\omega) = \left(\frac{\omega_0}{2Q}\right)^2 \frac{S_x^r(\omega_0)}{P_0} \tag{2.12}$$

where P_0 is the displacement carrier power, ie the RMS drive amplitude of the resonator $\frac{1}{2}a^2$. We will choose to drive it below the bistability limit due to the mechanical non-linearity: $a_c = 1.685\frac{l_r}{\sqrt{Q}}$ (Postma *et al.* 2005, Kacem *et al.* 2009).

Like in the capacitive case, the displacement noise power brought by the amplifier is then $S_x^a(\omega) = \left(10^{\frac{NF}{10}} - 1\right) S_x^r(\omega)$ which may be expressed in frequency noise, thanks to 2.12.Under the assumption of uncorrelated sources, the total noise power is

$$S_\omega^{total}(\omega) = S_\omega^m(\omega) + S_\omega^r(\omega) + S_\omega^a(\omega) \tag{2.13}$$

Neglecting the noise induced by the thermomechanical fluctuations of the mass, we find:

$$LOD \propto \sqrt{10^{\frac{NF}{10}} BW} \frac{\sqrt{L_r e_N}}{M} \tag{2.14}$$

from where we can deduce the resolution class of the accelerometer

$$\frac{LOD}{\gamma_{full}} \propto \sqrt{10^{\frac{NF}{10}} BW} \frac{L_r^{\frac{5}{2}}}{\sqrt{e_N} l_r^3} \tag{2.15}$$

A few comments can be made here: unlike an accepted idea, the LOD does not depend on the resonator quality factor. This is true under two conditions: i) the error made by the frequency-tracking technique (eg PLL) is negligible and ii) the resonator is driven at a quality factor-dependent amplitude, like the onset of non-linearity. Secondly, the resolution does not depend on the vibrating width of the resonator: indeed, the smaller the cross-section area, the more sensitive the resonator (sensitivity $\propto \frac{1}{l_r^2}$), but also the noisier ($S_\omega^r \propto \frac{1}{l_r^2}$). Finally, the accelerometer class scales like $\frac{1}{l_r^3}$: the ratio full scale/resolution depends only on the resonator itself whereas large mass and amplification linearly improve the resolution, a very intuitive result.

Figures 2.24 and 2.25 show the ratios of frequential over capacitive LOD and resolution class. It is clear that below a minimum feature size of a few 100's nm, the resonant detection displays a better resolution than the capacitive one for given in-plane mass dimensions. The opposite conclusion can be drawn about the resolution class, orders of magnitude better for the capacitive readout. It does scale with dimensions only for the realistic case where suspensions scale like the resonator. If we focus on the consumer applications, we aim at a few g full range, with around $500\mu g$ resolution (100Hz bandwidth) ie a resolution class better than 10^{-3}. In terms of process and according to figure 2.24, this means resonators at the frontier between DUV and e-beam lithographies. At these typical dimensions, capacitive and frequential detections may have about the same resolution, but only the frequential detection leaves room for size reduction.

Further comments The above study has been conducted in the frequency domain, and has assumed white noise sources, which is the only way to be predictive in the design process. Since then, another work (Le Foulgoc 2008) has carried out the same kind of analysis, but with more empirical (but more thorough) a noise description : the Leeson equation, describing the noise spectral densities in power functions of frequency. This formalism better describes the typical shape of the Allan deviation experimentally observed. This group worked as well on how size may be reduced while retaining good performance, even for navigation purposes.

Looking back at equations 2.14 and 2.15, a clear conclusion may be drawn: the decrease of the resonator footprint induces a drastic seismic mass reduction, at least its in-plane dimensions, which degrades the LOD. To compensate for this loss, it is necessary to drastically reduce the length and thickness of the resonator. This is detrimental to the resolution class, unless the resonator aspect ratio is decreased (increase in l_r), largely increasing its resonance frequency.

In brief, the design and technology roadmap we drew from this is:

- a seismic mass with reduced in-plane dimensions, but a large thickness.
- a NEMS resonator, with **a much smaller thickness**, resonating at a higher frequency.

This is what pushed towards the development of a 2-thickness process called *M&NEMS*.

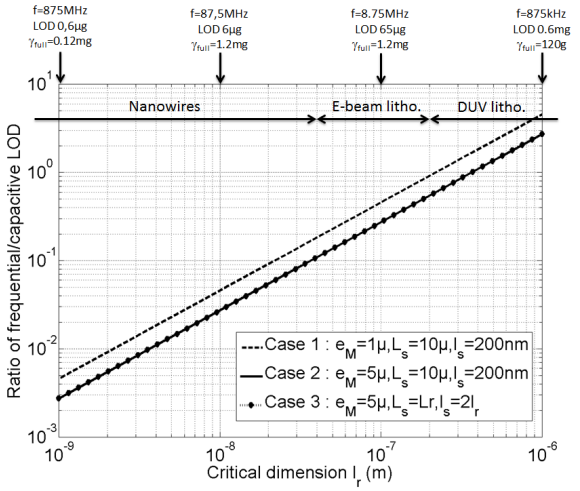

Fig. 2.24 – Frequential/capacitive LOD ratios vs l_r, for this particular set of parameters: $L_M = 150\mu$, $l_M = 120\mu$, $\Gamma = 37.5$, $L_r = 100l_r$, $e_N = 2l_r$, $g_c = l_s$, $Q_m = 10000$, $BW = 100Hz$

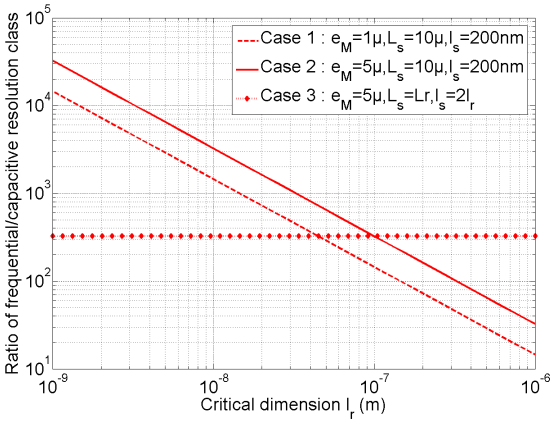

Fig. 2.25 – Frequential/capacitive class ratios vs l_r, for this particular set of parameters: $L_M = 150\mu$, $l_M = 120\mu$, $\Gamma = 37.5$, $L_r = 100l_r$, $e_N = 2l_r$, $g_c = l_s$, $Q_m = 10000$, $BW = 100Hz$

2.4 *M&NEMS* accelerometers [11]

This work was mainly funded by the ANR project M&NEMS led by Valérie NGuyen, from 2006 to 2009. A number of people were involved in the clean-room fabrication: Samuel Harrison, Fanny Delaguillaumie, Mouna Klein, Mylène Savoye.

2.4.1 Process

As this was the first attempt for a 2-thickness process, not aggressive thicknesses and feature sizes were chosen, using only DUV lithography. The process is described figure 2.26: a SOI is used, its silicon top layer thickness is which of the NEMS. Then lithography and etching of the NEMS and of the bulk contact are performed (a). Follows a $0.3\mu m$ thick oxide deposition followed by lithography/etching of the NEMS protection (b). In the same step, an over etching of the oxide is performed to open the silicon bulk contact. A few microns thick silicon epitaxial growth (or a polysilicon deposition) is done to realize the MEMS part (c). Depending on the silicon doping level of the MEMS part, an implantation step can be added for the electrical contact pads. Contacts are defined by a $0.5\mu m$ metal deposition followed by lithography/etching of pads (e). A last lithography step and a Deep-RIE of silicon thick layer is performed to realize the MEMS structure, to isolate the bulk contact, and to open the SiO2 protective layer of the NEMS (f). The release of the sensor is finally achieved by HF-vapor etching (g).

2.4.2 Mechanical structure

According to results obtained in the former section 2.2, scaling is not favorable to inertial sensing, unless the resonator alone scales down. For the first M&NEMS designs, we chose a few μm thick inertial mass and a few hundred nm thick resonators. As described figure 2.24, the resonator feature sizes were chosen at the limit DUV/e-beam lithography, ie around 250nm. It was engineered to be

[11] Details can be found in Robert *et al.* (2009), Juillard *et al.* (2010), Kacem *et al.* (2012*c*)

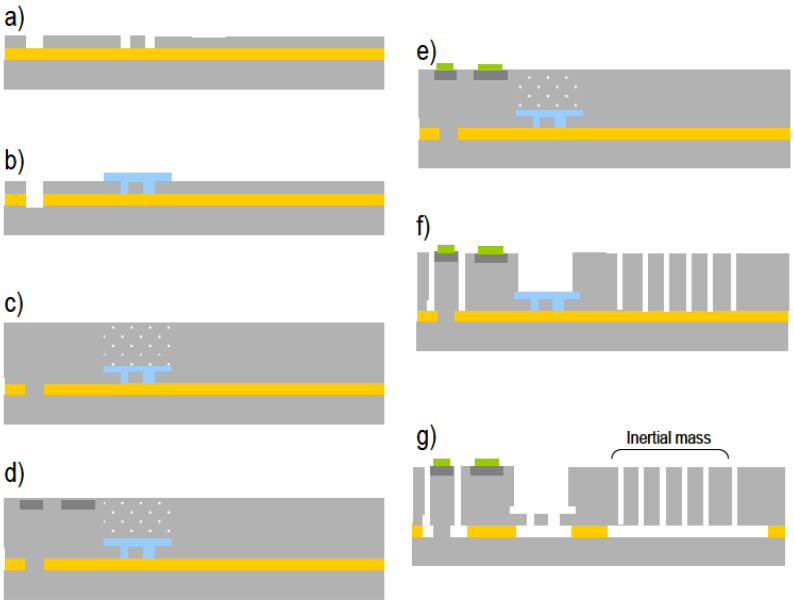

Fig. 2.26 – Process flow for the M&NEMS accelerometer

close to consumer market requirements: full range $+/-30g$, noise floor $350\mu g.\sqrt{Hz}^{-1}$, footprint $0.2 * 0.15mm^2$ (for one axis). The mass dimensions vary from 100 to $200\mu m$ (similar to the MNT resonator), the resonator length is of the order of $20-30\mu m$, its width around 250nm, which gives frequencies around a few MHz.

The overall principle is shown figure 2.23, it is inspired from Aikele *et al.* (2001). Figure 2.27 shows a SEM photo of one device. The "NEMS" zone (of reduced thickness) is clearly visible, as well as the junction of the NEMS resonator to the MEMS mass.

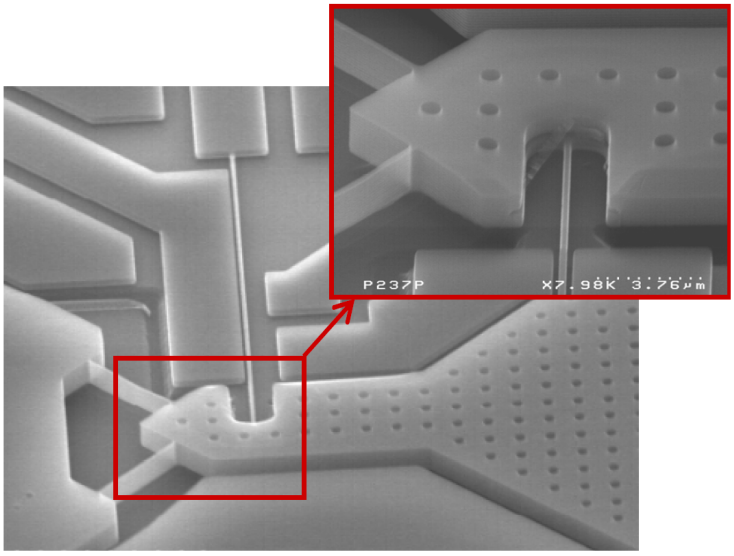

Fig. 2.27 – SEM photo of an M&NEMS accelerometer

The mass is suspended via two orthogonal beams : the mass can almost only "rotate" around their intersection point, as close as wanted to the resonator. Moreover, the notch in the mass at the resonator junction allows for a purely longitudinal force on the resonator. Also, the mass is longer

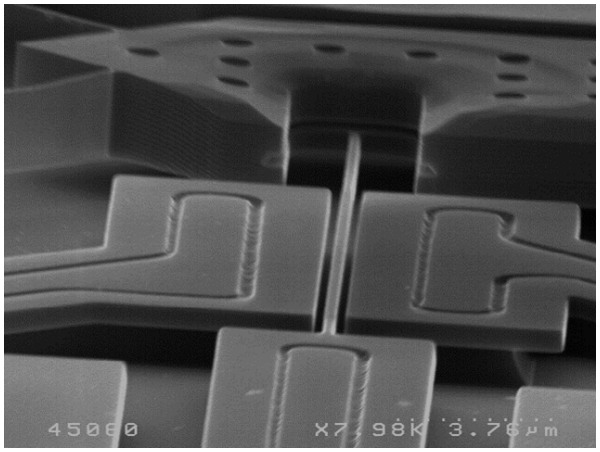

Fig. 2.28 – SEM zoom on the NEMS resonator link with the MEMS area

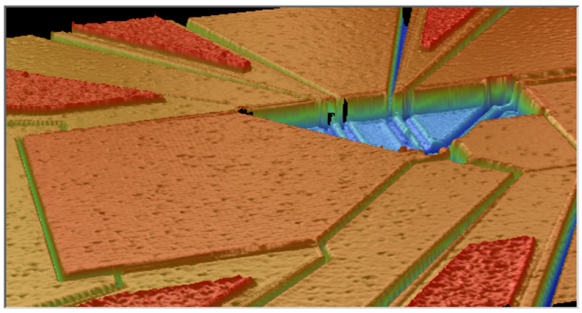

Fig. 2.29 – Wyko interferometer picture of an M&NEMS accelerometer: the NEMS "pool" is clearly visible

in the transverse direction than in the sensitive direction, to increase the amplification factor. FE simulations have shown that these refinements make this design extremely sensitive.

Capacitive transduction was also chosen for this device generation. We knew (see section 2.2.4) that the electrical measurements with good SNR of such small and high frequency resonators would be very tedious: capacitance variations were expected around a few aF and the motional resistance around a few $G\Omega$. Therefore we partnered with the team of Jérôme Juillard at Supelec to design a specific ASIC, bonded as close as possible to the device so that output capacitances were reduced to a minimal value (Juillard *et al.* 2010), as well as with Lionel Buchaillot team at IEMN for characterization. Before the ASIC could be designed and fabricated, the resonators had to be measured by external means. Of course, because of such a motional resistance, any attempt for direct or homodyne detection failed to give results.

2.4.3 Capacitive downmixing

Heterodyne schemes are very well known in the RF community for down conversions of RF signals, for mixing and filtering, for example in FM receiver units (Hagen 1996). They were also used in the same context when mixing and filtering subunits were performed by micromechanical capacitive resonators (Wong *et al.* 1998). Later, they were used for large motional impedance capacitive silicon resonators for clock generation (Bhave 2004). In these two last cases, characterization was simply performed with a spectrum analyzer for quick characterization. Consequently, fine amplitude measurement and simple electrical models could not be performed. Other heterodyne schemes or frequency modulation techniques have been used more recently for low signal characterization purposes with impressive performance (Durand 2009, Gouttenoire *et al.* 2010, Walter 2011).

The main advantages of downmixing conversion is that input and output signals may be at orders-of-magnitude different frequencies, preventing electrical input from feeding forward to the output and from masking the resonant peak; secondly as the output frequency can be chosen as small as wanted, signal loss through the load capacitance can be greatly diminished. Low-noise amplitude versions were performed (for example with lock-in amplifiers and the making of an external reference signal): Knobel & Cleland (2002) have shown the detection of the piezoelectrically

induced charge in a mechanical resonator with a SET; Bargatin *et al.* (2005) applied downmixing for ultra sensitive piezoresistive NEMS readout, Sazonova *et al.* (2004) for conductance variation of Carbon Nano Tubes (CNT), Chen *et al.* (2009) for monolayer graphene devices, Defoort *et al.* (2011) with magnetomotive actuation/detection and very recently Bartsch *et al.* (2012) with integrated FinFET NEMS.

Marc Sworowski while in post-doc in the team in 2008/2009 was among the first to try downmixing with ultra large motional resistance M/NEMS (Kacem *et al.* 2012*c*). Figure 2.30 shows the overall principle.

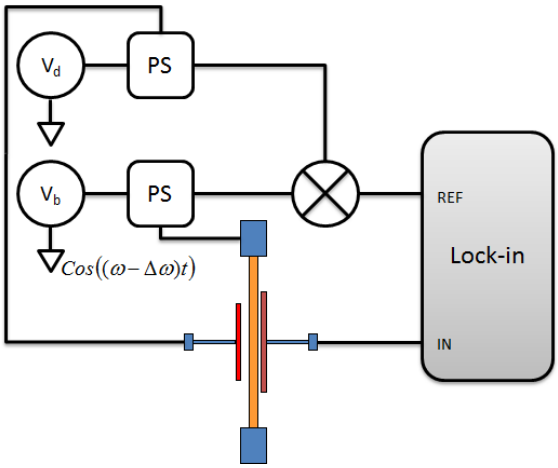

Fig. 2.30 – Capacitive downmixing principle

In this scheme and after low-pass filtering, the output signal is proportional to $V_b \frac{\partial C}{\partial t} \propto V_b \sin \Delta\omega t$.

Again, several configurations for drive can be used: "1f" with the addition of the DC voltage (see figure 2.31), "2f" where the drive voltage is a $\frac{\omega}{2}$ harmonic (see figure 2.32). The background happened to be much lower in the latter, although in any case it should theoretically be zero or negligible. Also, the background logically decreased with an decreasing drive, but as well with an increasing voltage. Another configuration was then tried: the "$\frac{f}{2}$" configuration (see figure 2.33). This technique was the only one that allowed the electrical characterization of the smallest of our devices ($15\mu m$ long, $400nm$ wide, $250nm$ sensing gap, frequency around 13MHz) with a reasonable SNR, see figure 2.34. Both SNR and SBR are around 40dB@100ms (equivalent to an Allan deviation of 5.10^{-6}) for this measurement. This is very likely one of the smallest capacitive resonator electrically measured in the literature without cointegration. Such electric performances translate into a resolution around a few $mg.\sqrt{Hz}^{-1}$, that is to say on the same order as which of the $4\mu m$ SOI accelerometers, way above the expected theoretical noise floor.

Meanwhile, discussions with various companies orientated the group's efforts towards a piezoresistive, non-resonant, sensing (at least as far as the accelerometer is concerned) for simplicity reasons. Unfortunately then, the characterization of the resonator and the assessment of the sensor performance could not go further, although the group actively went on with the M&NEMS concept.

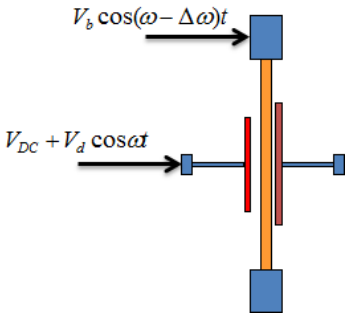

Fig. 2.31 – "1f" configuration

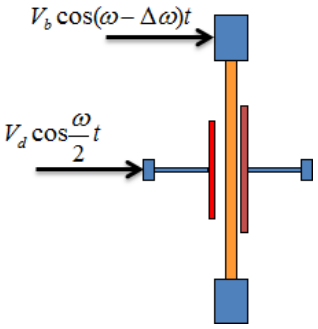

Fig. 2.32 – "2f" configuration

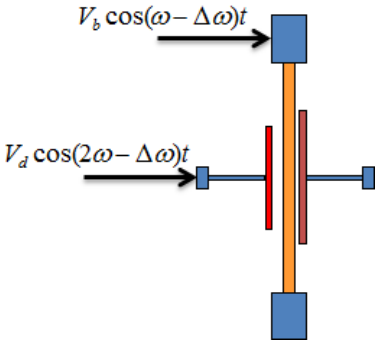

Fig. 2.33 – "$\frac{f}{2}$" configuration

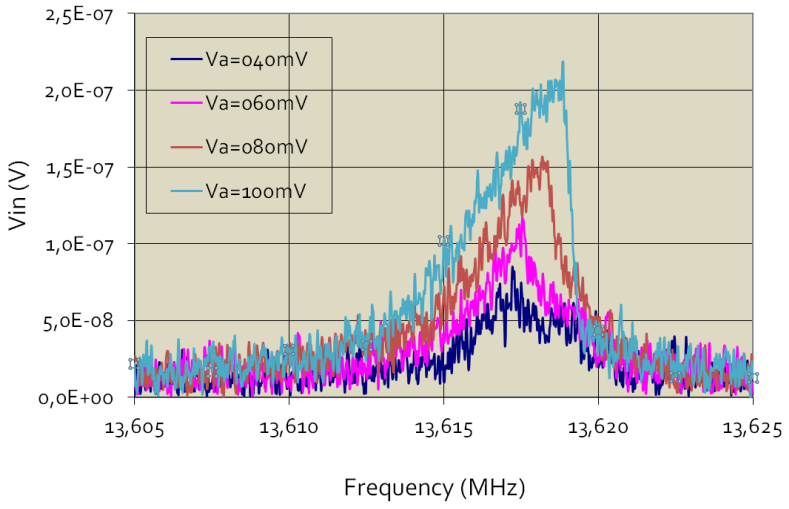

Fig. 2.34 – Frequency responses of the smallest capacitive resonator with the $\frac{f}{2}$ configuration.

	1f	2f	$\frac{f}{2}$
Drive harmonic (at ω)	$\propto V_d.V_{dc}$	$\propto V_d^2$	$\propto V_dV_b$
Output signal (at $\Delta\omega$)	$\propto V_d.V_b.V_{dc}$	$\propto V_d^2.V_b$	$\propto V_d.V_b^2$

Table 2.2: Harmonics in the different downmixing configurations

2.5 Conclusion

Several years of technological, characterization and model development, as well as many students involved paved the way for subsequent, more applied, developments. From an applicative point of view, addressing the industrial need for cheaper inertial sensors without performance loss proved to be a long and strenuous path. But it was for us a very good excuse to tackle a range of technical and scientific challenges. Many characterization techniques have been investigated ; in order to improve the resolution of our devices, we investigated the sources of damping and noise perturbing the frequency stability or our resonators. Homogeneously downscaling devices could not solve the issue: it significantly degrades the overall performances, mainly because the sensitive mass and hence the sensitivity scale down at the power three. The M&NEMS concept originated from the theoretically-proven idea that a resonant NEMS would be extremely sensitive to forces applied by a (small) MEMS inertial mass. This was the way to go. And this opened the way to one of the main activities of the group: transduction for NEMS appeared to be the main challenge, and the electrostatic one was most likely not the easiest solution, despite many technological and electrical improvements. The next chapter will describe our work about transduction for NEMS which took place partly simultaneously. Resonant devices with piezoresistive gauges were fabricated at the end of the M&NEMS project (see figure 2.35) and there is no doubt they would have been very efficient, surpassing the requirements, had we have the resources to go on with their characterization.

Today, the M&NEMS concept is very close to industrial transfer, and is a flagship of sensing at LETI, with non-resonant accelerometers. The number of patents, around 16, is well representative of the maturity reached by this activity (Robert *et al.* 2009, Robert & Hentz 2009).

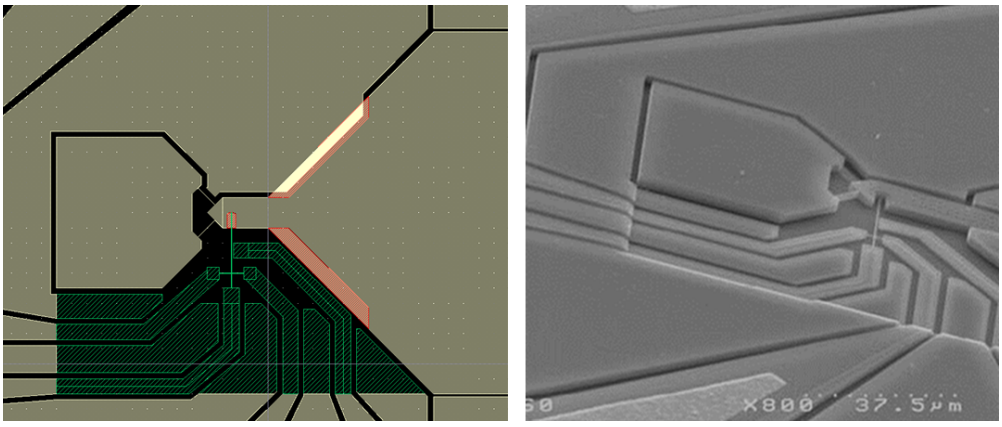

Fig. 2.35 – M&NEMS accelerometer with piezoresistively sensed resonator: two tiny gauges close to the resonator anchors are suspended

Chapter 3

VLSI NEMS: transduction and applications

3.1 Introduction: NEMS for sensing and time keeping? [1]

As explained in the previous chapter, the frequency stability is essential to the good resolution of a resonant sensor, but it is also essential to a good time-keeping device (clock). The question was then: are NEMS good candidates for time-keeping purposes? In many applications nowadays, in particular consumer (mobile phones, laptops, mp3 players...), this function is fulfilled by quartz crystal bulk resonators. Those are ubiquitous these days, but remain expensive, compared to the main chip : for example, in a mobile phone, the chip costs a few dollars including the quartz device alone which costs 50 cents. The main reason for this holds in the fact that quartz is not easily integrable and cannot be processed with microelectronics tools. Therefore there has been active research in the last years to replace quartz by silicon. Equation 2.12 shows that the frequency fluctuation is inversely proportional to the SNR, hence to the carrier power P_c. The latter is of course proportional to the strain energy stored in the mechanical resonator itself. Kaajakari *et al.* (2004) have shown that the strain energy density at the onset of non-linearity for bulk mode silicon resonators was three orders of magnitude higher than which for shear-mode quartz, opening the door to smaller and integrable silicon devices. As opposed to plates resonating in bulk modes, flexural microbeams lack the strain capacity and quality factor to rival quartz crystal resonators, mainly due to their weak stiffness. This is why silicon devices in the literature closest to communication requirements (in terms of phase noise, long-term stability and temperature drift) are bulk-mode plate devices (Rantakari *et al.* 2005, Koskenvuori *et al.* 2004, Lin *et al.* 2004, Sundaresan *et al.* 2006, Dalal *et al.* 2011, Hung & Nguyen 2011, Zuo *et al.* 2011), reaching motional impedances very close to 50Ω. At LETI, we too followed this trend with success (Colinet *et al.* 2010).

Simultaneously, driven by LETI's technological means as pointed out in chapter 1, the group was willing to go down the path of CMOS co-integration to reduce output capacitances to an extreme minimum. In the idea of monolithic integration (In-IC processing), this meant extremely low minimum feature sizes and thickness. The question was: can co-integration compensate for the low strain capacity of NEMS and allow their use for time-keeping? Following the seminal work of Ionescu group at EPFL (Abelé *et al.* 2005), Cédric Durand, PhD student from IEMN, Lille - EPFL

[1] Details can be found in Colinet *et al.* (2010), Duraffourg *et al.* (2008), Ollier *et al.* (2012)

aimed at an aggressive device: the Resonant Gate (RG)-MOSFET where first stage amplification and resonant part are one single unit (the gate dielectric is an air gap whom variation modulates the inverted charges along the channel, and hence the drain current). Two technological paths were investigated : a 400nm SON (silicon on nothing) technology (commonly developed by ST-LETI-EPFL-IEMN) as well as a 160nm SOI technology developed by LETI (Durand 2009, Durand *et al.* 2008, Duraffourg *et al.* 2008).

Despite huge progress in terms of process, device and characterization, those first attempts provided us only with preliminary and incomplete answers: there definitely was signal improvement relative to capacitive sensing, but doubt remained as to the gain brought by such a heavy technology. Investigation in both field effect transduction (Bartsch *et al.* 2012) and NEMS co-integration (Ollier *et al.* 2012) kept being pursued in their own way (both within the FP7 STREP project "NEMSIC"), but it appeared more and more clearly that time keeping would not be the mainstream application for NEMS. On the other hand, a transduction type adapted to VLSI NEMS remained to be found where they would very likely be a key player: gravimetric detection.

3.2 Piezoresistive NEMS for gravimetric sensing [2]

3.2.1 The Alliance for nanosystems VLSI applications

As stated on its leaflets, LETI and Caltech (namely Professor Roukes group) have joined their expertise to transition from the era of "nanocraft" to very-large-scale integration of nanosystems, with the prospect of producing a tool-driven revolution for system biology. In Professor Roukes' vision, NEMS are key elements for a change in paradigm for a number of biological or chemical analysis tools. As a part of this Alliance creation process led by Philippe Andreucci, I contributed in choosing a few key applications: firstly NEMS for multi-gas sensing, and secondly, NEMS for mass spectrometry. In both cases, the principle is the same, the device frequency is shifted because of a mass accreted onto its surface, but in two very different regimes : in the gas case, the concentration (even extremely low) is such that the distribution of mass on the NEMS is homogeneous over its surface, whereas in the spectrometry case, the "landing" of single particles on the NEMS is an individual event.

Mass sensing Let us consider the landing of a point mass δm onto the surface of a NEMS. Differentiating the formula for resonant frequency, we have:

$$\frac{\delta f}{f} = -\frac{1}{2}\frac{\delta m}{m} \tag{3.1}$$

If dimensions scale like α, then the mass relative sensitivity of a resonator scales like α^{-3}. This fact alone was often stated to make the case of efforts in the NEMS field.

Of course, this does not convey the whole truth, and the scaling of the mass resolution or LOD is needed: Assuming the thermomechanical noise is the dominant source of noise (meaning that transduction is good enough to read this noise, which is likely in vacuum), a drive power at the onset of NL (see next chapter), and combining equations 2.12 and 3.1, the mass resolution δm scales

[2] Details can be found in Mile *et al.* (2010), Fanget *et al.* (2011), Arcamone *et al.* (2011), Bargatin *et al.* (2012)

like (see annex for more details)

$$\delta m \propto \left(\frac{\rho^5}{E^3}\right)^{\frac{1}{4}} \alpha^2 \tag{3.2}$$

where E is the Young's modulus and ρ the mass density; this expression shows all the potential of NEMS for mass sensing. One will notice that the quality factor does not appear in the equation above, just like for inertial sensing. This is because the onset of NL depends on the square root of Q, just like the thermomechanical noise.

Gas sensing Chemisorbtion demands an additional transduction: the functionnalization layer. A chemical measurement is interested in the relative concentration of a gas analyte in a carrier gas. The mass of analyte at the concentration c in the gas phase above the solid phase, adsorbed in this layer is

$$\delta m = \rho_{analyte} V_f K \delta c \tag{3.3}$$

where $\rho_{analyte}$ is the mass density of the adsorbed gas, V_f is the volume of the functionnalization layer and K is the so-called partition coefficient, characterizing the couple analyte/functionnalization. It is the ratio of the concentration in the gas phase over the concentration in the solid phase, at equilibrium (it is function of temperature). The concentration sensitivity is:

$$\frac{\delta f}{f}\frac{1}{\delta c} = \frac{1}{2m}\rho V_f K \tag{3.4}$$

We can safely consider that the functionnalization layer volume is proportional to the device surface S (one could argue to its thickness too), then the sensitivity scales like α^{-1}. Under this assumption, one can compute the concentration resolution, or use another convenient figure of merit, the surface mass resolution $\frac{\delta m}{S}$, independent from the functionalization type.

Under the same assumptions that the thermomechanical noise dominates and that V_f is proportional to the device surface, the concentration resolution does not scale:

$$\delta c \propto \frac{\delta m}{S} \propto \left(\frac{\rho^5}{E^3}\right)^{\frac{1}{4}} \alpha^0 \tag{3.5}$$

Again, this result contradicts a common belief in the community. Of course, the sensitivity is still much higher for small devices, and this is true if the transduction allows for the reading of the thermomechanical noise floor (which, at ambient pressure, is not necessarily the case). We'll come back to this later in the chapter.

3.2.2 Metallic piezoresistive devices

Prof. Roukes group was advocating for the use of metallic piezoresistors in NEMS (Li *et al.* 2007) for simple reasons: as their resistance is much lower than semiconductor resistors, the associated Johnson noise is lower, and the noise-matching is way easier. This could compensate for a low bias voltage and an orders-of-magnitude lower gauge factor and eventually yield a very good SNR. The gauge factor can be expressed as

$$\gamma = (1+\nu) + \frac{1}{\varepsilon}\frac{\Delta\rho}{\rho} \tag{3.6}$$

where ν is the Poisson's coefficient, and ρ is the electrical resistivity. The first term in this expression is a change of resistivity due only to geometrical changes in the lattice. It is typically only

of order 1 or 2. The usual piezoresistive effect is the second term of this expression which in metals is of order unity too. The global gauge factor is around 2, to be compared with semiconductors gauge factors which can vary wildly (with doping for example), but which can be as high as 100 in silicon.

Figure 3.1 shows one of the fabricated metallized devices, proposed by Caltech (Bargatin 2008, Bargatin *et al.* 2007). Fabrication was followed by Carine Marcoux, staff member at LETI. It consists of a silicon beam with two AlSi loops at its extremities, one for thermoelastic actuation (an AC current flows through it, heats the metal loop, and the expansion difference with the silicon is the bimorph-effect-based actuation) and one for detection (the beam displacement stresses the metal loop which changes its resistance). The choice of metal has been a long and difficult process: it had to be CMOS compatible, light, with low-resistivity, free of any hysteresis effect (problem reported for aluminum in the literature, but which we did not encounter), not magnetostrictive (like Ni) for example. Gold, previously used by Caltech, was of course ruled out because of its incompatibility with CMOS clean-rooms. The use of AlSi in our process for metallic piezoresistive sensing is patented (Andreucci *et al.* 2009).

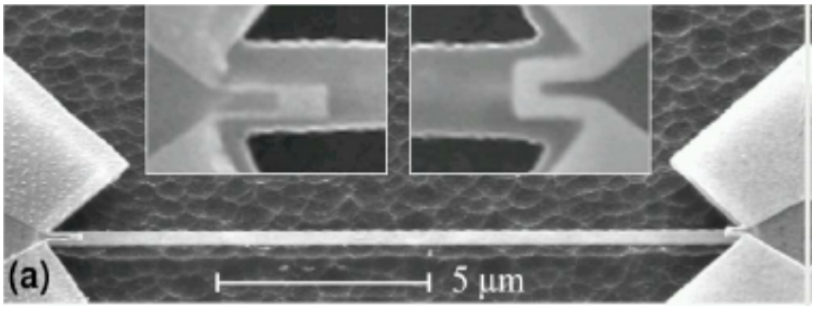

Fig. 3.1 – Caltech metallic piezoresistive devices. Two tiny metal loops are placed on the SiC beam close to the anchors, one for thermoelastic actuation, the other one for piezoresistive strain sensing ; from Bargatin *et al.* (2007)

Several kinds of devices were fabricated as will be seen in the following. Modelling in order to understand their physical behavior was very helpful in the prospect of a final choice.

Optimal power determination This determination involves consideration of two competing effects on the device performance. First, using larger bias and drive powers will obviously increase the signal out of the device. However, as these powers are increased, the device temperature increases. For surface capture techniques such as polymer and molecular monolayer coatings, higher temperatures result in a reduction of the mass adsorbed by the coating in thermodynamic equilibrium; this reduces the sensor response to a given analyte concentration. From the competition between these two effects, an optimal sensor temperature, and thus operating power, can be determined.

The output voltage V_{out} is directly proportional to the bias voltage and thus to the square root of the bias power. Since the thermoelastic drive depends on the heating provided by the drive, V_{out} is also proportional to the drive power:

$$V_{out} \propto \sqrt{P_{bias}} P_{drive} \propto P_{total}^{\frac{3}{2}} \propto \delta T^{\frac{3}{2}} \tag{3.7}$$

where P_{total} is the total power at the device, and δT is the temperature change relative to ambient temperature.

The partition coefficient depends on the temperature, at equilibrium the mass concentration decreases exponentially: $K \propto \exp^{\Delta G/RT}$, where ΔG is the Gibbs sorption energy (negative). Then

$$V_{out} \propto \delta T^{\frac{3}{2}} \exp^{\Delta G/RT} \tag{3.8}$$

Expressing $T = T_0 + \delta T$, performing a first order expansion and solving for δT to find the extremum of V_{out}, we find:

$$\delta T_{optimum} = -\frac{3}{5}\frac{RT_0}{\Delta G} \tag{3.9}$$

Typical sorption energies are around -40kJ/mol, yielding typical device operation temperatures around a few K to a few 10K.

Temperature distribution The dissipated power P in the metal loops being proportional to the square of the voltage, it consists of a DC part and an AC part. For both, the 1D heat transfer equation was analytically solved and validated by a FE model. They are both described figures 3.2 and 3.3. x_{imp} in the analytical model is where the prescribed temperature is zero (computed by FE analysis) and the prescribed heat power is dissipated from -z to 0.

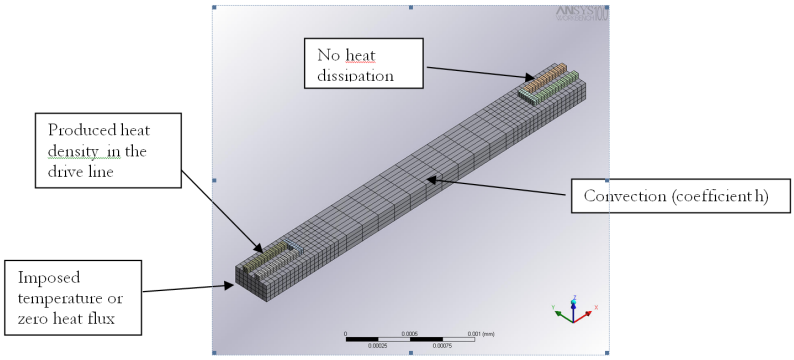

Fig. 3.2 – Prescribed boundary conditions for the FE beam thermal study without substrate

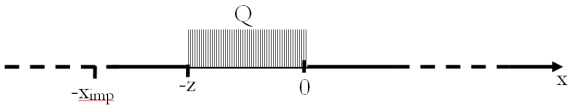

Fig. 3.3 – Prescribed boundary conditions for the analytical model

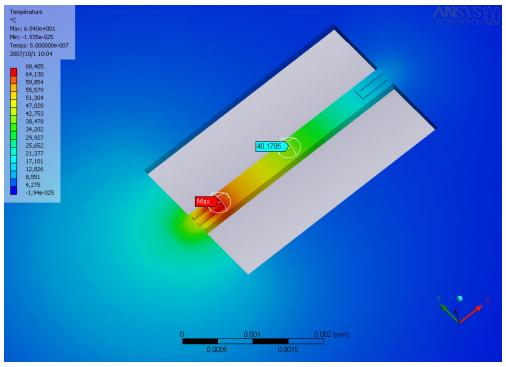

Fig. 3.4 – FE temperature distribution along the beam with substrate ; prescribed temperature is zero far from the beam

The heat equation is

$$\rho c S \frac{\partial T(x,t)}{\partial t} + hT(x,t) - kS\frac{\partial^2 T(x,t)}{\partial x^2} = Q(x,t) \tag{3.10}$$

where h is the linear convection coefficient ($W.m^{-1}.K^{-1}$). The DC temperature distribution amplitude is of the form

$$T_{DC}(x) = \frac{Q_{DC}(x)}{h} + A_1 \exp^{\sqrt{\frac{h}{kS}}x} + A_2 \exp^{-\sqrt{\frac{h}{kS}}x} \tag{3.11}$$

The AC temperature is written as $T(x,t) = T_{AC}(x)\exp^{i\omega t}$ and

$$T_{AC}(x) = \frac{Q_{AC}(x)}{h + i\omega\rho cS} + B_1 \exp^{\sqrt{\frac{h+i\omega\rho cS}{kS}}x} + B_2 \exp^{-\sqrt{\frac{h+i\omega\rho cS}{kS}}x} \tag{3.12}$$

A typical distribution is shown figure 3.5 for 1mW total power. For this power and typical dimensions, the temperature at the center of the beam oscillates around 40K with an amplitude of a few K. Knowing the temperature at the center of the beam and as it is linear with power, one can deduce the total power at the device so that it operates at the optimal temperature.

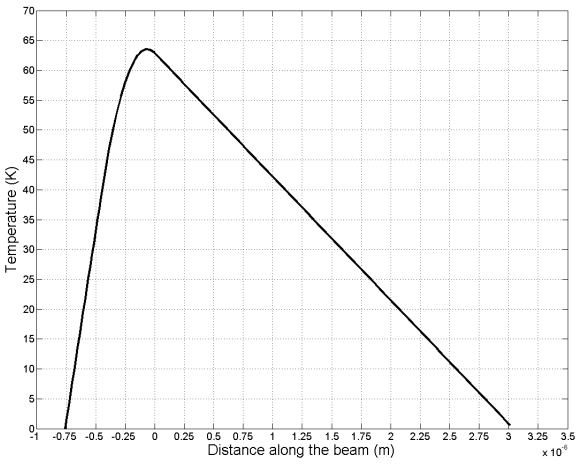

Fig. 3.5 – Temperature along the beam for 1mW total power

Mechanical motion amplitude Let's write the neutral fiber displacement field $\underline{u}(M,t) = w(x)\exp^{i\omega t}\underline{y}$ with the usual mode shape $w(x) = A\cos\lambda x + B\sin\lambda x + C\cosh\lambda x + D\sin\lambda x$. B, C and D can be deduced from the boundary conditions. Only A remains to be found.

The virtual power principle is applied to the device

$$\frac{dE_c}{dt} = P_{ext} + P_{int} \Leftrightarrow \frac{1}{2}\frac{d}{dt}\int_\Omega \rho\underline{\dot{u}}^2 d\Omega = -\int_\Omega c\underline{\dot{u}}^2 d\Omega - \int_\Omega \underline{\underline{\sigma}} : \underline{\underline{D}} d\Omega \tag{3.13}$$

where D is the strain rate tensor and Ω is the beam+metal loops. The thermoelastic constitutive law in our 1D case is $\underline{\underline{\sigma}} : \underline{\underline{D}} = \sigma_{11}\dot{\epsilon}_{11} = E(\epsilon_{11} - \alpha\Delta T)\dot{\epsilon}_{11}$ with $\epsilon_{11} = yw(x,t)$, y being the distance to the neutral fiber.

Replacing in equation 3.13, assuming the temperature is zero everywhere except in the drive loop (which is a strong assumption) where it is also assumed to be homogeneous (way below the thermal roll off), we find at resonance

$$\begin{aligned} \rho S\omega_0^3 \int_0^L w^2(x)dx + E\omega_0 \int_\Omega y^2 \left(w''(x)\right)^2 dxdydz = \\ -\frac{\rho\omega_0^3}{Q} S \int_0^L w^2(x)dx - E_{Al}\alpha_{Al}\Delta T_{Al}\omega_0 S_{Al}\frac{th_{Si}}{2}\int_{-z}^0 w''(x)dx \end{aligned} \tag{3.14}$$

In steady state, the thermoelastic drive energy must be equal to the dissipated energy, so both sides of the equal sign are zero. Performing the algebra allows solving for A and computing the motion amplitude. With typical devices and voltages, we find a few nm.

Output signal The average longitudinal strain in the readout loop must be computed, assuming it is constant in the metal thickness, and equal to the strain at the surface of the silicon beam:

$$\epsilon_{11} = \frac{1}{z}\int_{-z}^{0} \frac{th_{Si}}{2}\frac{\partial^2 w}{\partial x^2}(x)dx \tag{3.15}$$

then $\frac{\Delta R}{R} = \gamma\epsilon_{11}$, γ being the gauge factor of AlSi, taken here equal to 2. And we have $V_{out} = V_{bias}\frac{\Delta R}{R}$. The output voltage sensitivity is typically around a few $10\mu V.nm^{-1}$.

Roll-off frequency There is of course a limit in frequency beyond which the thermoelastic actuation becomes inefficient. There are two reasons for this: the first one is the time constant needed for thermalization of the metal actuator. The thermal diffusion length in a rod is $\lambda = \sqrt{\frac{k}{\rho c\omega}}$. Considering the actuator to be a rod of length $2z$, then equating $\lambda = 2z$ gives the pulsation ω_c above which thermalization will be delayed relative to the voltage. Secondly, $w''(x)$ should not change sign to optimize the actuation term, the last term in equation 3.14, that is the metal loop should not be longer than the first point of inflexion of the highest mode one wished to actuate. Overall, the metal loop should be made as short as possible.

Resolution performance Following the same procedure as in section 2.3, it is possible to compute the concentration resolution of such a device from the thermomechanical and electronics noise in the system. Orders of magnitude improvement can be obtained by using the model and finding an optimal design. Minimum detectable mass with typical dimensions was around a few ag.

Characterization Unfortunately, we encountered many issues with the AlSi patterning and device fabrication. No satisfying device with the geometry described above was fabricated. Nevertheless, other geometries with less aggressive metal feature sizes were characterized, see figures 3.6 to 3.9, all on 160nm SOI wafers, with 50nm thick AlSi on top. A large experimental campaign was performed with those devices, involving several people at LETI (in particular Denis Mercier, staff member) as well as at Caltech (Ed Myers, staff member) and Igor Bargatin, PhD student at Caltech then Post-Doc at LETI for a few months in 2008. Only two representative examples of those measurements are shown below.

The first device is a cantilever and is entirely covered by the metal layer, and the single loop is used for both actuation and detection. There is of course a large background due to temperature dependent resistance of the loop. Signal amplitude is less than a μV with 40mV bias and drive, with a total noise around a few $nV.Hz^{-1/2}$, which yields a mass resolution of a few ag (@100ms integration time), like expected by the model.

The second device is a two-loop cantilever, allowing to separate actuation and detection. Using two separate loops allows for an improvement of the signal to background ratio by a factor 100. This is mainly due to the fact that in the 1-loop device, the motional signal is masked by the resistance change induced by temperature variations in the loop. Typical quality factors are 10 in

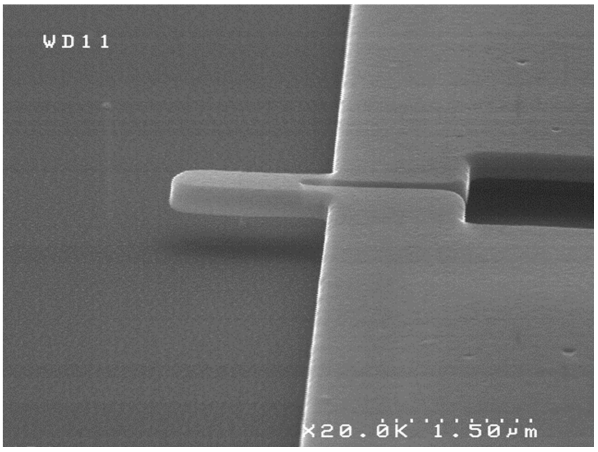

Fig. 3.6 – SEM picture of a simple loop, 1.5μm long, 600nm wide cantilever.

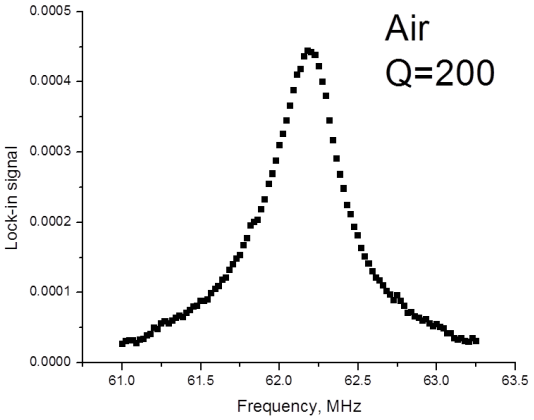

Fig. 3.7 – Electrical resonance in air obtained with downmixing ; signal is in V, with a 1000 gain preamplifier.

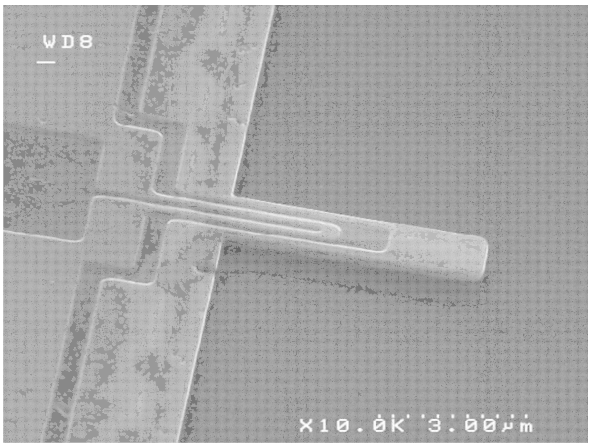

Fig. 3.8 – SEM picture of a double loop, 5μm long, 1.2μm wide cantilever.

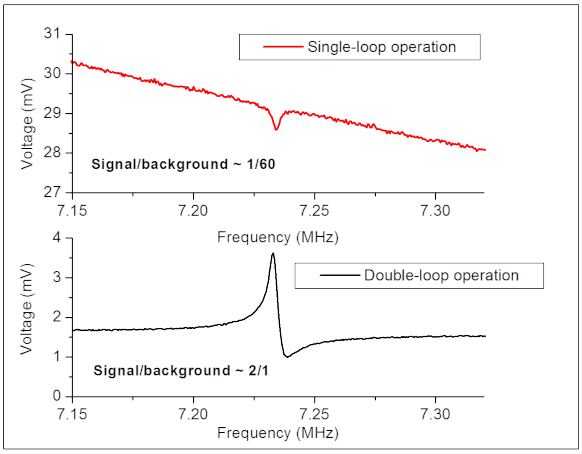

Fig. 3.9 – Electrical resonance in vacuum obtained with downmixing ($40mV_{bias}$ and $40mV_{drive}$) ; signal is in mV, with a 1000 gain preamplifier. Top graph is electrical resonance using only one of the two loops for both actuation and detection, and the bottom graph is the same device using the two loops

air (for those slendered devices) and 2000 in vacuum. For this device, one-loop operation yields a mass resolution around 40ag, whereas two-loop operation gives a few ag (in vacuum).

Nevertheless, it looked like the piezoresistive as well as overall electric behaviour of Aluminum Silicon was not as good as we could have hoped for, and was nothing close to be as good as gold. Signal amplitude was very weak, parasitic peaks and high background made electrical identification of resonance very difficult. Several paths were investigated to mitigate these results: change in transduction and array devices.

3.2.3 Semiconductor piezoresistive devices

Several people worked on this topic: the design was initiated by Sébastien Labarthe, PhD student at LETI, fabrication was followed by Carine Marcoux, and characterization was performed by Ervin Mile, PhD student at LETI, as well as Igor Bargatin and Guillaume Jourdan, both post-doc (Mile *et al.* 2010).

The device structure (named Xbeam) originated from opposite arguments leading to metallic gauges, and the ability to fabricate at LETI extremely small suspended silicon gauges with controlled doping level. Figure 3.10 shows a typical device: it consists in a cantilever (large dynamic range) with tiny piezoresistive silicon gauges, located close to the anchors. This layout has significant advantages: firstly, the subsequent lever arm allows for a large inertial force amplification on the gauges (the optimal location of the gauges along the cantilever has been evaluated around 0.15 times its length) ; secondly, the symmetric gauge layout allows for a differential measurement: the output signal comes from the central point, at a zero voltage if both gauges are polarized at opposite voltages: the background is reduced to a minimum, and the impedance matching is straightforward with a high impedance. Actuation is performed by an electrostatic gate nearby, polarized with an ω voltage plus a DC one (1f scheme) or an $\frac{\omega}{2}$ voltage (2f scheme). The latter usually yields a lower background, probably because of conductance variation of the gauge induced by proximity of the electrostatic electrode in the 1f case. Figure 3.11 shows a typical 2f downmixing scheme we used.

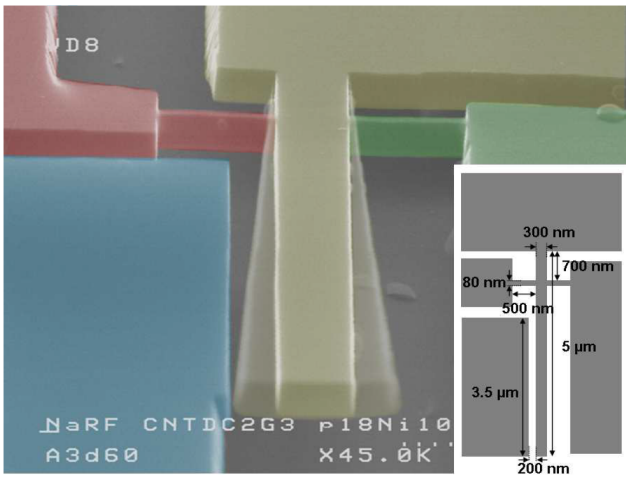

Fig. 3.10 – False colour SEM picture of a Xbeam device, with silicon piezoresistive gauges and typical dimensions

This time, the high resistance (around a few $k\Omega$) semiconductor gauges have a large gauge factor (experimentally evaluated around 40, to be compared with a bulk value of 47 at a doping

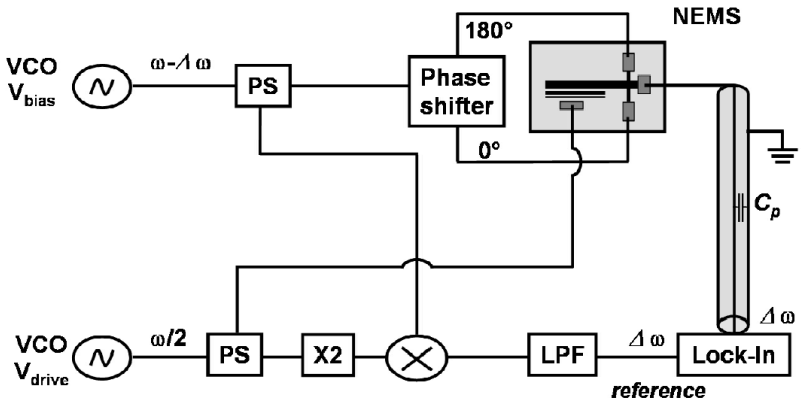

Fig. 3.11 – 2f downmixing scheme used for our Xbeam measurement. Both gauges are polarized with two opposite sign bias voltages at $\omega - \Delta\omega$. The piezoresistor is used as a mixer, and the bias voltage mixes with the resistance variation induced by the mechanical motion at ω. The output signal after filtering is at $\Delta\omega$. 1f scheme is also routinely used with an additional DC voltage for driving; background is somewhat higher with the latter.

level of $1.10^{19}.cm^{-3}$ with this crystalline orientation) and allow for large bias voltages (up to typically 10V before silicon melting). Figure 3.12 shows a resonance peak obtained before onset of NL with V_{drive} and V_{bias} equal to 1.5V in vacuum (less than 1mTorr). Quality factors varied from around 8000 to 12000 (around 200 at ambient pressure). Output signal at resonance *without amplification* is of the order of a few mV, and SBR is around 60dB. Those numbers, well above most of the literature devices of similar size and frequency (Ekinci *et al.* 2004*a*, Li *et al.* 2007, Arcamone *et al.* 2008, Bartsch *et al.* 2012), show how easy of use this device proved to be for measurement purposes. On the other hand, high resistance meant high Johnson noise as opposed to metallic piezoresistors. Thanks to LETI's background in microelectronics, doping processes are very well controlled, in terms of level, dimensions and thickness homogeneity. The doping level controls the trade-off between high gauge factor and high signal (low doping) and low noise (high doping). This trade-off was found around a few $10^{19}cm^{-3}$. With this level, Johnson noise was evaluated at ambient temperature from $\sqrt{4k_bTR}$ around $12nV.\sqrt{Hz}^{-1}$. In order to check that this transduction was good enough to read the thermomechanical noise, following Bargatin *et al.* (2007), we simply suppressed the drive voltage and measured the output amplitude fluctuations. Result is shown figure 3.13 ; two noise density peaks are found, each separated of $\Delta\omega$ from the resonance frequency. From this noise level, thermomechanical noise was evaluated around $18nV.\sqrt{Hz}^{-1}$, and the SNR around 100dB. Those numbers were state-of-the-art and this measurement proved that our readout was as good as it could get, that thermomechanical noise was dominant, above Johnson noise *and* the $1/f$ noise, usually designated as the culprit in piezoresistive devices (Li *et al.* 2007). From equation 2.12, such a SNR should translate in frequency fluctuations around 10^{-9} @1sIT.

To experimentally check this number, an Allan deviation measurement in open-loop was performed (see Mile *et al.* (2010) for details), see figure 3.14. We measured an Allan deviation close to 5.10^{-7} at ambient temperature, which was state-of-the-art (Feng *et al.* 2008), but far from the theoretical value computed from the dynamic range (SNR). I will come back to this important discrepancy in the next chapters. But the actual deviation value translated into a mass resolution

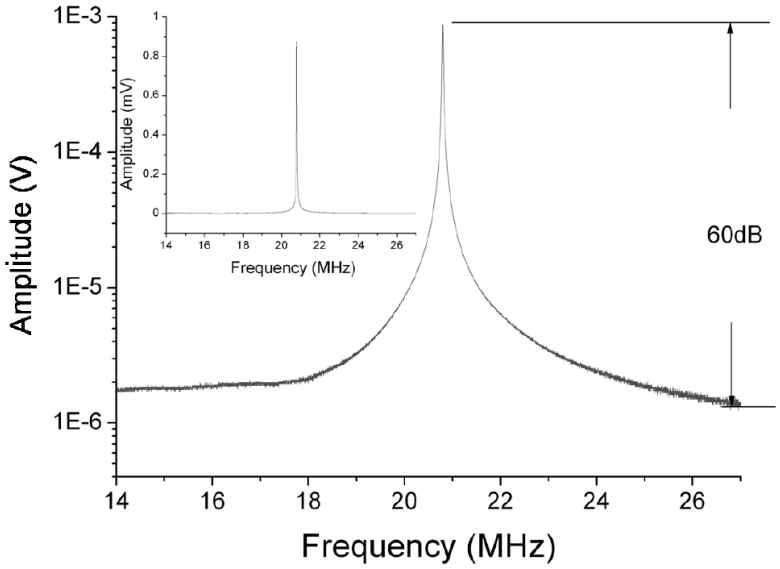

Fig. 3.12 – Typical resonance peak measured with a Xbeam, $V_{drive} = 1.5V$, $V_{bias} = 1.5V$ in vacuum

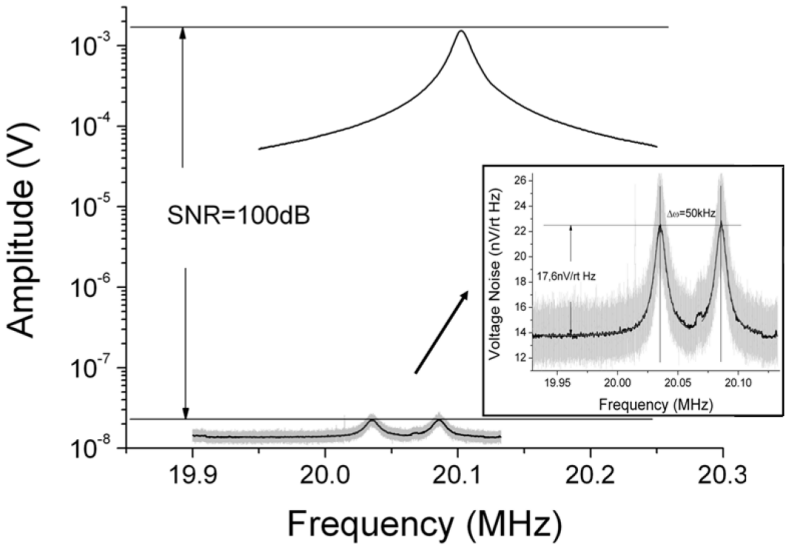

Fig. 3.13 – SNR obtained with $V_{drive} = 1.5V$, $V_{bias} = 1.5V$ in vacuum. Noise is computed for 1Hz bandwidth. Inset shows the two noise density peaks around the resonance frequency.

around 100zg, which again was state-of-the-art for a top-down device.

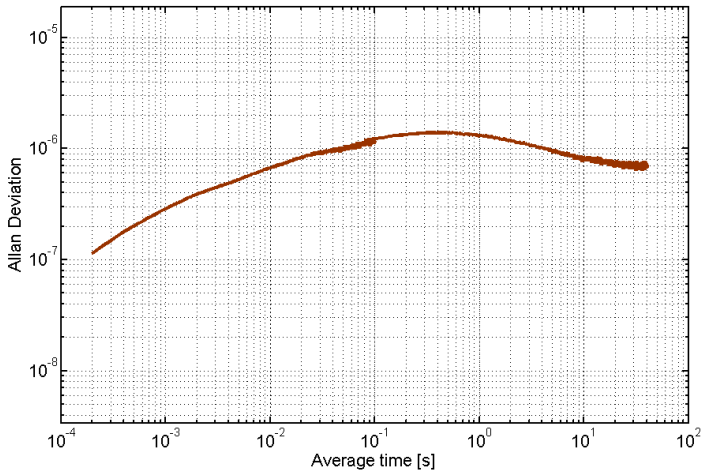

Fig. 3.14 – Open-loop Allan deviation measurement at relatively short integration times.

To briefly conclude, this device has shown outstanding performance and is the achievement of a team gathering multiple expertise: device physics, mechanics, characterization, noise modelling, fabrication. It is this gathering, along with VLSI processes that gives this device the potential to come out of the lab and to be used as a robust real-world sensor. The first application that was considered was multigas sensing: beyond theoretical predictions, we carefully reviewed experimental results in the literature and compared it to NEMS measurements (Fanget *et al.* 2011). It appeared that NEMS was a promising technology in that regards.

Ambient pressure measurements showed a quality factor around 200, an Allan deviation around 10^{-6} at a few 100ms IT, translating into a surface mass resolution above $500zg.\mu m^{-2}$. Both equilibrium experiments with a bubbler gas bench and fast-GC experiments were successfully performed (Arcamone *et al.* 2011). NEMS have the simultaneous advantages of their relatively good resolution obtained at a low integration time compatible with GC operation and their small size, making them ideal to avoid dead volumes, potential killers of GC operation performance. A GC architecture was preferred for real-world multigas analysis, see figure 3.15. Beyond the surface mass resolution alone, relatively good for NEMS, this architecture as well as the VLSI robustness of the XBeam devices, are the underlying motivations for the creation of APIX Technology, a start-up from the Alliance LETI/Caltech: it is today the first industrial NEMS initiative worldwide.

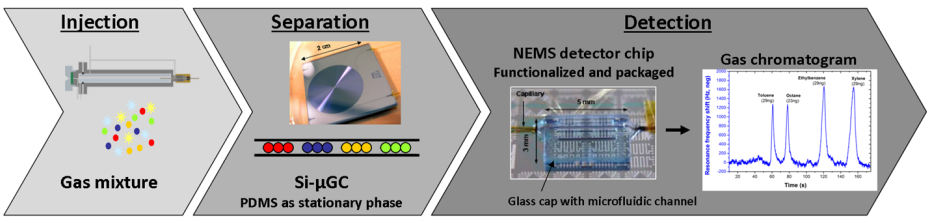

Fig. 3.15 – Schematic representation of a multi-gas analyzer associating a silicon μGC and the Xbeam NEMS detectors

3.2.4 NEMS arrays

Section 3.2.2 has shown the limitations and the fabrication difficulties of the metallic piezoresistive devices. An excellent alternative was described in the last section. Another one we investigated, mainly with Igor Bargatin while he was PhD student at Caltech and later post-doc at LETI, was simply to combine individual NEMS into large arrays as a way to scale up the interaction cross-section with the analyte in the context of gas sensing. VLSI fabrication techniques are particularly relevant to design devices using the collective response of multiple elements: the main argument for such a layout is that in the ideal case where all NEMS are identical, all output signals coherently sum up, and the overall signal scales like N, N being the number of devices within the array; assuming noise sources are uncorrelated from device to device, voltage noise scales like $\sqrt{N}$. The overall gain in SNR would then be $\sqrt{N}$. Figure 3.16 shows a picture of a representative array of metallic piezoresistive devices from a 200mm wafer. Arrays were fabricated with different individual NEMS element dimensions across the wafer with lengths varying between 1.6 and 5 μm, and widths varying between 800 nm and 1.2 μm. A typical array contained 20 rows and 140 columns with a 6.5 μm linear pitch for a total of 2800 array elements. The largest arrays employed in the present work contained 6800 NEMS with an integration density of nearly 6 million NEMS per square cm. The obvious advantage of this first realization with metal piezoresistive devices is the extreme simplicity of electrical connections.

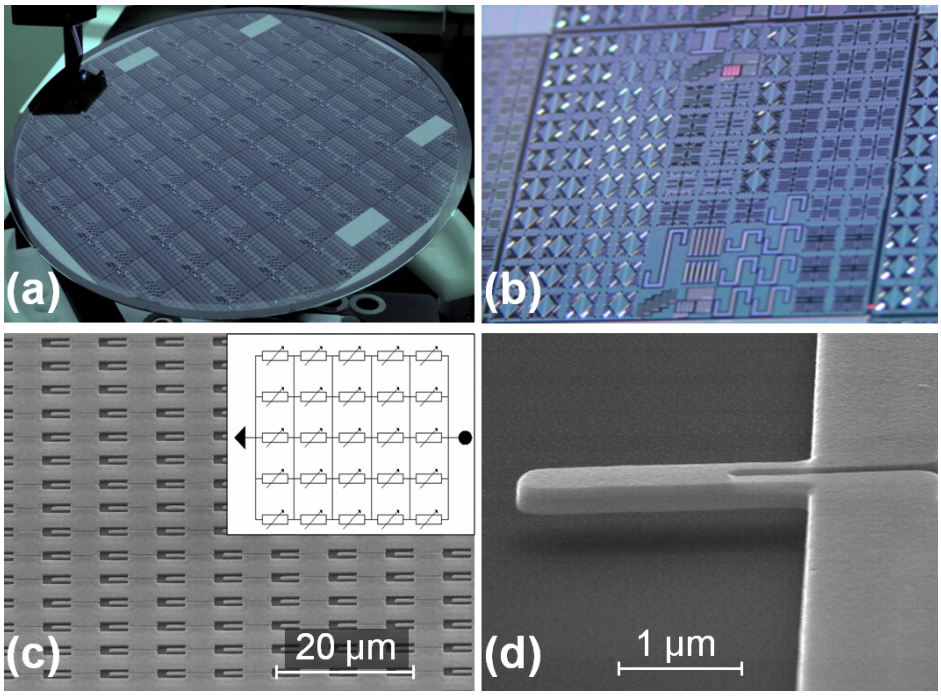

Fig. 3.16 – (a) Photograph of a full 200-mm wafer with patterned NEMS arrays. (b) Zoomed-in photograph of one 20-mm wafer die containing a variety of nanofabricated resonator array structures. (c) Scanning electron micrograph of a section of a cantilever array. Inset: Schematic of a combined series-parallel electrical connection of array elements. (d) Scanning electron micrograph (oblique view) of an individual array component.

A straightforward approach to harnessing the power of many individual NEMS in large-area arrays is to connect them electrically in a combined series-parallel configuration, which ensured the

necessary phase coherence. A single-port (signal and ground) connection to the array can then be made through electrodes on opposite edges of the array, just like an individual device shown figure 3.6. Electrical characterization was performed thanks to a downmixing scheme, with a balanced differential bridge (Ekinci *et al.* 2002) using two separate arrays.

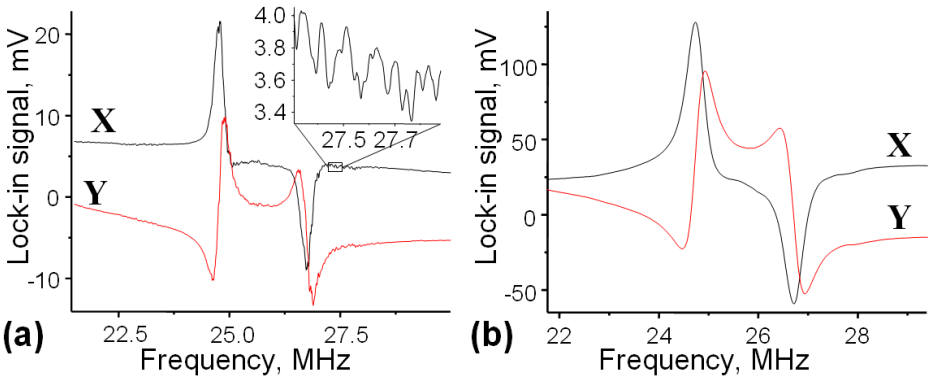

Fig. 3.17 – (a) Resonant response of the two arrays in vacuum. Both quadratures of the lock-in response, X and Y, are shown. The inset shows a zoomed-in version of a part of the measured response curve. The noise level in these measurements was more than an order of magnitude smaller than the amplitude of the rapid variations shown in the inset. (b) Same for measurements in air, with higher drive and bias voltages.

As can be seen on the resonant response figure 3.17, the overall quality factor was around 100 in vacuum and 50 in air, while for the same individual devices, it was around 1000 in vacuum and 100 in air. The reason for this is that in practice, there are some fabrication uncertainties, and the dispersion of resonance frequencies across the array was of the order of 1%, widening the resonant response. The overall quality factor can be expressed as $Q_{eff} = (Q^{-1} + Q_{distr}^{-1})^{-1}$, where $Q_{distr} = \frac{\Delta f}{f}$ describes the widening due to frequency dispersion. As fabrication uncertainties do not depend on feature sizes, the relative frequency dispersion decreases with increasing cantilever length. On the other hand, the quality factor in air decreases with increasing length (Bianco *et al.* 2006). As a result, there is some optimal cantilever length, for which $Q_{distr} \simeq Q_{air}$, and $Q_{eff} \simeq Q_{distr}/2 \simeq Q_{air}/2$. This was roughly the case for a close-to-24MHz array, for which $Q_{distr} \simeq Q_{air} \simeq 100$ and $Q_{eff} \simeq 50$. This was obviously not the case in vacuum, where the overall quality factor was largely determined by the frequency dispersion. Figure 3.18 shows an optical measurement of this dispersion in vacuum within an array: the beam spot was moved across the width of an array. The spot size is roughly $10\mu m$ and contains a dozen cantilevers at a time. Most of the resonances formed the main peak of the array response, with a number of individual resonances outside of this peak.

Electrical characterization and theoretical consideration showed that those devices were perfectly suited for gas sensing experiments, and in particular GC operation like described in the last section. An array was operated in ambient air and the end of GC column was placed thanks to a micropositionner as close as possible to the array. The arrays were coated with a silicone copolymer developed at Sandia National Laboratory for detection of phosphonate gas molecules – precursors and simulants of nerve gas agents, among which DIMP. Solutions of this gas were injected in the column and the array response in open-loop was monitored. Figure 3.19 shows the resulting chromatograms for a wide range of DIMP mass injections, as well as the setup used.

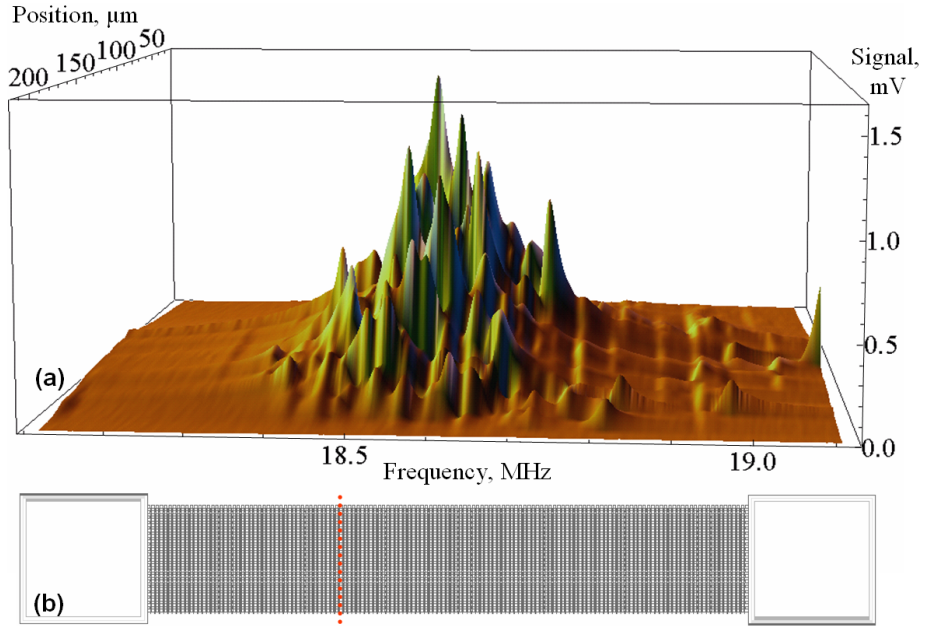

Fig. 3.18 – Optically detected spectrum of cantilevers in a representative array for different positions of the laser spot (spot size approximately $10\mu m$). (b) Top-view schematic of a 140*20 array of cantilevers. Individual cantilevers are not visible in this image. The dotted red line schematically shows the positions of the laser spot used to acquire the spectra.

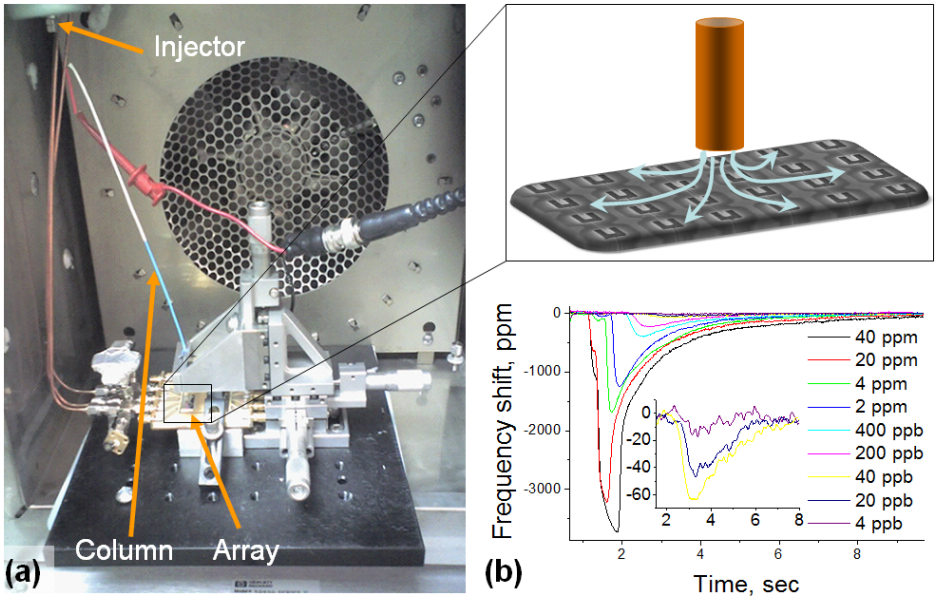

Fig. 3.19 – (a) Integration of the array sensors into a commercial gas chromatography system. The photograph shows the inner chamber of the GC system with the injector, column, and column heating wires as well as the printed circuit board with the sensor arrays and a micropositioner. (b) Gas chromatogram of DIMP obtained with an array sensor in the bridge configuration with 10-Watt resistive heating of the 90-cm-long column. The inset shows zoomed-in versions of the chromatograms for the lowest DIMP concentrations.

In these measurements, the averaging time was 150 ms, corresponding to a bandwidth of $1/(2\pi * 0.15s) \simeq 1Hz$. The rms amplitude of noise corresponds to a frequency shift of 3 ppm and therefore a concentration resolution of approximately 1.2 ppb. This resolution was not any better than previous equilibrium measurements (long integration times) (Li *et al.* 2007), but was an improvement upon fast-GC and short IT measurements, by roughly a factor 30.

Within the array, individual cantilevers had typical resistances around 7Ω, so that 20*140 arrays we typically used had total resistances of $7*140/20 \simeq 50\Omega$, hence optimally matched to commercial power electronics. This is another obvious advantage of arrays, besides an increased power handling, as total RF power we typically used for previous measurements were around 1W. This value shows their robustness, but also does not seem reasonable for low-power devices. This is the reason why a less dissipative, more efficient actuation method was investigated, namely the piezoelectric actuation.

3.3 Piezoelectric transduction at the nanoscale [10]

Piezoelectric transduction seems particularly suited to NEMS for a number of reasons: as opposed to electrostatic transduction relying on displacement, it is a transduction based on stress/strain: its efficiency does not scale with device size. Unlike metal thermoelastic actuation or piezoresistive detection, it is low power as it does dissipate very little power: the dielectric loss may be expressed in terms of the dissipation factor, the ratio between resistive power and reactive power. For piezoelectric materials, the loss tangent δ can be easily as low as 0.1%. Before this work, piezoelectric material-based NEMS had never been attempted. It was conducted within the Alliance and the Carnot-NEMS project, along with Rassul Karabalin, Matt Matheny and Luis Guillermo Villanueva from Caltech, Paul Ivaldi PhD student at LETI (and partially at Caltech) and Paul's advisor, LETI piezoelectric material expert, Emmanuel Defaÿ.

3.3.1 Material

There is much to discuss on this topic, and it is a whole research field. This activity relied on our experts' choices, like E. Defaÿ, and I will only describe the big picture here, as those issues are discussed thoroughly in the literature, like in Defaÿ (2007). In the field of micro-actuators like switches or micro-resonators, the main materials are PZT and AlN, because high piezoelectric coefficients are needed for good actuation ($e_{31} \simeq 1C/m^2$ for bulk AlN and $e_{31} \simeq 10C/m^2$ for bulk PZT). ZnO is less used as it has similar properties as AlN, but is more difficult from a technological point of view. It is also the case of $LiNbO_3$, which has very good piezoelectric properties. PZT has a 100-fold larger dielectric constant than AlN (respectively 1000 and 10), as well as larger dielectric losses ($tan\delta$ can be between a few % and 20% for PZT, while around 0.1% for AlN). For resonant sensing application, this is greatly in favor of AlN, as a large static capacitance masks the motional signal in the background and low dielectric losses should not degrade the quality factor. Moreover, the maximum voltage possible will be three-fold higher with AlN compared to the same PZT thickness because of a higher breakdown field strength. More importantly, we aim at good gravimetric performance, and nano-devices. We needed a material as light as possible,

[10] Details can be found in Karabalin *et al.* (2009), Ivaldi *et al.* (2010; 2011*b*;*a*)

and retaining its high piezoelectric coefficient in ultra-thin layers (below 100nm). This was made possible at LETI thanks to tremendous technological efforts on AlN for RF applications, in a VLSI context and processes compatible with CMOS lines. This progress was interestingly achieved in other groups within a few years, like in in EPFL with degrading piezoelectric properties (Martin *et al.* 2004), or UPenn (Sinha *et al.* 2009). The piezo group at LETI achieved layers below 100nm with no degradation (Karabalin *et al.* 2009). Finally this previous work was key for us, and AlN was the good trade-off between high PZE coupling, low dielectric loss, good mechanical, chemical and thermal stability and compatibility with CMOS processing.

3.3.2 Individual NEMS

A major drawback of piezoelectric transduction is the fact that downmixing cannot be used: indeed, unlike piezoresistive and capacitive actuation, piezoelectricity generates electric charges without the need for a bias voltage. Rather than a passive component which can be used as a mixer, it is an active component. It is then subject to signal shorting by parasitic capacitances. To minimize this issue as much as possible, the "non-active" capacitance (that is, outside of the suspended devices) was reduced to a minimum: a multi-level process allowed for contact to both bottom and top electrodes to a region where AlN has been etched away. For this first attempt, the thin AlN layers were made at LETI, and the process shown figure 3.20 was developed at Caltech.

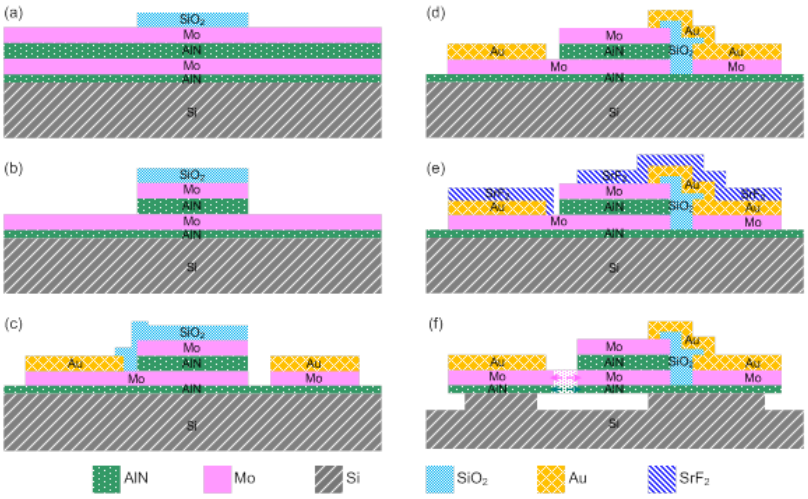

Fig. 3.20 – The multilayer stack comprises Mo/AlN/Mo/seed AlN (100nm/100nm/100nm/20nm) layers on Si. (a) Definition of SiO2 mesa, followed by a Dry etch (b) to remove top Mo and AlN. (c) Au electrodes are patterned and deposited adjacent to the mesa region, along with an SiO2 bridge protecting part of bottom Mo, while remaining bottom Mo removed. (d) SiO2 is stripped and contact is made to the top Mo electrode (including deposition of a SiO2 bridge layer. (e) NEMS devices are defined, using SrF2 as a dry etch mask for both NEMS and all metallic contacts. (f) Anisotropic etching of all the structural layers down to Si by using Ar/Cl2 ICP-RIE is followed by an isotropic Ar/NF3 etch for device release, and subsequent removal of SrF2 mask. The dashed arrows and lightly-hatched areas indicate that the bottom Mo and AlN layers are connected out of the present section plane (passing vertically through the longitudinal axis along a suspended cantilever).

Despite these precautions and much characterization care, the electrical readout was not satisfying and impedance mismatch was really cutting the signal down. Optical interferometry detection

had to be used (see figure 3.21), which still showed how efficient piezoelectric actuation at the nanoscale was: on this figure, the displacement on resonance is 0.5nm with 2mV drive, the onset of NL is reached with very low voltages and a high tunability has been shown (allowing for example for parametric amplification (Villanueva *et al.* 2011)).

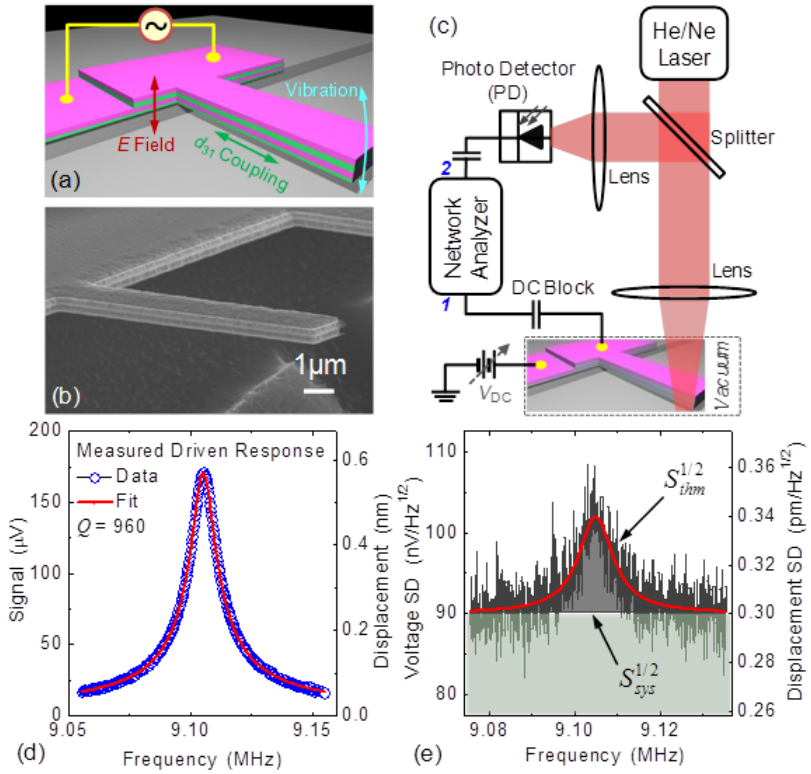

Fig. 3.21 – (a) Illustration of the piezoelectric actuation. (b) An SEM image displaying the 4-layer composite structure of a cantilever NEMS resonator. (c) Simplified schematic of the optical readout scheme (d) A typical resonant response measured from a driven cantilever, with f0=9.11MHz and Q=960, extracted from the fit to the model of damped driven oscillator. (e) Measured thermomechanical noise spectral density from the 9.11MHz device, demonstrating the sensitivities in both electrical and mechanical domains, with contributions from both the NEMS and the detection setup.

As expected, piezoelectric transduction gain is as good as piezoresistive can be, but the impossibility to use a downmixing scheme does not allow its implementation for external readout of individual NEMS devices. CMOS co-integration would solve this issue, by using a nearby transistor for amplification or mixing ; two other altrenatives are being described below: piezoelectric MEMS with large signals and NEMS arrays.

3.3.3 Piezoelectric cantilevers for gas sensing

As discussed section 3.2.1, a number of assumptions lead to the conclusion that the surface mass resolution does not scale with device size. We investigated this fact further within Paul Ivaldi's PhD, whose objective was to make progress with gas sensing experiments with piezoelectric devices in the prospect of scaling up towards arrays. Paul has later been hired by Izatec, Toulouse, France.

As a first conservative approach, Paul started with simple and large (typically a few $10\mu m$ long) cantilevers, comprising the AlN piezoelectric stack as well as an elastic layer (in our case, a silicon

nitride layer), see figure 3.22. In order to find design rules for an optimized surface mass resolution, an analytical electromechanical model was developed. From figure 3.23, one can deduce the output voltage of the device: assuming a differential bridge configuration to get rid of the non-motional current induced by C_0, the piezoelectric stack capacitance at rest (including the signal lines and pads), it is proportional to $\frac{C_m}{2C_0+C_p}$ where C_p is the load capacitance including all parasitics (see figure 3.26). The motional capacitance C_m scales like $\frac{LW^2}{EI_{eq}}\beta^2$ where β is a figure of merit of the actuation efficiency (product of the lever arm and the piezoelectric coefficient e_{31}).

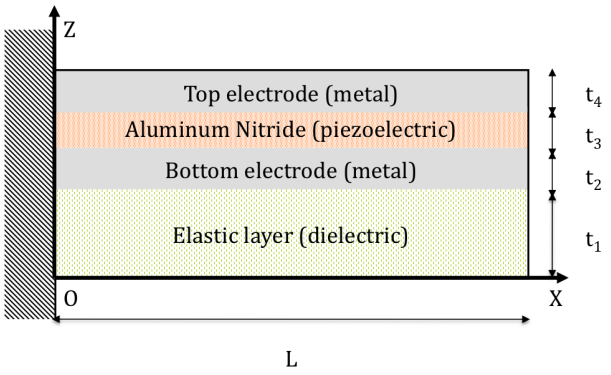

Fig. 3.22 – Structure of a PZE heterogeneous multi-morph system incorporating an elastic layer on top of which a metal PZE layer metal stack is deposited.

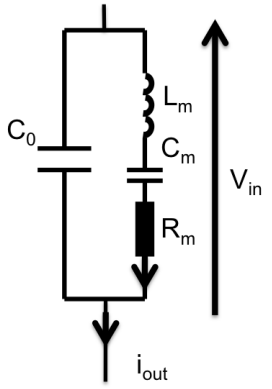

Fig. 3.23 – Butterworth Von Dyke equivalent circuit of the PZE bimorph; the metal insulator/metal capacitance C0 is responsible for the presence of a background current i0; Lm, Cm, Rm represent the motional components arising from the mechanical resonance

Experience proved that the dominant noise within the scheme used was the input electronics noise. Neglecting other sources like thermomechanical noise and using Robin's formula 2.12, one finds the surface mass resolution

$$\delta m_{surf} \propto \frac{\mu}{Q^2 V_{in}} \frac{2 + C_p/C_0}{C_m/C_0} \tag{3.16}$$

where μ is the mass density per unit length and width. From this, a number of comments can be made:

- Of course, the product drive voltage by quality factor should be maximum. In the viscous regime, the quality factor, at the square power, scales like $\frac{Wt^2}{L^2}$ (Bianco *et al.* 2006). Moreover, the drive should be limited by the onset of non-linearity, scaling like $\frac{L}{\sqrt{Q}}$ (Kacem *et al.* 2010). Both those facts should be introduced in the scaling laws, but these theoretical expressions did not account very well with our observed Q (which has a large variability, I'll come back to it later) and onset of NL, way lower than expected. We will consider in the following they do not scale.

- Without much surprise, μ must be made minimum: overall thickness should be minimum, and in particular those of the heavy metallic electrodes.

- Again, as the measurement is homodyne, the load capacitance shortens the signal and it is of primary importance to reduce the parasitic capacitance C_p relatively to the static capacitance C_0. This can be achieved with electronic as close as possible to the device. In the range where the parasitic capacitance dominates over C_0, then the larger the device in-plane, the better the resolution, up to a limit given by fabrication issues. This is not the commonly accepted conclusion.

- The motional capacitance C_m should be maximized relatively to the static capacitance C_0. Reducing the surface of the mechanically non active areas can be done at the cost of additional process steps (see for example figure 3.20). When this is achieved, the ratio $\frac{C_m}{C_0}$ depends only on the layer distribution and a trade-off exists for the thickness of the elastic layer: indeed, if it is too thin, the lever arm becomes too small (β) and the actuation efficiency collapses. If it is too thick, the overall cantilever becomes too stiff to be actuated. Figure 3.24 shows the optimum elastic layer thickness for a given AlN layer thickness.

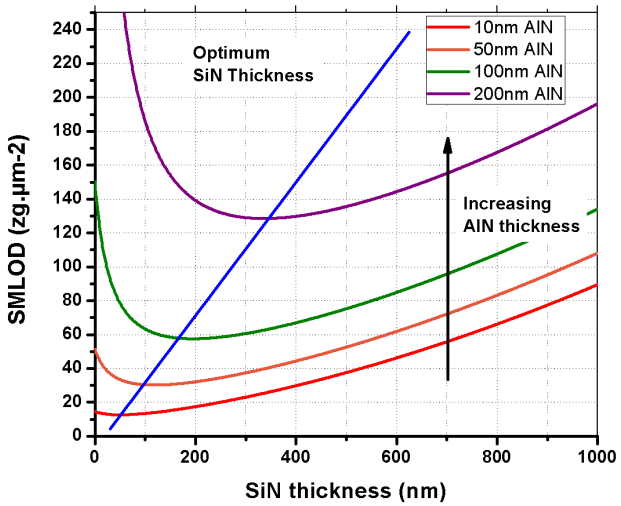

Fig. 3.24 – Surface Mass Limit of Detection (SMLOD) as a function of the SiN layer thickness and for different AlN layer thicknesses. For comparison with experimental results, the bottom and top electrode thicknesses are equal to 100nm and 25nm respectively, the parasitic capacitance is dominant and equal to 100pF and the actuation voltage, quality factor, measurement bandwidth and the dominant noise are equal to 750mV, 100, 0.1Hz and 5nV/$\sqrt{\text{Hz}}$ respectively.

From the comments above, besides increasing the in-plane dimensions of the device, key to the improvement of the gas resolution is the reduction of the thicknesses, and in particular the piezoelectric layer. A lot of time and effort has been devoted at LETI and elsewhere in the past decade to finding reliable AlN deposition techniques. DC magnetron reactive sputtering is the most widely used now and had demonstrated its capability to produce good quality AlN layers of 100nm thick. Thanks to developments led at LETI for the BAW technology, it proved possible to produce 50nm thick and below AlN layers with excellent piezoelectric properties, which is what we used for our gas sensing cantilevers, and was a first. The presence of residual stresses within the layers is a strong constraint design-wise in particular at these low thicknesses, which is why we stepped away from the optimal layer distribution and used a 600nm thick SiN layer to be conservative. A careful balance with DC power tuning allowed Paul to obtain devices with very low initial deflection.

Figure 3.25 shows a representative device and its fabrication process, performed at the sample level in the Minatec "PTA" (smaller, more flexible) clean room. This partly explained the relatively large variability in Q in particular, as process conditions could vary from batch to batch, like the release depth for example.

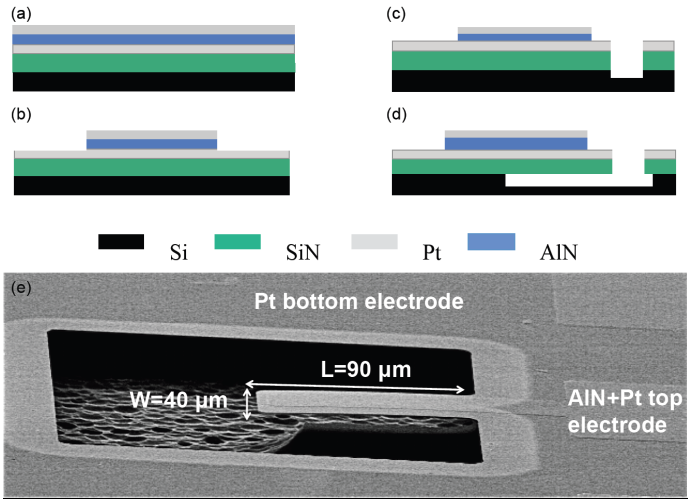

Fig. 3.25 – Fabrication process: (a) full sheet deposition of SiN (600 nm)/Pt (100 nm)/AlN (50 nm)/Pt (100 nm) stack on 200 mm Si wafers; (b) first lithographic step and ion beam etching (IBE) of the top Pt and AlN layers; (c) second lithographic step and subsequent IBE and reactive ion etching (RIE) of the bottom Pt and SiN elastic layer; (d) rapid thermal annealing (RTA) and XeF2 isotropic etching of the Si substrate and (e) SEM picture of the fabricated cantilever.

Figure 3.26 shows the electrical scheme that was used, taking advantage of a "dummy" cantilever, identical but not released to cancel out the static capacitance. An almost perfect Lorentzian response is obtained (figure 3.27) with an excellent fit of the analytical model. The quality of the measurement is further shown by observing higher frequency peaks up to 20MHz; figure 3.28 shows the first four flexural peaks. The maximum actuation voltage was found to be close to 750mV, above which stiffening occurred. This corresponds to a cantilever displacement around 110nm, well below the theoretical limit. I suspect an effect of the residual stresses distribution, but the origin of this effect is still unknown.

Those good electrical performance encouraged us to go one step further and assess the frequency stability of this device, see figure 3.29. An Allan deviation measurement was done in open loop at a set frequency while phase variations were recorded, for integration times varying from 10ms to 100s. Up to 10s, the slope of the Allan deviation is $-\frac{1}{2}$, consistent with a dominant additive white noise, and its level fits very well with our LIA input noise ($5nV.\sqrt{Hz}^{-1}$) and Robin's formula 2.12. An excellent deviation of 10^{-8} was measured, demonstrating the performance of our piezoelectric layer and transduction. The expected surface mass resolution expected from this frequency stability is around $50zg.\mu m^{-2}$, which is still today state of the art, to be compared to a few 100 for NEMS (Li *et al.* 2007; 2010) or around 80 for arrays of CMUTs (Lee *et al.* 2008) for example. This number was exceeded only by a complex 1GHz AlN bulk resonator, packaged with a CMOS circuit ($35zg.\mu m^{-2}$ by Rinaldi *et al.* (2011)). In contrast our result was obtained with a simple 100kHz cantilever and external circuitry, but at a higher integration time (10s to be compared to 1ms). Knowing that our device was far from the optimal design, 1 to 2 orders of magnitude improvement in the LOD is

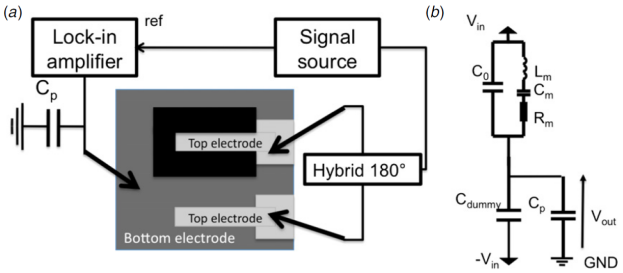

Fig. 3.26 – (a) On chip capacitive bridge used for frequency response characterization. The output signal is taken from the common bottom electrode and detected by the lock-in amplifier through the parasitic capacitance of connectors and cables. (b) Electrical equivalent network of the capacitive bridge using BVD representation of the PZE cantilever.

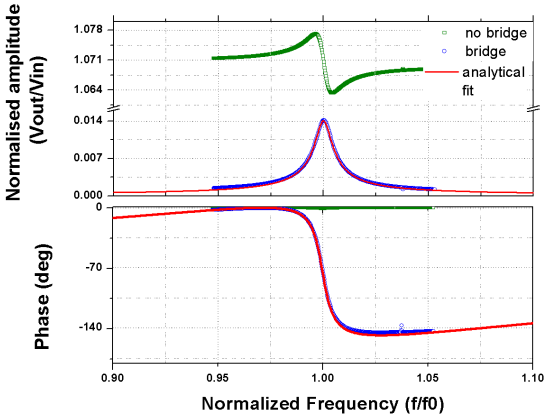

Fig. 3.27 – Electrical amplitude and phase of the first resonant mode of a 50 nm AlN film-based PZE microcantilever resonator, with and without capacitive bridge background compensation and fit with the analytical model. Note the almost undetectable phase jump in the case of no bridge.

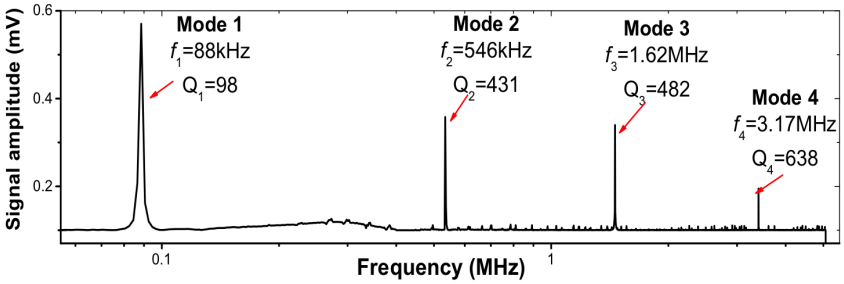

Fig. 3.28 – Frequency response of a 50 nm AlN film based PZE microcantilever resonator, the observed four resonance peaks correspond to the first four flexural modes of the cantilever. Theoretical resonance frequencies are 92 kHz, 578 kHz, 1.62 MHz and 3.17 MHz.

expected with geometry changes, and it will be possible to use lower ITs with similar performance.

This performance was further investigated by gas sensing experiments, performed at Caltech during Paul's 6-months stay there as a visiting PhD student (he was recipient of a Fulbright Program grant): first a PLL frequency tracking circuit was developed using the circuit by controlling the resonance frequency of the source in order to keep the phase signal of the lock-in amplifier at 0 thanks to a SIMULINK program. The PLL digital corrector was designed using $H\infty$ loop shaping (Kharrat *et al.* 2008), with 1s IT.

Similar functionnalization layers and gases as in section 3.2.4 were used: the cantilevers were coated with DKAP silicon polymer by drop-deposition and air-drying, a polymer having a strong affinity towards organophosphates (Li *et al.* 2010) . A thickness of 5nm was deduced from the subsequent frequency shift. This number could be increased by an order of magnitude considering the device thickness (hence improving the partition coefficient and the surface mass resolution by as much). Equilibrium experiments were performed thanks to a bubbler-based gas delivery system, see figure 3.30.

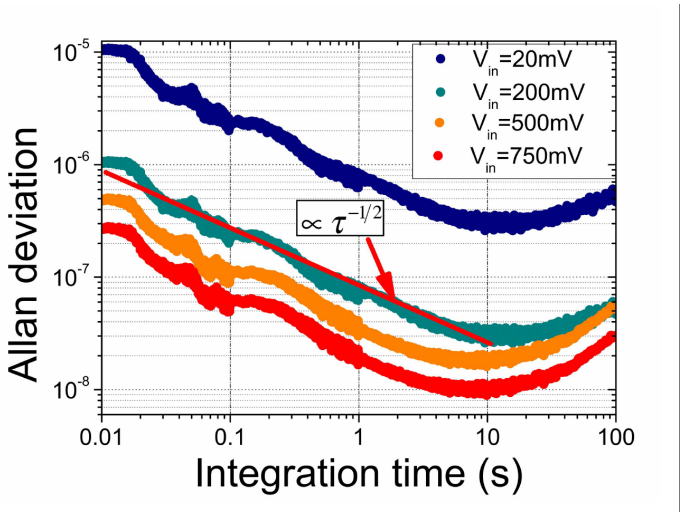

Fig. 3.29 – Allan deviation of a 50 nm thick AlN film-based PZE microcantilever for integration time between 10 ms and 100 s and input voltage between 50 mV and 750 mV (measured onset of nonlinearity).

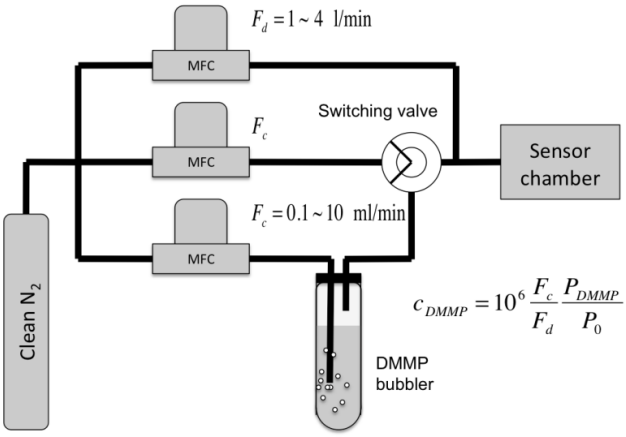

Fig. 3.30 – Schematic of the DMMP vapor delivery setup. A saturated mixture of N2 and DMMP is produced at the outlet of the bubbler with a controlled mass flow Fc and then diluted in pure N2 flow Fd. The concentration of DMMP is controlled by controlling the dilution ratio Fc/Fd thanks to a mass flow controller (MFC).

This time, the experiments were performed with another phosphonate compound, the Dimethyl methylphosphonate (DMMP), a simulant for sarin training exercises and for calibration of detectors, harmful if inhaled. Figure 3.31 presents the response of two devices, one without coating, and another one with DKAP coating, to decreasing DMMP vapor concentration down to 25 ppb: we believe our lod is lower, but a higher total flow rate would have to be used to reach lower DDMP concentrations ; above this value, extra noise appears which we attributed to perturbations of the cantilevers by flow turbulences. Notably the resonance frequency of our cantilever is fairly stable over the 12 hours non stop measurement and recovers its initial value when the exposure to DMMP vapor is turned off. However an important difference between the fall (roughly 30 s) and rise time (up to 15 min) can be observed. This was tentatively attributed to the chamber design which does not provide a laminar flow at the gas exhaust.

We also investigated the response of our system over a large range of concentrations, see figure

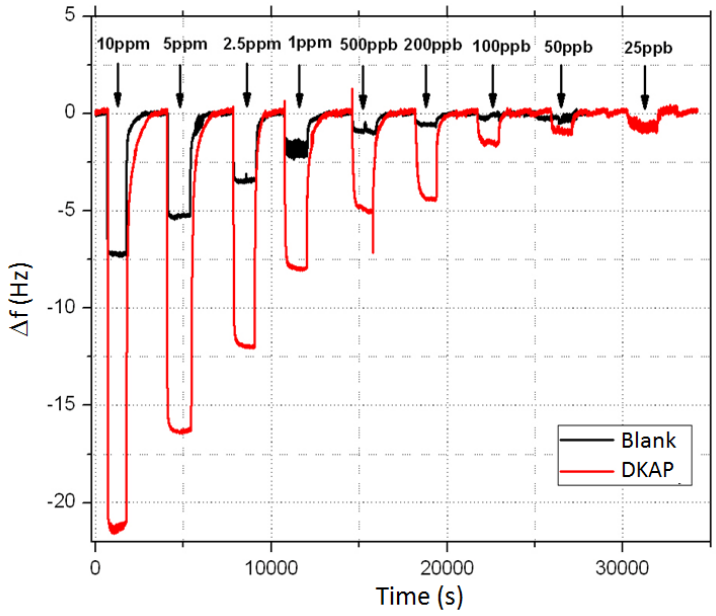

Fig. 3.31 – Transient frequency response of the DKAP coated 50 nm thick AlN film based cantilever, as well as of the blank (no coating) device, under DMMP vapors with concentration from 10ppm down to 25ppb. The RMS frequency noise sets the resolution of the DMMP vapors sensing system to 10ppb. A constant drift of the resonance frequency of $0.1Hz.h^{-1}$ has been removed numerically.

3.32. The frequency shift versus concentration curve is relatively linear for low DMMP concentration and saturates for concentrations higher than 1 ppm. This saturation should be attributed to the extremely low thickness of the DKAP and the concentration range may be largely extended by increasing the DKAP thickness (by roughly an order of magnitude). In the linear regime, the concentration sensitivity is 28 mHz/ppb from which we can deduce a DKAP/DMMP partition coefficient of 2.10^4. This low value explains the little difference between responses with and without coating in figure 3.31. This is more than 2 orders of magnitude smaller than values reported in Li *et al.* (2010) (1.10^7 for DIMP), and is explained by the use of an old DKAP solution and the fact that organic polymers degrade with time. Nevertheless, the minimum demonstrated DMMP concentration (25 ppb) is state of the art (Li *et al.* (2010) have reported 100ppb) and the ultimate concentration resolution calculated from the RMS frequency noise (10 ppb) is not far from the best one reported (800ppt by the same group).

In conclusion, thanks to the excellent piezoelectric qualities of the ultra-thin layers of AlN developed at LETI (<50nm), our simple VLSI-compatible cantilevers have shown among the best surface mass LOD around $50zg.\mu m^{-2}$, almost an order of magnitude better than our VLSI NEMS (section 3.2.3, around several $100zg.\mu m^{-2}$), and similar to metal piezoresistive NEMS (Li *et al.* 2010) and piezoelectric bulk-mode devices (Rinaldi *et al.* 2011), despite a design far from optimal. They have also demonstrated a DMMP concentration LOD at equilibrium among the best in the literature (25ppb), despite a degraded functionalization layer. Nevertheless, they show their best performance at relatively long ITs and the LOD degrades at higher speed, which is required for fast-GC operation. As there is a lot of room for design improvement, we are confident that higher frequency devices would allow us to find the necessary trade-off between speed and resolution.

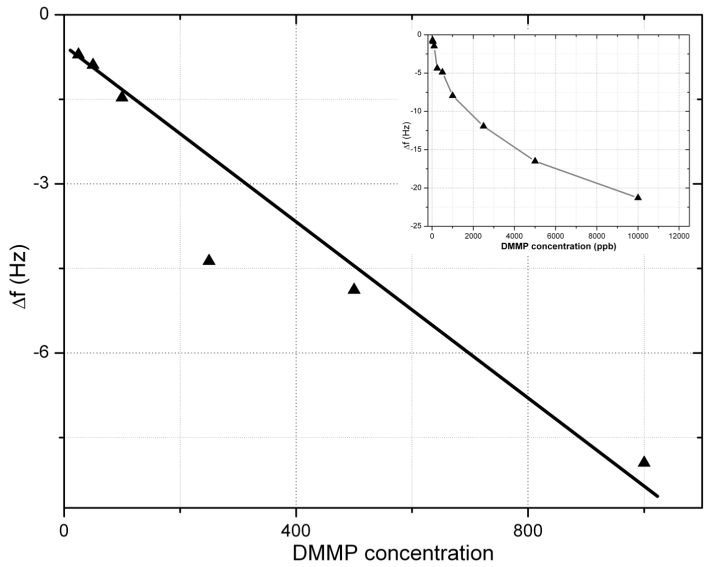

Fig. 3.32 – Frequency shift versus DMMP concentration curve for low concentrations (in ppb). The response of the sensor is linear in this range of concentration with a sensitivity of 28 mHz/ppb. Inset: higher DMMP concentration regime showing a saturation of the sensor response.

3.3.4 Towards piezoelectric NEMS arrays

Following section 3.2.4, one of the motivations for going to PZE NEMS was their layout in large collective arrays, in particular for gas sensing. They promised to cumulate the metal piezoresistive transduction advantages like integrability, low noise, high efficiency and low power, while the signal summation brought by the collective layout would compensate for the impossibility to use down-mixing and help with impedance matching. In this frame of mind, we used the same set of masks as in section 3.2.4 with a fabrication process derived from the previous section (see figure 3.33).

The chosen material stack consists in AlN (50 nm) / Mo (50 nm)/ AlN (50 nm) / Mo (25 nm) deposited on a Si wafer with a thermally grown $2\mu m$ thick oxide. According to figure 3.24 it is close to the optimum thickness distribution with respect to surface-mass sensitivity. Beside, the change of electrode metal from Mo to Pt was motivated by the good piezoelectric properties obtained with this stack, but also by contamination issues that forbid the use of Pt in LETI's 200mm clean rooms. As opposed to the micro-cantilever process, the whole stack is patterned during the first step. Also a 700 nm thick SiH4 hard mask is deposited and patterned prior to IBE in order to improve patterns conformation and avoid the solidification of the photoresist. The second lithographic step is used to remove the top electrode and AlN layer and access the bottom electrode on the large pads next to the samples areas. This second lithography IBE step was performed at the sample level in the Minatec "PTA" (smaller, more flexible) clean room. Finally, samples are released using vapor HF isotropic etch of underlying SiO2.

Figure 3.34 shows SEM pictures of the fabricated nano-cantilevers. Two etching angles have been attempted for the first IBE step, 45 and 90°. Only the 90° etching angle allowed for feature sizes down to $0.4\mu m$ with steep walls. Unfortunately, etched materials have redeposited on the wall side and form visible residues after the release step. Noteworthily, all fabricated cantilevers are straight and fully released even though no special efforts were dedicated to the control of static stress. Neither AlN nor Mo have been etched during the HF vapor process while the SiH4 hard mask

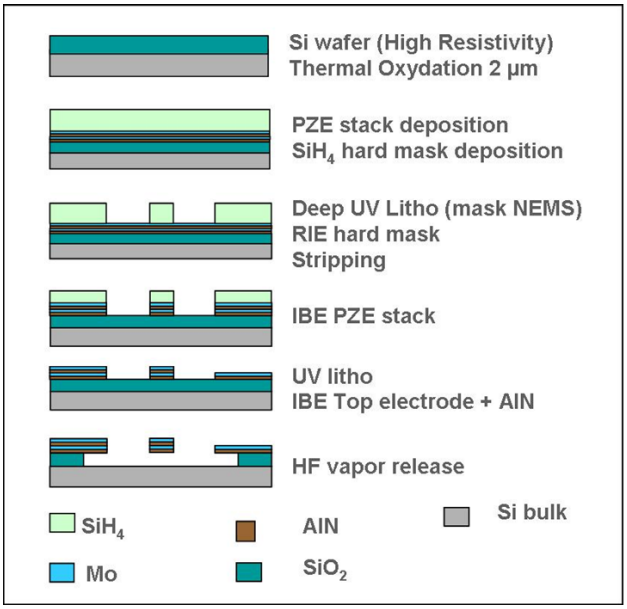

Fig. 3.33 – PZE NEMS array fabrication process.

has been completely removed. Unfortunately, 45°-etched devices were all electrically short-circuited and 90° devices present a very low leakage resistance between the top and the bottom electrodes (on the order of a few 100Ω). Such leakage resistance level is however too high to be explained by electrical breakdown of the AlN and most certainly the short circuit can be explained by the presence of the IBE residues. The IBE etch could be further optimized for example by looking for the etching angles that insure proper patterns conformation and limit material redeposition. SF6 plasma flash might also be investigated as residue removal process step. But an additional deep UV step in order to enlarge the bottom electrode patterns is certainly an efficient strategy. Those are leads that should be investigated in the future for the next PZE arrays. Piezoelectric arrays display several attributes making them ideal for several applications like gas sensing: out-of-plane motion, compacity and density, easy connection for collectively addressed arrays and ensemble-averaged signal. Also, they allow for piezoelectric actuation and metallic piezoresistive detection (with only the top electrode for example).

3.4 Conclusion

This chapter has described the efforts of a team, including LETI people and Caltech people over a number of years. Those efforts have contributed in shifting NEMS from laboratory devices to real-life devices in a VLSI context. Even though frequential sensing needs good frequency stability for good performance, the weak power handling capability of NEMS did not make them adapted to clock generation, at least for individual devices. Gravimetric sensing is often mentioned as the prime application for NEMS in terms of LOD, which is true for punctual mass sensing, but not necessarily in the regime where there is homogeneous covering of the surface, like for gas sensing: indeed, state-of-the-art measurements have been obtained with bulk resonators in the literature as well as with MEMS cantilevers at LETI. As for transduction, metallic piezoresistive devices, even though they had shown outstanding performance with extremely careful characterization in the lab, have proved

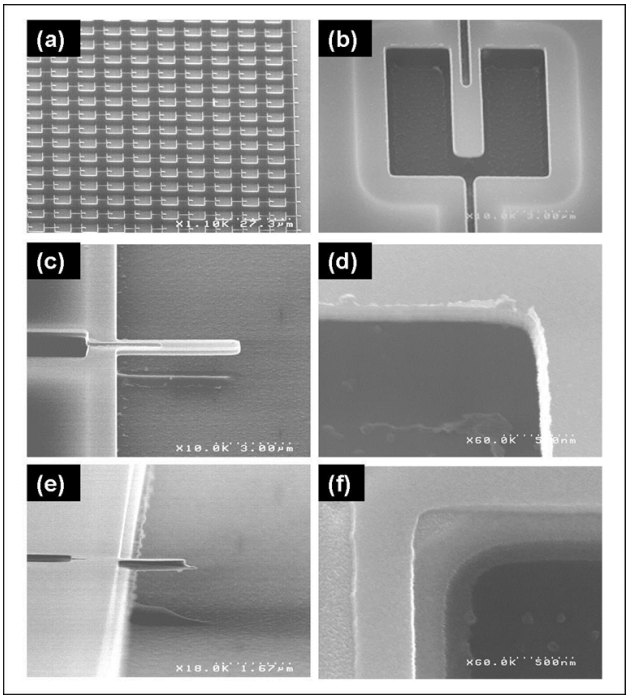

Fig. 3.34 – SEM micrograph of PZE nano-cantilever (a) array of nano cantilever (b) zoom on a single of the array (c) tilted view of a nano cantilever etched (IBE) with an angle of 90° revealing the presence of etching residue on the cantilever side (d) zoom on the residues (e) tilted view of a nano-cantilever with an angle of 45° . (f) zoom on a wall with a large slope of 40° with respect to the substrate.

complex -unreasonable?- to fabricate with 200mm processes, as well as delicate electrical handling and measurement. Two alternatives were investigated: i) silicon piezoresistive devices: as opposed to their metallic counterparts, their power handling capability was much higher, as well as their output signal, which made them robust alternatives. Moreover, they showed excellent SBR, SNR and frequency stability, with a fairly easy VLSI process. For all those reasons, they were chosen as the first detector of a multi-gas analysis architecture, potential first product of the start-up company APIX Technology. ii) the second alternative came with the idea to implement metallic NEMS devices in collectively addressed arrays. A nice feature of those arrays were their robustness coming from device redundance, besides their sensing performance enhancement. Because of power consumption, metallic transduction is ill-suited to large array operation, and piezoelectric transduction at the nano-scale was investigated. This effort was made possible thanks to LETI's know-how in ultra-thin piezoelectric layers. This transduction is particularly interesting, as it is compatible with CMOS processes, and it is very similar in operation to thermoelastic/piezoresistive transduction: it is strain-based and is still efficient at small dimensions. On the other hand, it does not allow for heterodyne schemes. Ultra-thin piezoelectric AlN cantilevers with large in-plane dimensions were fabricated, electrically characterized and tested under gas. They have shown excellent frequency stability and state-of-the-art or better surface mass resolution and equilibrium gas concentration resolution, despite much room for improvement. A test array was fabricated but IBE step has induced redeposition, short-circuiting the devices with such small dimensions. Nevertheless, this effort has shown how promising the piezoelectric transduction was for NEMS and NEMS arrays. CMOS-integration should make it one of the most efficient transduction at the nano-scale.

Chapter 4

Non-linear dynamics of MEMS and NEMS

4.1 Introduction

Many times throughout what is preceding in this manuscript were non-linearities mentioned. It is true that axial stretching due to large transverse vibrations in a doubly-clamped beam is well-known to lead to a stiffening non-linearity in the frequency response of a device (Postma *et al.* 2005). The following work was mainly performed by Najib Kacem, PhD student, co-supervised at LETI and by Sébastien Baguet and Pr. Régis Dufour at INSA de Lyon. Najib is now Maître de Conférences at FEMTO, Besançon, France, on a Chaire d'Excellence. The work was motivated by complex behaviors we observed during our electrical measurements, behaviors we could not always understand. More importantly, this work was also motivated by performance improvement. If we get back to Robin's formula:

$$S_\omega(\omega) = \left(\frac{\omega_0}{2Q}\right)^2 \frac{S_x(\omega_0)}{P_0} \tag{4.1}$$

where P_0 is the displacement carrier power, ie the RMS drive amplitude of the resonator $\frac{1}{2}a^2$.

The frequency noise is inversely proportional to the signal-to-noise ratio, that is, expressed in the mechanical domain, the frequency stability is proportional to the drive amplitude of the device, and inversely proportional to the amplitude noise. Much effort has been devoted to reducing noise in the community, and the drive amplitude is usually set somewhere below the onset of NL or is given by the maximum voltage available. Very little had been done about what are the inherent limits of the drive amplitude, and how it can be tuned (Tilmans & Legtenberg 1994, Kozinsky *et al.* 2006). Interestingly though, MEMS and NEMS have also opened up a whole new experimental window into the study of the nonlinear dynamics of discrete systems like micro and nanoresonators: high frequency and relatively weak dissipation, beside keeping transients so short as to make them difficult to observe, make M/NEMS amenable to small perturbation theory and hence quantitative study. An excellent review of many works on the subject can be found in Lifshitz & Cross (2008): almost all of them deal with the Duffing resonator, or parametrically excited Duffing resonators, or arrays of such coupled devices.

We had a particular interest in devices where non-linearities originated from an external poten-

tial, like an electrostatic gate, present either for detection, actuation or else for tuning. This was because this kind of non-linearity made the device dynamics richer and more complex. As a very good and representative example, Kozinsky *et al.* (2006) used a nonlinear model with a third order Taylor series expansion of the electrostatic forcing applied to a nanoresonator in order to tune the effective Duffing coefficient using an external electrostatic potential. The Taylor expansion leading to a Duffing model is very common in the literature, and a first question was the domain of validity of this approximation.

4.2 Higher-order non-linearities in doubly-clamped beams

4.2.1 Chosen approach and its limits of validity [1]

Figure 4.1 shows a schematic of the most simple electrostatically actuated doubly clamped beam.

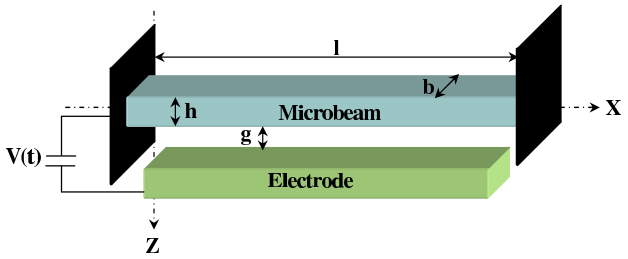

Fig. 4.1 – Schematic of a one-port electrostatically actuated beam

The equation of motion that governs the transverse deflection $\tilde{w}(\tilde{x},\tilde{t})$ is written as

$$\rho bh\frac{\partial^2\tilde{w}}{\partial\tilde{t}^2}+\tilde{c}\frac{\partial\tilde{w}}{\partial\tilde{t}}+EI\frac{\partial^4\tilde{w}}{\partial\tilde{x}^4}-\tilde{N}(t)\frac{\partial^2\tilde{w}}{\partial\tilde{x}^2}=\tilde{F}_e \tag{4.2}$$

where $\tilde{N}(t)$ is the axial tension force

$$\tilde{N}(t)=\tilde{N}_0+\frac{Ebh}{2l}\int_0^l\left[\frac{\partial\tilde{w}(\tilde{x},\tilde{t})}{\partial\tilde{x}}\right]^2 d\tilde{x} \tag{4.3}$$

$\tilde{N}_0$ results from the material residual stress or the effect of the applied axial load, controlling the natural frequency of the micro-beam. The second term is the non-linear part due to stretching effects. The right-hand side of equation 4.2 corresponds to the parallel-plate approximation of the electric force including the edge effects by means of the coefficient C_n (Nishiyama & Nakamura 1990)

$$\tilde{F}_e(\tilde{x},\tilde{t})=\frac{1}{2}\varepsilon_0\frac{bC_n\left[V_{dc}+V_{ac}\cos(\tilde{\Omega}\tilde{t})\right]^2}{(g-\tilde{w})^2} \tag{4.4}$$

Boundary Conditions (BC) should be added to complete the set of equations.

After proper normalization (see Kacem *et al.* (2011*b*) for details), one has to solve the following PDE:

$$\frac{\partial^2 w}{\partial t^2}+c\frac{\partial w}{\partial t}+\frac{\partial^4 w}{\partial x^4}-\left[N_0+\alpha_1\int_0^1\left(\frac{\partial w}{\partial x}\right)^2 dx\right]\frac{\partial^2 w}{\partial x^2}=\alpha_2\frac{[V_{dc}+V_{ac}\cos(\Omega t)]^2}{(1-w)^2} \tag{4.5}$$

[1] Details can be found in Kacem *et al.* (2011*b*)

Neglecting the static deflexion, the Galerkin decomposition method is used as usual on linear undamped mode shapes:

$$w(x,t) = \sum_{k=1}^{N_m} a_k(t)\phi_k(x) \tag{4.6}$$

where $a_k(t)$ is the k^{th} time varying generalized coordinate and $\phi_k(x)$ is the k^{th} linear undamped eigenmode solution of

$$\frac{d^4\phi_k(x)}{dx^4} = \lambda_k^4\phi_k(x) \tag{4.7}$$

Using the BCs, the mathematical form of the eigenmodes is given by

$$\phi_k(x) = A_k\left\{\cos\lambda_k x - \cosh\lambda_k x + \left[\frac{\cosh\lambda_k - \cos\lambda_k}{\sin\lambda_k - \sinh\lambda_k}\right][\sin\lambda_k x - \sinh\lambda_k x]\right\} \tag{4.8}$$

with the λ_k solutions of the transcendental equation

$$1 - \cos\lambda_k \cosh\lambda_k = 0 \tag{4.9}$$

These functions are a modal basis for the scalar product

$$\langle u, v\rangle = \int_0^1 u(x)v(x)dx \tag{4.10}$$

and the coefficients A_k are chosen to normalize the eigenmodes such that $\langle\phi_i, \phi_j\rangle = \delta_{ij}$.

The previous equations are straightforward and very commonly used in the literature. Again, in contrast, the electrostatic non-linear forcing term is usually approximated by a Taylor expansion in order to simplify the Galerkin procedure. However, when vibration amplitudes become large, one can wonder if this is still valid. Several options may be considered: firstly, one can use a higher-order expansion, but may end up wondering up to which order that should be done. Another one consists in using approximations of integrals derived from the existence of inverse power law force densities (Juillard *et al.* 2011). We chose to include the complete contribution of the non-linear electrostatic forces in the resonator dynamics without approximation and multiply Eq. (4.5) by $\phi_i(x)(1-w)^2$ like in Younis *et al.* (2003), and explore this method. This has some disadvantages like the non orthogonality of the operator $w^2\dfrac{\partial^4 w}{\partial x^4}$ with respect to the undamped linear mode shapes of the resonator, the increase of the nonlinearity level in the normalized equation of motion (4.5) as well as the incorporation of new nonlinear terms such as the Van der Pol damping. Nevertheless, the resulting equation contains less parametric terms than if the nonlinear electrostatic forces were expanded in Taylor series and the solution of nonlinear problem is valid for large displacements of the beam up to the gap (with a high enough number of modes). The modal projection consists in substituting Eq. (4.6) in Eq. (4.5), using Eq. (4.7) to eliminate $d^4\phi_k(x)/dx^4$ and integrating the outcome from $x = 0$ to 1. Doing so, Eq. (4.5) becomes in matrix-vector form

$$\begin{aligned}
&[\mathbf{M}_0 + \mathbf{M}_1(\mathbf{a}) + \mathbf{M}_2(\mathbf{a})]\,\ddot{\mathbf{a}} \\
&+ [\mathbf{C}_0 + \mathbf{C}_1(\mathbf{a}) + \mathbf{C}_2(\mathbf{a})]\,\dot{\mathbf{a}} \\
&+ [\mathbf{K}_0 + \mathbf{K}_1(\mathbf{a}) + \mathbf{K}_2(\mathbf{a})]\,\mathbf{a} \\
&- [N_0 + \alpha_1 T_2(\mathbf{a})]\,[\mathbf{K}_T + \mathbf{K}_{T1}(\mathbf{a}) + \mathbf{K}_{T2}(\mathbf{a})]\,\mathbf{a} \\
&= \alpha_2\,(V_{dc} + V_{ac}cos\Omega t)^2\,\mathbf{F}
\end{aligned} \tag{4.11}$$

Two different approaches were used to solve this equation: a numerical procedure and a simplified analytical approach.

4.2.1.1 High-order harmonic balance method combined with the asymptotic numerical method (HBM+ANM)

The Harmonic Balance Method (HBM) is commonly used for computing periodic solutions. It consists in assuming a time solution in the form of a Fourier series and comparing/balancing the coefficients of the same harmonic components. In this way, non-linear differential equations in the space variables and time are transformed into a non-linear algebraic system in the space variables and frequency. However, when non-linearities are complicated, the derivation of the algebraic system becomes very cumbersome. Alternative methods have been proposed to overcome these shortcomings, such as the incremental harmonic balance method (IHBM) (Lau & Cheung 1981) but they are very demanding from a computational point of view. Recently, Cochelin & Vergez (2009) have proposed another strategy for applying the classical HBM with a large number of harmonics. The basic idea consists in recasting the original system 4.11 into a new system where non-linearities are at most quadratic polynomials by introducing as many new variables as needed. This leads to an augmented, but quadratic only, non-linear system for which the application of the HBM is quite straightforward. Furthermore, this quadratic framework makes it possible to use the so-called asymptotic numerical method (ANM) for the continuation of solutions. The ANM consists in computing power series expansions of solution branches and presents several advantages: it provides continuous solutions, the continuation is very robust, and the control of the step length is automatic and always optimal (Cochelin 1994). This method is detailed elsewhere (Kacem *et al.* 2011*b*), and is mostly the contribution of our partners from INSA de Lyon, which is why its application to our NL system will not be detailed here. Only the results of the HBM+ANM method will be compared to the analytical results.

4.2.1.2 Simplified analytical method

Assuming that the first mode should be the dominant mode of the system, only one mode is retained ($N_m = 1$). Eq. (4.11) becomes :

$$\begin{aligned} &\ddot{a}_1 + (500.564 + 12.3N_0)a_1 + (927 + 28N_0 + 151\alpha_1)\,{a_1}^3 \\ &+347\alpha_1{a_1}^5 + (1330.9 + 38.3N_0){a_1}^2 + 471\alpha_1{a_1}^4 \\ &+2.66c_1a_1\dot{a}_1 + 1.85c_1{a_1}^2\dot{a}_1 + c_1\dot{a}_1 + 2.66a_1\ddot{a}_1 \\ &+1.85{a_1}^2\ddot{a}_1 = -\frac{8}{3\pi}\alpha_2\left[V_{dc} + V_{ac}\cos(\Omega t)\right]^2 \end{aligned} \tag{4.12}$$

To analyze the equation of motion (4.12), it proves convenient to invoke perturbation techniques which work well with the assumptions of "small" excitation and damping, typically valid in MEMS resonators (see Nayfeh (1981) for a good introduction to perturbation techniques). The method of averaging was chosen for convenience and a standard constrained coordinate transformation is introduced by assuming a slowly time-varying amplitude:

$$\begin{cases} a_1 = A(t)\cos\left[\Omega t + \beta(t)\right] \\ \dot{a}_1 = -A(t)\Omega\sin\left[\Omega t + \beta(t)\right] \\ \ddot{a}_1 = -A(t)\Omega^2\cos\left[\Omega t + \beta(t)\right] \end{cases} \tag{4.13}$$

In addition, since near-resonant behavior is the principal operating regime of the proposed system, a detuning parameter σ is introduced, as given by:

$$\Omega = \omega_n + \varepsilon\sigma \tag{4.14}$$

We can then differentiate a_1 in 4.13, equate it with $\dot{a}_1$, substitute equations 4.13 in 4.12, and we obtain two equations for $\dot{A}$ and $\dot{\beta}$. As they are assumed to be slow-varying, we can equate them with their average over the period $\frac{2\pi}{\Omega}$ in the t-domain which gives in terms of amplitude and phase:

$$\dot{A} = -\frac{1}{2}\epsilon\xi_0 A - \frac{1}{8}\epsilon\xi_2 A^3 - \frac{1}{2}\epsilon\frac{\kappa}{\omega_n}\sin\beta + O(\varepsilon^2) \tag{4.15}$$

$$\begin{aligned} A\dot{\beta} = A\sigma\epsilon - \frac{3}{8}\epsilon\frac{\chi_3}{\omega_n}A^3 - \frac{5}{16}\epsilon\frac{\chi_5}{\omega_n}A^5 + \frac{7}{10}\epsilon\omega_n A^3 \\ + \frac{1}{2}\epsilon\frac{\kappa}{\omega_n}\cos\beta + O(\varepsilon^2) \end{aligned} \tag{4.16}$$

where

$$\omega_n = \sqrt{500.564 + 12.3N_0} \tag{4.17}$$

and the other parameters are $\xi_0 = c_1$, $\xi_2 = 1.85c_1$, $\chi_3 = 927 + 28N + 151\alpha_1$, $\chi_5 = 347\alpha_1$ and $\kappa = \frac{16}{3\pi}\alpha_2 V_{ac} V_{dc}$.

The steady-state motions occur when $\dot{A} = \dot{\beta} = 0$, which corresponds to the singular points of Eqs. (4.15) and (4.16). Thus, the frequency-response equation can be written in its implicit form as:

$$\left(\frac{3\chi_3}{4\omega_n}A^2 + \frac{5\chi_5}{8\omega_n}A^4 - \frac{7\omega_n}{5}A^2 - 2\sigma\right)^2 + \left(\xi_0 + \frac{\xi_2}{4}A^2\right)^2 = \left(\frac{\kappa}{A\omega_n}\right)^2 \tag{4.18}$$

The normalized displacement W_{max} with respect to the gap at the middle of the beam and the drive frequency Ω can be expressed in function of the phase β. Thus, the frequency response curve can be plotted parametrically.

This analytical model is a lightweight, easy-to-use and very efficient tool for MEMS designers. Although it is very simple, it is able to capture all the non-linear phenomena in the resonator dynamics (hardening and softening behaviors) and describe the competition between them.

4.2.1.3 Results

In a first step, the HBM+ANM method was validated over a shooting method, considered as a reference solution. Figure 4.2 shows this confrontation. Results are in very good agreement between the shooting and HBM+ANM methods, and the convergence of the latter is obtained with only 3 harmonics. A small difference between the curves for 1 mode and 2, 3 or 4 modes is noticeable. Nevertheless, it is less than 0.1% with respect to the peak frequency, which is negligible compared to the frequency shifts induced by the fabrication tolerances.

Figure 4.3 displays the confrontation of both models at a high non-linear regime for a polarization voltage V_{dc}=5V and a drive voltage V_{ac}=0.5V. In this configuration, the coupling between the modes is strongly amplified. Nevertheless, the error between the analytical model and the HBM+ANM model is still negligible, even with respect to the computational solution with 3 modes.

Several conclusions may be drawn from those results: first of all, the HBM+ANM study showed that convergence with the number of modes is very quickly obtained: there is a very slight difference with the use of 1 mode only and several, and a negligible difference with 2 or more modes

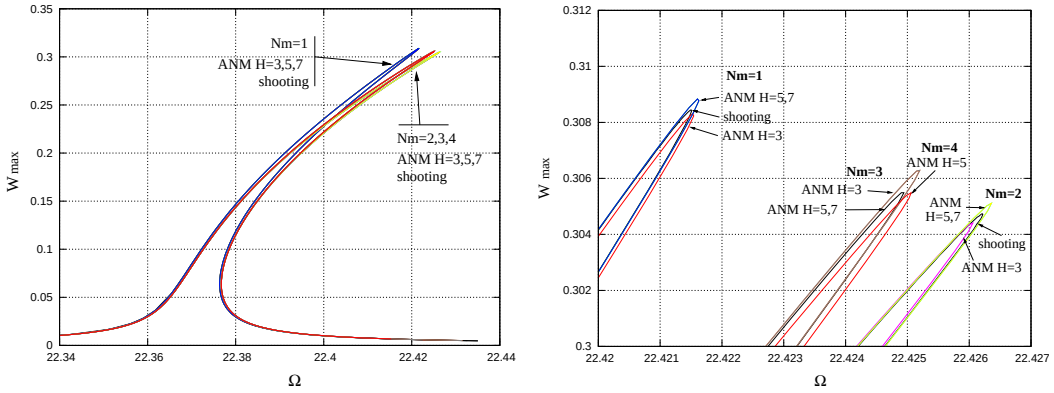

Fig. 4.2 – Confrontation Shooting/HBM+ANM on a strongly non-linear behavior (Beam $L = 400\mu m$, $b = 10\mu m$, $h = 10\mu m$, $g = 2\mu m$, $Q = 10000$, V_{dc}=9V, V_{ac}=0.9V). N_m is the number of modes used for the projection and H_m is the number of harmonics retained for the HBM

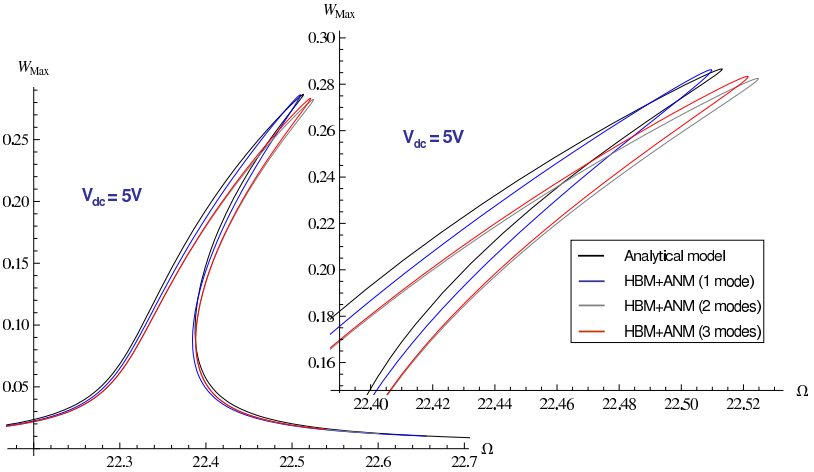

Fig. 4.3 – Confrontation HBM+ANM/Analytical model on a strongly non-linear behavior (Beam $L = 50\mu m$, $b = 1\mu m$, $h = 1\mu m$, $g = 0.4\mu m$, $Q = 1000$, V_{dc}=5V, V_{ac}=0.5V).

compared to other practical perturbations like fabrication uncertainties, temperature variation, pressure, etc... Although this is not a formal proof, it would tend to show relatively well that the loss of orthogonality induced by the multiplication by $(1 - w)^2$ is not an issue: solving equation 4.11 is legitimate and should be valid up to very large displacement, although this last point has not been demonstrated: our comparisons were made for ratios displacement over gap on the order of 30%.

As the number of modes does not make much difference in the numerical results, it was not surprising to see that the analytical model, retaining only 1 mode, gave very consistent results with the numerical results. This strong approximation has the clear advantage to yield a fast and accurate model, allowing analytical parametric investigations with respect to the phase of the resonator oscillation and the derivation of analytical expressions.

4.2.2 Duffing non-linearity cancellation and the mixed behaviour [2]

We applied the analytical model developed in the previous section to the resonators described section 2 and fabricated as the sensitive elements of accelerometers. This time, they are 2-port devices, see figure 4.4.

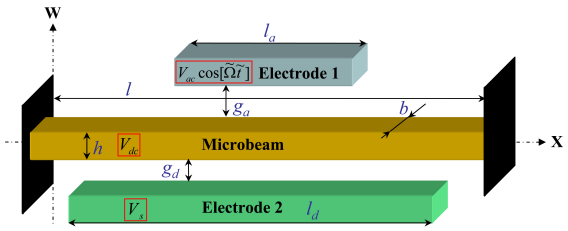

Fig. 4.4 – Schematic of the two-port device modelled. The top electrode is the actuation electrode, and the bottom is the detection electrode

The purpose of this simple experiment was the experimental validation of our model, beside the numerical validation in the previous section. The only difference was the expression of the electrostatic force density, as two electrodes are present from two opposite sides, and they cover only a part of the beam length. Because of this difference, the equation of motion was this time multiplied by $(g_a - w)^2(g_d - w)^2$ so that no approximation was needed on the displacement value relative to the gaps. On the other hand, this increases the level of non-linearity in the normalized equation of motion.

After proper normalization, the Galerkin procedure was applied with the undamped mode shapes as basis functions, and as seen in the previous section, only the first mode is retained for the projection. We obtain the following ODE:

$$\begin{aligned}
&\ddot{a}_1 + c\dot{a}_1 + {\omega_n}^2 a_1 + \mu_1 a_1 \ddot{a}_1 + \mu_2 {a_1}^2 \ddot{a}_1 + \mu_3 {a_1}^3 \ddot{a}_1 \\
&+\mu_4 {a_1}^4 \ddot{a}_1 + c\mu_1 a_1 \dot{a}_1 + c\mu_2 {a_1}^2 \dot{a}_1 + c\mu_3 {a_1}^3 \dot{a}_1 \\
&+c\mu_4 {a_1}^4 \dot{a}_1 + \chi_2 {a_1}^2 + \chi_3 {a_1}^3 + \chi_4 {a_1}^4 + \chi_5 {a_1}^5 \\
&+\chi_6 {a_1}^6 + \chi_7 {a_1}^7 + \nu + \zeta_0 \cos(\Omega t) \\
&+\zeta_1 a_1 \cos(\Omega t) + \zeta_2 {a_1}^2 \cos(\Omega t) \\
&+\zeta_3 \cos(2\Omega t) + \zeta_4 a_1 \cos(2\Omega t) \\
&+\zeta_5 {a_1}^2 \cos(2\Omega t) = 0
\end{aligned} \tag{4.19}$$

This ODE contains canonical terms like the Duffing term, the Van Der Pol damping as well as the Mathieu term. But it also contains non-linear terms up to the 7th order, as well as multifrequency parametric excitation terms, which is not so commonly encountered in the literature. Like before, the averaging technique is used for solving, and steady-state motions are investigated ($\dot{A} = \dot{\beta} = 0$). The solution can be written in its parametric form $\{A = K_1(\beta),\ \Omega = K_2(\beta)\}$ in function of the phase β as a set of 2 equations easy to introduce in Matlab or Mathematica. This ability actually makes the model very convenient for closed-form solutions and engineering purposes.

In particular, the model allows for easy computation of the onset of non-linearity, also called critical amplitude A_c. This is of prime interest for us: as previously mentioned, the maximum

[2] Details can be found in Kacem *et al.* (2009), Kacem & Hentz (2009)

drive amplitude is often set to this critical amplitude. It is the oscillation amplitude above which bistability occurs. At this transition, the frequency response exhibits a point of infinite slope in amplitude as well as in phase.

For the sake of simplicity, let's consider the case when electrostatic non-linearities can be neglected ($\frac{h}{g_d} \ll 1$). Then the parametric form of the frequency response is

$$\Omega = \frac{1}{8}\left(\frac{3\kappa^2\gamma_3}{\xi_0^2\omega_n^3}\sin^2\beta - 4\xi_0\cot\beta\right) + \omega_n \tag{4.20}$$

$$A = \frac{\kappa}{\xi_0\omega_n}\sin\beta \tag{4.21}$$

The critical amplitude is the amplitude for which the equation $\frac{\partial\Omega}{\partial\beta} = 0$, has a unique solution. This last trigonometric equation in $\sin 2\beta$ can be transformed into a fourth order polynomial equation, and this unique solution is $\beta_c = \frac{2\pi}{3}$, only under the condition of a particular critical drive κ_c. The critical amplitude at resonance, ie at the peak, is given by the amplitude obtained with this critical drive, at $\beta = \frac{\pi}{2}$ (see figure 4.5). Finally we find

$$A_c = 1.685\frac{h}{\sqrt{Q}} \tag{4.22}$$

Where Q is the quality factor of the considered mode. This expression is very similar to previous ones (Nayfeh & Mook 1979, Postma *et al.* 2005) and is a very good example of the model's advantages: this expression is simple and elegant, and it shows that the critical amplitude is only determined by the beam vibrating width h and the quality factor Q and does not depend on the beam length l. For example, the critical amplitude of a resonator with a quality factor of 10^4 and a width of $100nm$ is about $1.68nm$, which represents 0.84% of a $200nm$ gap...this confirms the importance of investigating these issues for a device performance.

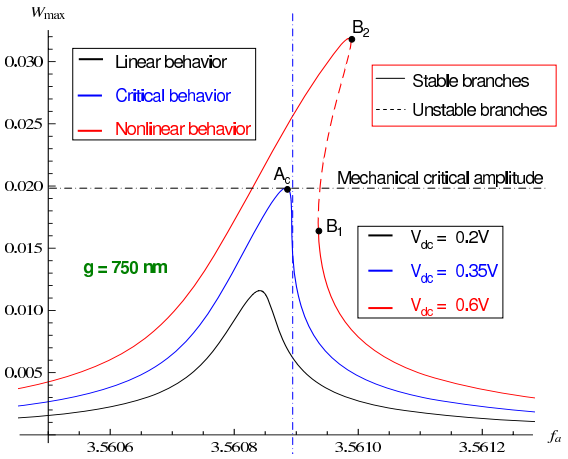

Fig. 4.5 – Forced frequency responses of a representative resonator. f_a is the dimensionless frequency and W_{max} is the displacement of the beam normalized by the gap g at its middle point $\frac{l}{2}$. A_c is the mechanical critical amplitude and $\{B_1, B_2\}$ are the two bifurcation points of a typical hardening behavior.

Figure 4.6 shows the simple LIA experimental setup. As explained in chapter 2, only the motional signal is obtained by background substraction. The objective was to obtain a model as predictive as possible, and no free parameter was kept. The fringing field coefficient was analytically

calculated (Nishiyama & Nakamura 1990) as well as numerically validated, the output capacitances were measured, the residual stress fitted from average frequency measurements. Only the quality factor was measured a posteriori.

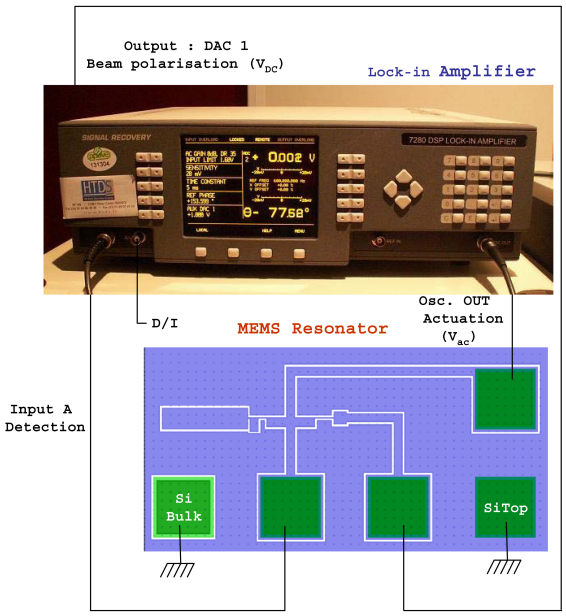

Fig. 4.6 – Experimental setup

Finally, figure 4.7 shows analytically predicted and experimentally measured frequency responses in a linear and non-linear case. Different peaks are shown, for different drive voltages, and more particularly different DC voltages (note the varying quality factor with DC voltage because of ohmic dissipation (Sazonova *et al.* 2004, Barois *et al.* 2012)). The agreement is excellent considering the absence of fitting parameters. The existing discrepancies are small relatively to slight changes or error in residual stress for example.

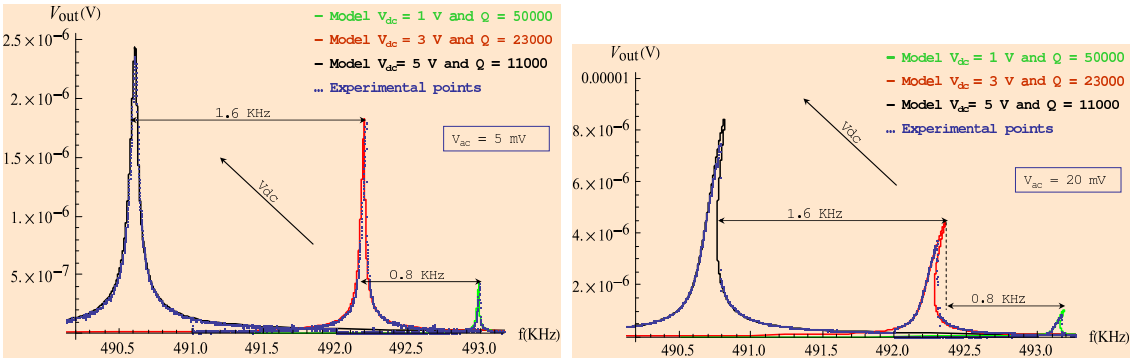

Fig. 4.7 – Frequency responses both analytically predicted and experimentally measured, in the linear case (left) as well as in the non-linear case (right)

These results gave us enough confidence in the prediction capability of our model. The procedure described for the computation of the critical amplitude can be performed without assumption as to which non-linearity dominates, in which case the DC voltage appears in the expression. Indeed, this voltage appears in the third order NL term and has a tuning effect on the NL. Figure 4.8 shows different behaviors the model displayed under some conditions for the same device, but with varying detection gaps and drive voltages. Firstly one should note that if represented on this graph,

the mechanical critical amplitude would be extremely low, around 15nm, that is a few percents of the gap. The usual softening as well as stiffening behaviors are also displayed, as well with a linear peak, well above the critical amplitude. This happens under certain conditions when mechanical and electrostatic non-linear terms (of order three) balance each other out. This is a straightforward dynamic range enhancement pursued by some groups in the past (Gui *et al.* 1998, Shao *et al.* 2008, Kozinsky *et al.* 2006). More interestingly, the model also showed a behavior we called "mixed behavior", because it is a mix of stiffening and softening behavior: indeed, it is a response with 4 bifurcation points and for one given drive frequency, up to five possible amplitudes. This is the result of the high order-terms present in the projected equation of motion 4.19: indeed, the frequency response must have multiple solutions in A, meaning the functions K_1 and K_2 must be polynomial of order at least 5 for this response to happen. In our case, equation 4.19 is of order 7.

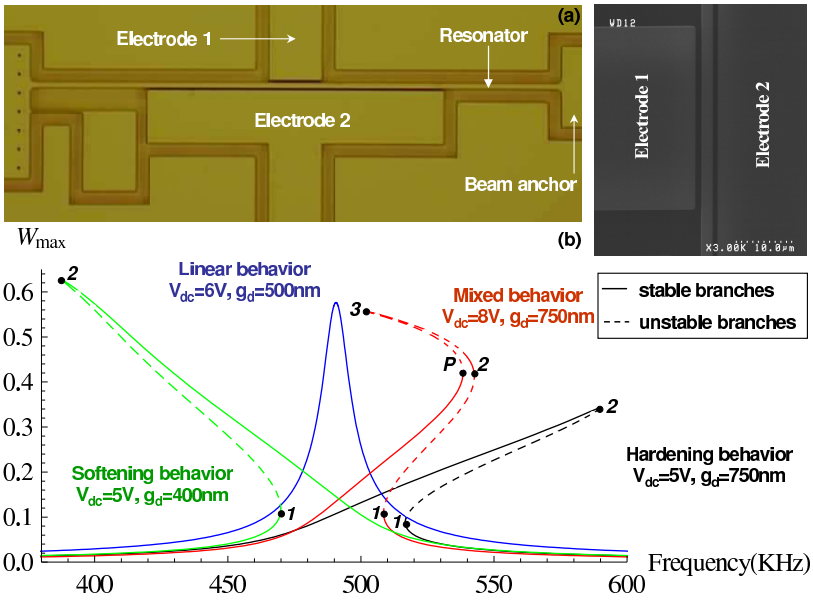

Fig. 4.8 – (a) Optical microscope image of a representative device. It is $200\mu m$ long, $4\mu m$ thick, $2\mu m$ wide, the actuation gap is $1\mu m$, and the detection gap $750nm$. (b) Predicted forced frequency responses for varying detection gaps and drive voltages. W_{max} is the displacement of the beam normalized by the gap g_d at its middle point $\frac{l}{2}$ and $\{1, 2, 3, P\}$ are the different bifurcation points. SEM image of the device is shown in the inset.

From this graph, the actual device with a $750nm$ detection gap seemed well suited to the appearance of a mixed behavior. Figure 4.9 shows an experimental frequency response obtained with $V_{ac} = 0.5V$ and $V_{dc} = 10V$, as well as the analytical fit. The beam undergoes very large displacement under these high voltages (up to 75% of the gap). The four amplitude jumps are the signature of a mixed behavior. This is most likely the first experimental evidence of the influence of the high-order NL terms.

Among the different bifurcation points present in the mixed behavior, the P point is interesting: it is located at relatively high amplitude as opposed to point 1 for example, and the closest stable branch is located even at higher amplitude (2-d_1). We indeed experimentally observed that P was highly unstable, the device going sometimes to pull-in, thus dangerous for the device operation. There may or may not be a stable branch below P out of resonance, depending on the relative position of the P point and point 1. Figure 4.10 shows the effect of increasing the DC voltage

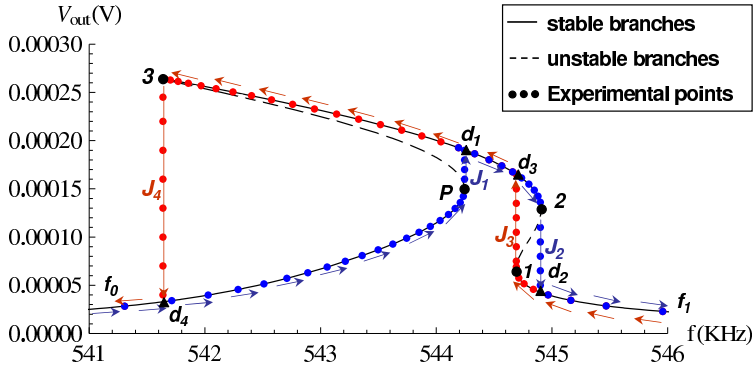

Fig. 4.9 – Analytical and experimental frequency curves showing a mixed behavior and the followed paths respectively in a sweep up frequency $f_0 - P - d_1 - 2 - d_2 - f_1$ and a sweep down frequency $f_1 - 1 - d_3 - 3 - d_4 - f_0$, with $V_{ac} = 0.5V$ and $V_{dc} = 10V$. $\{J_1, J_2, J_3, J_4\}$ are the four jumps cauterizing a typical mixed behavior of MEMS and NEMS resonators, $\{1, 2, 3, P\}$ are the different bifurcation points and $\{d_1, d_2, d_3, d_4\}$ are the destination points after jumps. The two branches $[3, P]$ and $[1, 2]$ in dashed lines are unstable.

on this bifurcation topology. Besides a negligible change in the static deflexion, this has several effects: i)the electrostatic spring softening induces a frequency shift, ii)the oscillation amplitude increases and iii)the quality factor decreases because of ohmic losses (Sazonova *et al.* 2004, Barois *et al.* 2012). Depending on the relative position of P and 1, the branch d_1-3 may or may not be stable, with a large variation in the possible stable oscillation amplitude.

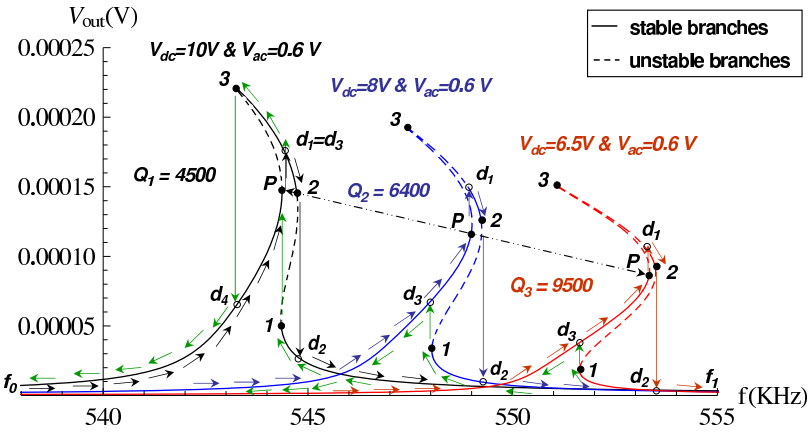

Fig. 4.10 – Analytical frequency responses showing mixed behaviors, the location of the different bifurcation points and the effect of the DC voltage on the stability of the different branches and the P point location.

An experimental demonstration of this effect is presented figure 4.11, where AC voltages are kept identical and responses are plotted against the ratio $\frac{V_{out}}{V_{DC}}$, proportional to the mechanical motion amplitude. Up and down oscillations around the P point confirm its instability. But as importantly, one should note the P point amplitude does not vary: indeed, its vertical location is set by the geometry of the device and is not changed by DC voltages (which tunes the NL terms though), the AC voltage or the quality factor. This is an undesirable feature as it is an upper bound to balancing out the NL terms of order 3 by DC voltage, and hence to the dynamic range of our resonators.

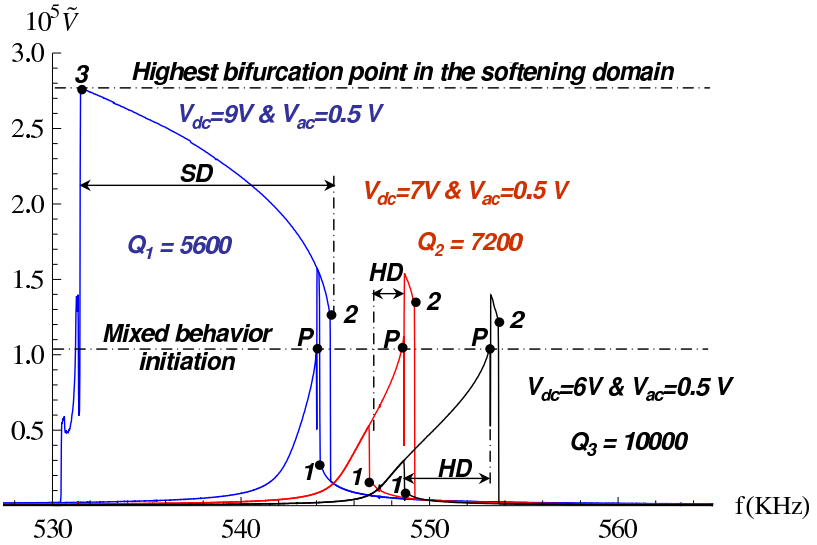

Fig. 4.11 – Resonance frequency responses showing mixed behaviors experimentally measured, the location of the bifurcation points, the effect of the DC voltage on the stability of the different branches and the P point vertical position. $\tilde{V} = \frac{V_{out}}{V_{DC}}$ is proportional to the mechanical amplitude. HD and SD are respectively the hardening and the softening domains. The point 3 is the highest bifurcation point in the softening domain.

4.2.3 Superharmonic and simultaneous resonance [3]

From the observation in the previous section that the dynamic range of our devices could be limited by an upper bound due to the bifurcation topology, or said differently by a highly unstable limit set only by the geometry of the device, we started investigating other types of dynamics than the primary resonance.

Non-linear oscillations are not sinusoidal, but rather are a sum of harmonics: one can expect additional peaks in the spectrum of a resonator dynamics. In general, they appear at driving frequencies which are integer fractions of the fundamental frequency. Those secondary resonances like parametric resonances of different orders are well-known in the vibration community, and have also been studied with MEMS resonators. A good pioneering example is the work of Turner *et al.* (1998), who used MEMS as a test bed to demonstrate higher-order parametric instability regions (up to 5), whereas one always had been limited to the first one with macroscopic objects. Many groups have investigated the interesting dynamics of parametric excitation in MEMS, for fundamental purposes with individual (Carr *et al.* 2000) or coupled devices (Lifshitz & Cross 2003), or noise squeezing since the 90s (Rugar & Grütter 1991).

Superharmonic and subharmonic resonances are another type of secondary resonances: let us consider a 1-dof NL resonator with the following equation of motion

$$\ddot{a} + \omega^2 a + \alpha_n a^n = F\cos\Omega t \tag{4.23}$$

then this resonator will display a resonant frequency response at ω when $\Omega = n\omega$ and when $\Omega = \frac{\omega}{n}$.

This type of resonance were already observed in MEMS not so long ago by a few studies, see for example Nayfeh & Younis (2005), and a few interesting dynamic features were observed. We also eventually investigated analytically superharmonic resonance: we start from the same projected

[3] Details can be found in Kacem *et al.* (2012*b*; 2011*a*)

equation of motion 4.19, neglecting all 2Ω terms. This time, we solve it with the multiple scale method (Nayfeh 1981) for reasons that will be explained later. We seek a first-order uniform solution of the form

$$a_1(t,\varepsilon) = a_{10}(T_0,T_1) + \varepsilon a_{11}(T_0,T_1) + \cdots \tag{4.24}$$

where ε is the small nondimensional bookkeeping parameter, $T_0 = t$ and $T_1 = \varepsilon^2 t$. Since the non linear response to a superharmonic resonance excitation of order two is analyzed, the nearness of Ω to $\frac{\omega_n}{2}$ is expressed by introducing the detuning parameter σ according to

$$2\Omega = \omega_n + \varepsilon\sigma \tag{4.25}$$

Substituting equation 4.24 into equation 4.19 and equating coefficients of like powers of ε yields

Order ε^0

$$\cos\left(\sigma T_1 + \frac{T_0\omega_n}{2}\right)\zeta_0 + \omega_n^2 a_{10} + {a_{10}}^{(2,0)} = 0 \tag{4.26}$$

Order ε^1

$$\begin{aligned}
&a_{10}^2\chi_2 + a_{10}^3\chi_3 + a_{10}^4\chi_4 + a_{10}^5\chi_5 + a_{10}^6\chi_6 + a_{10}^7\chi_7 \\
&+a_{10}c\mu_1{a_{10}}^{(1,0)} + a_{10}^2 c\mu_2 {a_{10}}^{(1,0)} + a_{10}^3 c\mu_3 {a_{10}}^{(1,0)} \\
&+\cos\left(\sigma T_1 + T_0\omega_n\right)\zeta_3 + \cos\left(\sigma T_1 + T_0\omega_n\right)a_{10}\zeta_4 \\
&+a_{10}^4 c\mu_4 {a_{10}}^{(1,0)} + a_{10}\mu_1{a_{10}}^{(2,0)} + a_{10}^2\mu_2{a_{10}}^{(2,0)} \\
&+a_{11}\omega_n^2 + \cos a_{10}^2\zeta_5\left(\sigma T_1 + T_0\omega_n\right) + c{a_{10}}^{(1,0)} \\
&+2{a_{10}}^{(1,1)} + a_{10}^3\mu_3{a_{10}}^{(2,0)} + a_{10}^4\mu_4{a_{10}}^{(2,0)} \\
&+{a_{11}}^{(2,0)} + \cos\left(\sigma T_1 + \frac{T_0\omega_n}{2}\right)a_{10}\zeta_1 \\
&+\cos\left(\sigma T_1 + \frac{T_0\omega_n}{2}\right)a_{10}^2\zeta_2 = 0
\end{aligned} \tag{4.27}$$

where $a_i^{(j,k)} = \dfrac{\partial^k}{T_1^k}\left(\dfrac{\partial^j}{T_0^j}\right)$.

The general solution of equation 4.26 can be written as

$$a_{01} = A\cos\left(\omega_n T_0 + \Phi\right) - \frac{4\zeta_0}{3\omega_n^2}\cos\left(\frac{\omega_n T_0}{2} + \sigma T_1\right) \tag{4.28}$$

Equation 4.28 is then substituted in equation 4.27 and the trigonometric functions are expanded. The elimination of the secular terms yields two first order non-linear ordinary-differential equations which describe the amplitude and phase modulation of the response and permit a stability analysis

$$\dot{A} = f_1(\varepsilon, A, \beta) + O(\varepsilon^2) \tag{4.29}$$

$$\dot{\beta} = f_2(\varepsilon, A, \beta) + O(\varepsilon^2) \tag{4.30}$$

where $\beta = 2\sigma T_1 - \Phi$. The steady-state motions occur when $\dot{A} = \dot{\beta} = 0$, which corresponds to the singular points of equations 4.29 and 4.30. Thus, the frequency-response equation can be written in its parametric form with respect to the phase β as a set of two equations

$$A = K_1(\beta) \tag{4.31}$$

$$\Omega = K_2(\beta) \tag{4.32}$$

Figure 4.12 shows different frequency responses obtained for a representative device, of similar dimensions as in the previous section. Remarkably, both stiffening and softening behaviors appear, depending on the ratio width over gap value, just like in the primary resonance case. Unlike the latter though, no mixed behavior with more than two bifurcation points could be found. Indeed, the superharmonic excitation filters out the effect of the fifth order nonlinear terms, and the only upper bound to third order non-linear term balance is pull-in occurrence. What is more, the critical amplitude for superharmonic resonance has the same expression as in the primary case. On the other hand, the superharmonic drive is not very efficient and unreasonable voltages should be used. To combine advantages of both techniques, we decided to investigate simultaneous primary and superharmonic resonances.

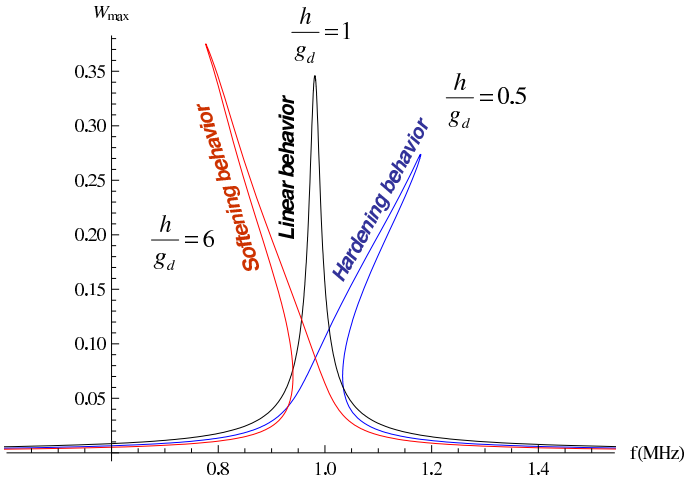

Fig. 4.12 – Superharmonic resonance: competition between stiffening and softening behaviors for different values of the ratio $\frac{h}{g_d}$ (W_{max} is the normalized displacement at the middle of the beam, h the width of the beam and g_d the detection gap)

For the sake of clarity, let's consider now an equation of motion containing all necessary ingredients for our demonstration, but kept as simple as possible: indeed, from the previous section, we know a Taylor expansion of the electrostatic driving term at the 5th order is enough to model the behavior of interest:

$$\ddot{x} + \mu\dot{x} + \omega_0 x + \alpha_2 x^2 + \alpha_3 x^3 + \alpha_5 x^5 = \zeta_1 \cos(\Omega) + \zeta_2 \cos(2\Omega) \tag{4.33}$$

Experimentally, simultaneous resonance comes at a very low cost: as the driving term is a superposition of a static voltage V_{dc} and a time varying voltage V_{ac}, the electrostatic force being proportional to the square of the voltage, two harmonics Ω and 2Ω of equation 4.33, with amplitudes ζ_1 and ζ_2 proportional to $V_{ac}V_{dc}$ and V_{ac}^2 respectively.

When Ω is tuned around the resonator normal frequency ω_0, the primary resonance at ω_0 is mainly actuated by the first harmonic Ω, the effect of the second harmonic being negligible. Experimentally, this is the "1f mode" of the lock-in amplifier, see section 2. When Ω is tuned around $\frac{\omega_0}{2}$, the resonant response at ω_0 is induced by both the first and the second harmonic 2Ω. More precisely, in this "2f mode" (where the output signal is at twice the input signal), the 2Ω harmonic mainly generates the primary resonance at ω_0, and the Ω harmonic actuates a superharmonic resonance at ω_0. The response at ω_0 is thus made of simultaneous primary and superharmonic resonances. The latter is generated via a "slow" excitation compared to the resonant frequency.

Basically, simultaneous resonance is experimentally obtained with the exact same 1f setup, but by switching the LIA to the "2f mode" and by going into the non-linear regime.

Analytically, we solve equation 4.33 (for fitting purposes, the full equation of motion 4.19 can also be solved in the same fashion). In order to investigate the fast (superharmonic) effects on a slow excitation, we use the multiple scales method which allows one to take into account the contribution of each dynamics in the resonator frequency response. Details of the computation can be found in Kacem *et al.* (2011*a*). At intermediate amplitude above the onset of bistability, DC voltage variations have no influence whatsoever on the response, showing no effect of the superharmonic resonance. Figure 4.13 shows the response for different values of V_{dc} (6, 8 and 10 V), and for a fixed $V_{ac} = 1\,V$, high enough to display a mixed behavior (the simulated device is which of figure 4.8). The amplitude of the P bifurcation point, called the onset of the mixed behavior is shown. As opposed to the actuation under primary resonance only, the P point amplitude is shifted up by the increase of the AC voltage, increasing only the superharmonic resonance relative to the primary resonance. This was exactly the type of mechanism we were looking for.

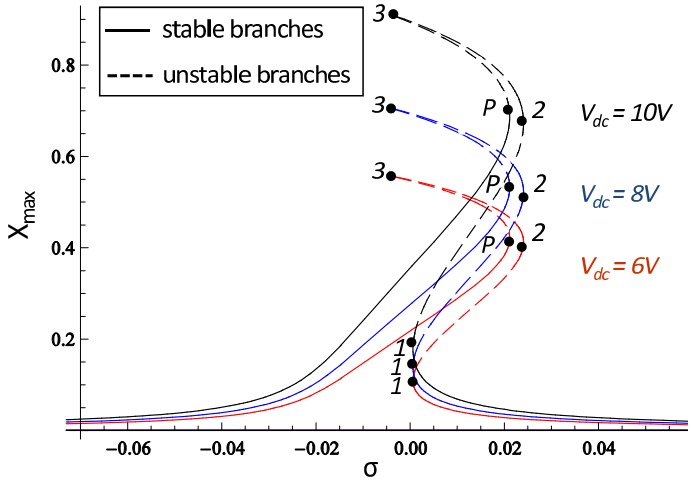

Fig. 4.13 – Analytical frequency responses showing mixed behaviors under simultaneous primary and superharmonic excitations; the location of the different bifurcation points and the effect of the DC voltage on the P point vertical position are shown. X_{max} is the displacement of the beam normalized by the gap g_d at its middle point. P point amplitude is the onset of the mixed behavior and point 3 is the highest bifurcation point in the softening domain.

The first experimental demonstration of simultaneous resonance in the literature is shown figure 4.14. It shows six nonlinear mixed behavior peaks, dashed and solid curves corresponding to "1f mode" and "2f mode" respectively. Again, the dimensionless voltage $\tilde{V} = \frac{V_{out}}{V_{dc}}$ is plotted, after background substraction in the 1f mode. Like in the primary resonance case only, the P point vertical location on the three 1d-mode peaks is unchanged with respect to the drive amplitude, proportional to $V_{ac}V_{dc}$. The onset of the mixed behavior (P point amplitude) is set only by the gap-to-width ratio of the device.

The three 2f-mode curves were obtained for $V_{ac} = 1V$, and a V_{dc} voltage increased from 6 to 10V. Since the Ω- and 2Ω-excitation amplitudes are proportional to $V_{ac}V_{dc}$ and V_{ac}^2 respectively, only the Ω-excitation amplitude was amplified. This increases significantly the quadratic nonlinearity, proportional to $V_{dc}^2 + \frac{1}{2}V_{ac}^2$, which in turn amplifies the superharmonic resonance. As a result, and due to the nonlinear interaction between the two harmonics, the slow dynamics transfers more

energy into the resonance at ω_0. The bifurcation topology is thus modified, and the onset of the mixed behavior in particular can be retarded: the slow Ω-excitation allows one to tune it; the simultaneous resonance shows the fast effect of a slow nonlinear resonance on the resonator bifurcation topology around the mixed behavior.

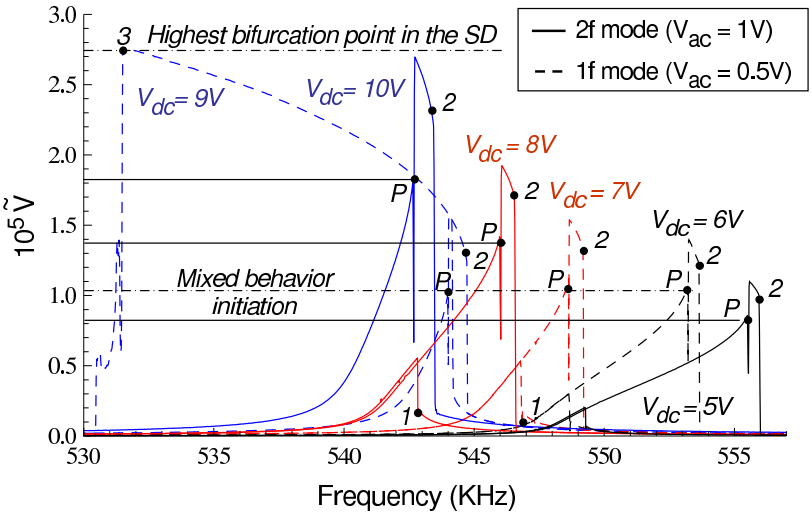

Fig. 4.14 – Frequency responses showing mixed behaviors measured under primary resonance as well as under simultaneous primary and superharmonic excitations, the location of the different bifurcation points and the effect of the DC voltage on the P point vertical position.

In summary, one can use a capacitive gate to cancel out the third order nonlinear terms and operate linearly beyond the Duffing critical amplitude, which is possible in a certain range of DC and AC voltage, and width over gap ratio. This new stability domain is small and is jeopardized by the onset of the mixed behavior which cannot be tuned with only primary resonance.

The use of simultaneous resonances (primary+superharmonic) has been shown here to overcome this limitation, by stabilizing the dynamic behavior of the resonator when operated at high drives. In fact, the effect of the high order nonlinearities can be retarded by an energy transfer between fast and slow dynamics which enlarges the stability domain beyond the onset of the mixed behavior. This stabilization technique has been patented (Hentz & Kacem 2010). One can expect nanoscale devices, with low SNRs and dynamic range to benefit greatly from this dynamics. A demonstration will be given in the next section.

4.3 Dynamic range enhancement

4.3.1 Non-linearities in cantilevers [4]

Cantilevers are commonly said to have a large dynamic range as opposed to doubly-clamped beams because non-linearities occur at very large displacement. This is mainly an experimental observation: little work has been done on the non-linear dynamics of macroscopic cantilevers, and even less in micro-cantilevers. One can cite recent investigations (Mahmoodi *et al.* 2008, Alhazza *et al.* 2008, Kumar *et al.* 2011).

The origin of non-linearities in a cantilever (or any non-extensional beam) is very different from

[4] Details can be found in Kacem *et al.* (2010)

the axial stretching in beams. It is mainly due to geometric effects (because of increasing curvature, the lever arm to the current cross-section decreases) appearing in the equation of motion as a non-linear stiffness and a non-linear inertia (see second and fifth terms in equation 4.34 respectively).

Figure 4.15 shows a schematic of the electrostatically actuated cantilever.

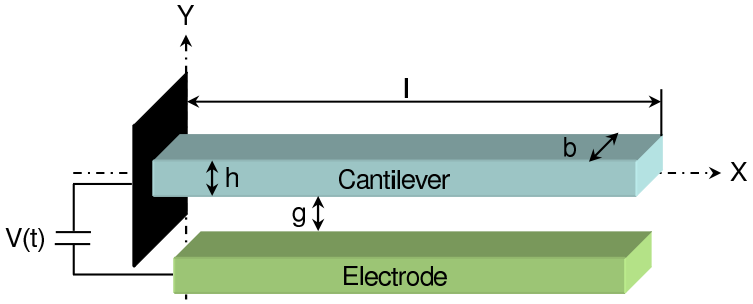

Fig. 4.15 – Schematic of the electrostatically actuated cantilever

The equation of motion of such a structure can be written (Crespo da Silva & Glynn 1978):

$$EI\left\{\tilde{w}'''' + \left[\tilde{w}'\left(\tilde{w}'\tilde{w}''\right)'\right]'\right\} + \rho bh\ddot{\tilde{w}} + \tilde{c}\dot{\tilde{w}} = -\frac{1}{2}\rho bh\left\{\tilde{w}'\int_l^s\left[\frac{\partial^2}{\partial\tilde{t}^2}\int_0^{s_1}(\tilde{w}')^2 ds_2\right]ds_1\right\}' + \frac{1}{2}\varepsilon\frac{C_n b\left[V_{dc}+V_{ac}\cos(\tilde{\Omega}\tilde{t})\right]^2}{(g-\tilde{w})^2} \quad (4.34)$$

where primes and dots denote respectively the partial differentiation with respect to the arclength s and to the time $\tilde{t}$; $\tilde{w}$ is the beam bending deflection in y. It is evident that such an equation will lead to more complex terms than a doubly-clamped beam.

Like before, after normalization, the Galerkin procedure is used with the first linear undamped mode shape, the second harmonic terms are neglected and the electrostatic driving term is Taylor-expanded at the fifth order so that the mixed behavior may be modelled; we obtain:

$$\begin{aligned}
&40.44\delta_1 a_1^3 + 0.39\frac{V_{ac}}{V_{dc}}\delta_3 + 0.78\frac{V_{dc}}{V_{ac}}\delta_3 - \frac{V_{ac}}{V_{dc}}\delta_3 a_1 - 2\frac{V_{dc}}{V_{ac}}\delta_3 a_1 \\
&+2.22\frac{V_{ac}}{V_{dc}}\delta_3 a_1^2 + 4.43\frac{V_{dc}}{V_{ac}}\delta_3 a_1^2 - 4.7\frac{V_{ac}}{V_{dc}}\delta_3 a_1^3 - 9.4\frac{V_{dc}}{V_{ac}}2\delta_3 a_1^3 \\
&+9.75\frac{V_{ac}}{V_{dc}}\delta_3 a_1^4 + 19.5\frac{V_{dc}}{V_{ac}}\delta_3 a_1^4 - 20\frac{V_{ac}}{V_{dc}}\delta_3 a_1^5 - 40\frac{V_{dc}}{V_{ac}}\delta_3 a_1^5 \\
&+a_1\lambda_1^2 + c\dot{a}_1 + 9.2\delta_2 a_1\dot{a}_1^2 + \ddot{a}_1 + 9.2a_1^2\delta_2\ddot{a}_1 \\
&+1.56\delta_3\cos(\Omega t) - 4\delta_3 a_1\cos(\Omega t) \\
&+9\delta_3 a_1^2\cos(\Omega t) - 19\delta_3 a_1^3\cos(\Omega t) \\
&+39\delta_3 a_1^4\cos(\Omega t) - 80\delta_3 a_1^5\cos(\Omega t) = 0
\end{aligned} \quad (4.35)$$

As usual, the canonical terms can be recognized (Duffing, Van Der Pol, Mathieu). The averaging method can be used to solve this equation, in the same fashion as already described, with the same standard constrained coordinate transformation and detuning parameter. Separating the resulting equations and averaging them over the period $\frac{2\pi}{\Omega}$ in the t-domain results in a system's averaged equations in terms of amplitude and phase. See (Kacem *et al.* 2010) for details.

The resulting model was validated over CMOS co-integrated nanocantilevers fabricated at CNM-IMB (CSIC) in Barcelona (Spain) and at EPFL in Lausanne (Switzerland), see figure 4.16 and Arcamone *et al.* (2008) for process details. The polysilicon devices are typically $12\mu m$ long, $300nm$ wide and $500nm$ thick, with frequencies around a few MHz. As an example, figure 4.17 shows the experimental motional admittance (hence after background substraction) versus frequency with varying DC voltages, along with the analytical fit. Only the quality factor was set a posteriori. Those responses are dominated by a softening behavior, which was expected in air, with low quality factors and large DC voltages.

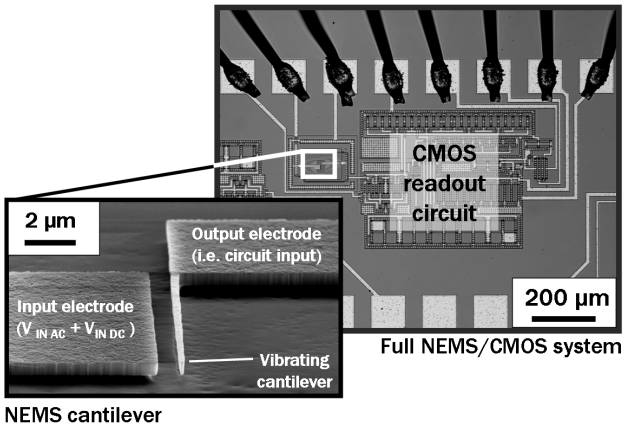

Fig. 4.16 – Optical picture of the [NEMS resonator / CMOS readout circuit] system. The scanning electron micrograph zooms the cantilever beam itself and its driving electrode.

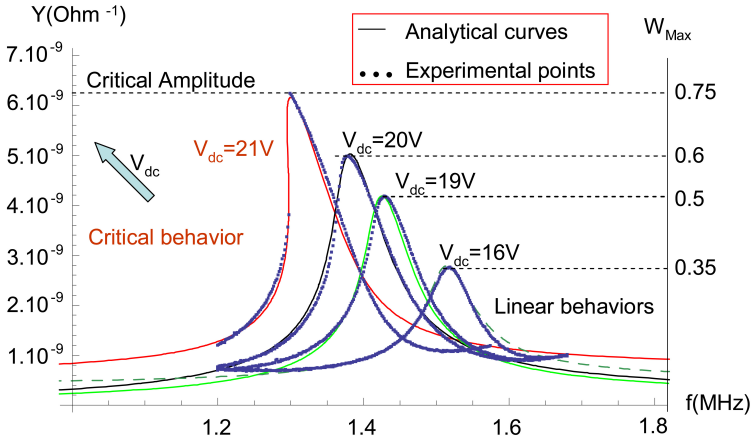

Fig. 4.17 – Analytical and measured motional admittance frequency curves (in air) of cantilever A. W_{max} is the beam displacement at its free end normalized by the gap.

Like in section 4.2.2, the model allows for the computation of closed-form solutions of the mechanical critical amplitude: again, using the same criterion for which the equation $\frac{\partial \Omega}{\partial \beta} = 0$ has a unique solution, and neglecting the electrostatic non-linearities, we find:

$$A_{cm} = 6.3\frac{L}{\sqrt{Q}} \tag{4.36}$$

This is most likely the first computation of a closed-form solution of the critical amplitude for cantilevers. Remarkably, and despite the complexity of the equation of motion, the expression is simple and depends only on the cantilever length and its quality factor, as opposed to the

width for a doubly-clamped beam (for which $Ac = 1.68\frac{h}{\sqrt{Q}}$). For a typical aspect ratio L/h of 10, cantilevers may display an onset of NL a few 10's times which of a doubly clamped beam, confirming experimental observations.

It is also possible thanks to the model to compute the critical amplitude in the opposite case, when electrostatic non-linearities dominate. We find

$$A_{ce} = 2 * 10^9 g^{\frac{5}{2}} \frac{h}{l\sqrt{Q}V_{dc}} \left(\frac{7.5 * 10^7 h^2}{l^4} - \frac{3.8 * 10^{-15} V_{dc}^2}{g^3 h} \right)^{\frac{1}{4}} \tag{4.37}$$

From both those closed-form expressions, assuming a constant quality factor and a low AC voltage it is easy to compute an optimal DC voltage so that both mechanical and electrostatic critical amplitudes are equal $A_{cm} = A_{ce}$: this is the condition under which third order NLs cancel each other out, yielding a linear response until higher order NLs show up.

Indeed, figure 4.18 shows analytical frequency responses obtained with a representative device ($l = 12.5\mu m$, $h = 300nm$, $b = 500nm$ and $V_{dc} = 50V_{ac}$. g and V_{ac} were varied). Fifth order NLs modify the behavior of a cantilever too for large displacements, and a mixed behavior may occur. This result, along with closed-form solution of an optimal DC voltage allowing the third order NLs cancellation opens up the possibility to stabilize the device dynamics up to a very large amplitude.

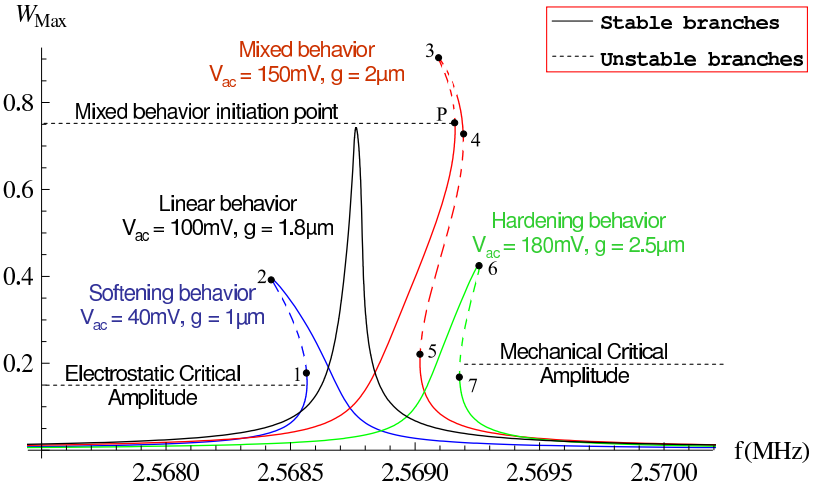

Fig. 4.18 – Analytical forced frequency responses for $Q = 10^4$ and several values of g and V_{ac}. W_{max} is the beam displacement at its free end normalized by the gap g, A_c is the critical amplitude above which bistability occurs, $\{1, 2, 3, 4, 5, 6, 7\}$ are the different bifurcation points and P is the third bifurcation point characterizing the initiation of the mixed behavior.

4.3.2 NEMS stabilization and dynamic range enhancement [5]

Among the different devices tested by the team and in this manuscript, the silicon piezoresistive device described section 3.2.3 (figure 4.19) displays the highest output signal amplitude, the highest SNR and SBR, and the best mass resolution. We naturally tried to improve still further this resolution by implementing the simultaneous resonance technique with this device. An additional motivation was the fact that, as previously mentioned, its frequency stability is several orders of magnitude lower than which expected from Robins' formula. It was interesting to check whether or not linearizing its output signal up to very large amplitudes would improve its frequency stability.

[5] Details can be found in Kacem *et al.* (2012*a*)

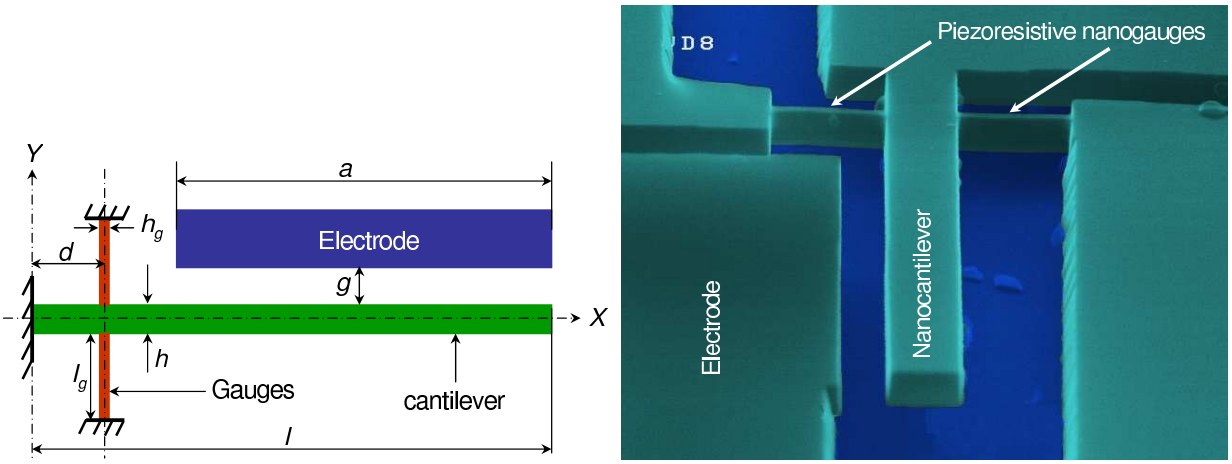

Fig. 4.19 – The Xbeam device and notations

Firstly we needed to operate in the regime where third order NLs would cancel out. Assuming the cantilever displacements are very small in the span between the anchor and the gauges, the overall dynamics is the same as an equivalent cantilever of length $l - d$. Replacing l by $l - d$ in the expression of the optimal DC voltage, we could compute the value of the latter. Then the device could be operated under simultaneous resonance thanks to a 2f down-mixing scheme as in section 3.2.3, but with an added DC voltage, see figure 4.20. The latter were evaluated around 0.5V (as all assumptions in its computation are not completely satisfied, some amount of trial and error is necessary).

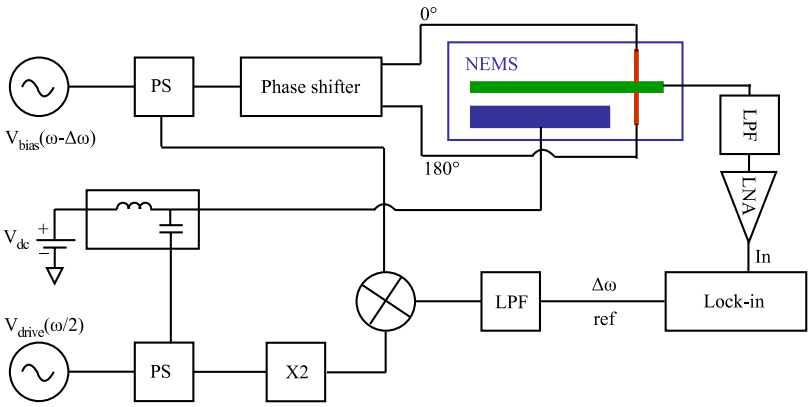

Fig. 4.20 – 2ω down-mixing scheme for simultaneous resonance (note the added DC voltage). PS, LPF are power splitter and Low-Pass Filter, respectively.

Figure 4.21 shows a frequency response obtained under simultaneous resonance with $V_{dc} = 0.5V$ and $V_{ac} = 2V$. The device is $5\mu m$ long, $300nm$ wide and $160nm$ thick, the gap is equal to $200nm$. Analytically, for this set of parameters the nonlinear electrostatic and mechanical stiffnesses are balanced and the cantilever oscillation amplitude is close to $200nm$ at its free end, barely touching the drive electrode without pull-in or observed damage. Remarkably, the frequency response is almost linear, with very little hysteresis, up to around 98% of the gap. The same device with the 1f scheme showed a highly unstable, multi-bifurcated behavior at oscillation amplitudes well below this value.

To make sure the displacement figure 4.21 is as high as analytically expected, the DC voltage

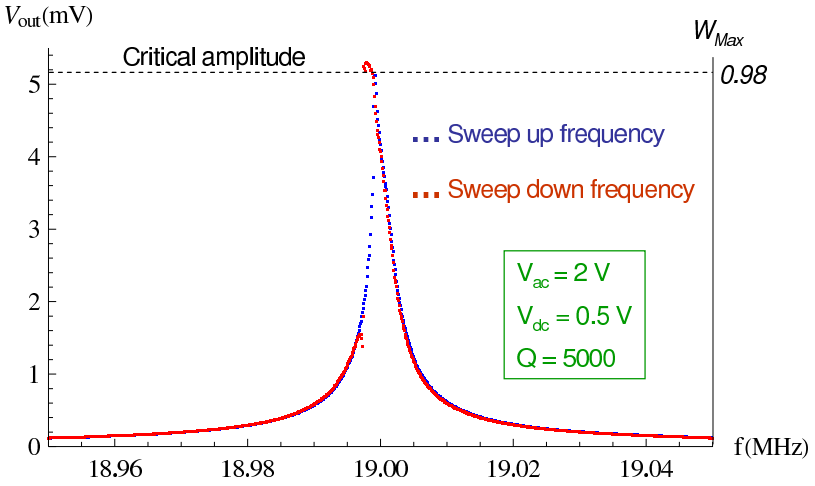

Fig. 4.21 – Slightly softening resonance frequency response measured using a 2ω down-mixing technique at the optimal DC voltage. The peak is close to the critical amplitude. W_{max} is the cantilever displacement at its free end normalized by the gap.

was increased up to 2V, see figure 4.22. There is a plateau in amplitude (not coming from the LIA sensitivity), confirming that the displacement is limited by the electrode nearby. Moreover, the change in operation regime moves away from the optimal DC and a softening behavior is seemingly obtained.

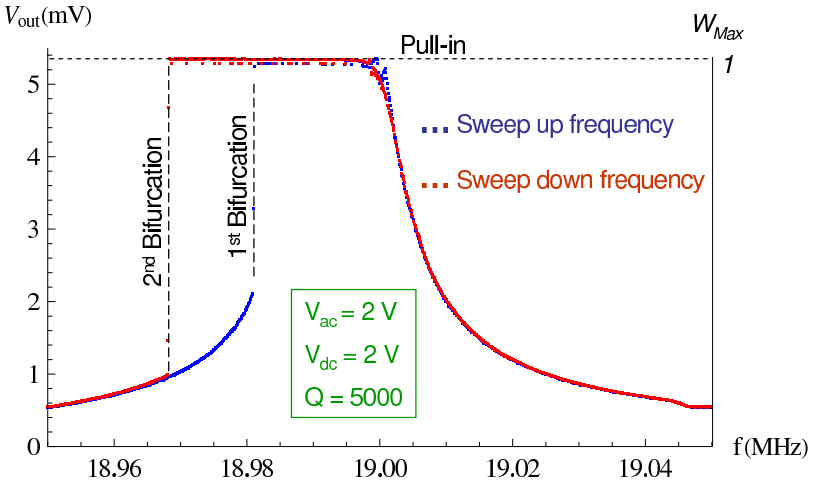

Fig. 4.22 – Softening frequency response measured using a 2ω down-mixing technique at $V_{dc} = 2V$. W_{max} is the cantilever displacement at its free end normalized by the gap.

4.4 Conclusion

This chapter explained the development of an analytical model based on perturbation techniques to study the rich dynamic behavior we observed experimentally. It includes with as few assumptions as possible all orders of mechanical and electrostatic non-linearities. It provided with a simple expression for the mechanical onset of NL, and showed the effect of high-order terms (> 3): they were experimentally observed, certainly for the first time in the literature. The cancellation of the usual non-linearities (third order) by balancing mechanical and electrostatic terms is possible only in

a narrow parameter window, limited by the onset of a mixed behavior induced by high-order terms (fifth order). This mixed behavior is highly unstable, and its onset is set by the device geometry with only primary resonance. We analytically as well as experimentally showed how simultaneous primary and superharmonic resonances could retard this onset and stabilize our Xbeam device with displacements up to the gap. This significantly increases the dynamic range and if the dominant noise is additive, will potentially improve our frequency stability by as much. This will be discussed in the next chapter.

Chapter 5

NEMS-Mass Spectrometry, mass resolution and device noise [1]

5.1 Introduction

The idea of performing Mass Spectrometry (MS) with NEMS originated in Pr. Michael Roukes group at Caltech some 12 years ago from the pioneering work on NEMS fabrication (Yang *et al.* 2001), NEMS dissipation (Mohanty *et al.* 2002, Cleland & Roukes 2002), NEMS electrical characterization (Ekinci *et al.* 2002) and finally the realization that NEMS mass resolution was exquisite, both theoretically (Ekinci *et al.* 2004*b*) and experimentally (Ekinci *et al.* 2004*a*), where a few ag mass resolution was demonstrated and individual molecule weighing was envisioned. Since then, several groups in the NEMS field consider NEMS-MS as one of the possible applications of their research (Jensen *et al.* 2008, Lassagne *et al.* 2008, Gil-santos *et al.* 2010, Atalaya *et al.* 2010, Jiang *et al.* 2011, Park *et al.* 2011, Chaste *et al.* 2012).

My contribution in the field started within the context of the LETI/Caltech Alliance in 2008/2009, firstly from the device point of view, in terms of mechanical structure, mass resolution and noise modelling, and later from the system architecture point of view. This work was performed at LETI along with PhD student Eric Sage, as well as at Caltech in Pr. Roukes group during my fellowship there as a visiting scientist in 2010/2011, along with Caltech PhD students Selim Hanay, Scott Kelber and staff member Akshay Naik. A number of my scientific interests nowadays are likely to have an application in NEMS-MS. Most of this work is still unpublished; I will only go briefly into the main results.

I will not go into much detail on MS and its applications, I will only recall the main features so that the stakes are well understood. Conventional MS principle of operation relies on the ionization of neutral analytes, and on measuring how the trajectories of the resulting ions respond in vacuum to various combinations of electric and magnetic fields. Four basic components are necessary (see figure 5.1): injection, (usually from the liquid phase into vacuum for biological applications, but it can be from the solid or gas phase as well), ionization source, mass analyzer (which sorts the analytes according to their mass-over-charge ratio) and ion detector. A mass spectrometer gives a *mass spectrum*, that is to say a graph showing the abundance of the analytes within the mixture to be analyzed versus their mass-to-charge ratio. Figure 5.2 shows the typical mass range and

[1] Details will be found in Hanay *et al.* (2012)

associated analytes processed by MS.

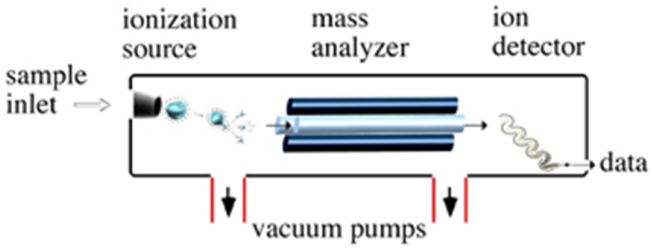

Fig. 5.1 – Conventional Mass Spectrometry basic components

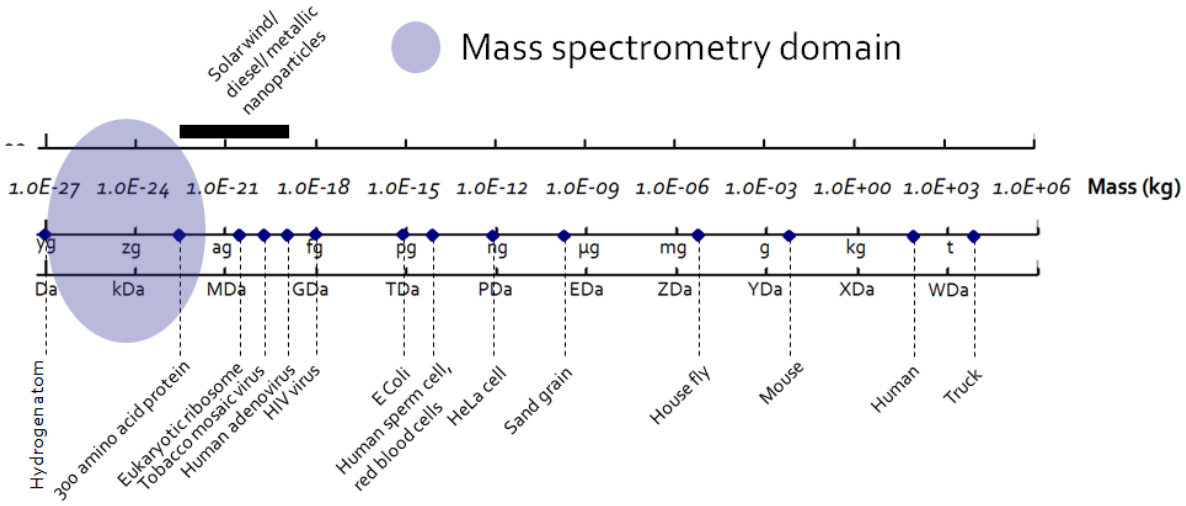

Fig. 5.2 – Conventional Mass Spectrometry mass range, orders of magnitude

The principle of NEMS-MS is straightforward: the idea is to directly weigh the analyte accreting onto the NEMS surface by measuring the induced frequency shift. After transferring the analyte from the liquid phase into vacuum, there is no need for ionization or mass sorting. Several attributes may potentially make this technology a real breakthrough: as opposed to conventional MS, it can be massively parallel thanks to VLSI fabrication techniques providing orders of magnitude improvement in speed; miniaturized and low-cost devices may emerge as opposed to several 100k\$ apparatus that fill a room; NEMS are sensitive to ionized and neutral species (commercial MS ionization yield is around 0.1 to 1%), providing orders of magnitude improvement in sensitivity; when the analyte mass is above its mass resolution, NEMS can access single-level measurement (while typical conventional MS ion detectors have a resolution of 100 to 100000 ions), which has tremendous biological significance.

The first NEMS-MS experimental demonstration is described in Naik *et al.* (2009), see figure 5.3. Commercial Electro Spray Ionization is used to ionize and transfer the analytes into vacuum through several pumping stages and hexapoles, used to guide the ions towards the NEMS. The latter is placed into an external magnet; transduction is magnetomotive. The NEMS device is a 428MHz SiC doubly-clamped beam displaying a 10kDa mass resolution at 40K. Figure 5.4 shows frequency vs time plots with individual events, signature of individual molecules landing on the

NEMS.

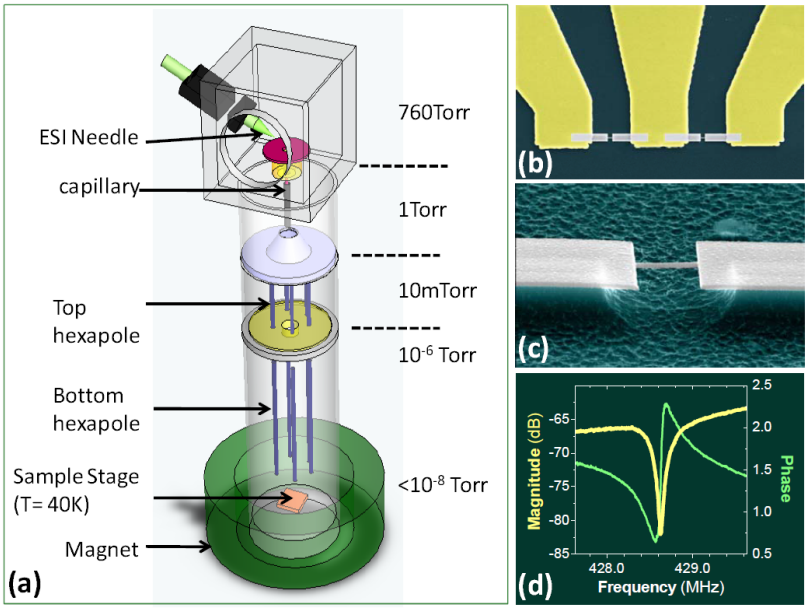

Fig. 5.3 – First-generation NEMS-MS system. (a) Simplified schematic of the experimental configuration (not to scale), showing the fluid-phase electrospray ionization and injection, the system's two-stage differential pumping, and its two-stage ion optics. (b, c) Progressively magnified scanning electron micrographs showing one of the doubly-clamped beam NEMS devices used in these experiments. It is embedded in a nanofabricated three-terminal UHF bridge circuit. (d) Magnitude and phase of the UHF NEMS resonator's response displaying a prominent fundamental-mode resonance near 428MHz ; from Naik *et al.* (2009).

Several problems arise there: first of all, the transduction demands an external magnet, which is an issue for integration and real-world devices. Secondly, frequency shifts amplitude depends on the analyte mass, but also on its position on the NEMS surface. This can be circumvented by a statistical approach of many events, but prevents real-time monitoring. Also, the event rate is low, and the analysis is long and demands much material in the first place.

5.2 NEMS-MS devices

Firstly, efficient, integrated transduction was needed with the best mass resolution as possible. Because of its easy VLSI fabrication, easy characterization and high performance, we chose to work with the silicon piezoresistive device named Xbeam described section 3.2.3. Another way to circumvent the position-dependent mass sensitivity is the use of simultaneous modes (Dohn *et al.* 2005; 2007, Schmid *et al.* 2010, Parkin & Hähner 2011). Indeed, we have:

$$\frac{\Delta f}{f_0} = -\frac{1}{\alpha M}\Delta m \Phi(a)^2 \Longleftrightarrow \alpha \delta f = \delta m \Phi(a)^2 \tag{5.1}$$

where f_0 denotes the natural resonant frequency of the device, M represents the device mass and $\Phi(a)$ denotes the resonance mode shape at the landing position a. Δm is the mass of the particle landing on the NEMS. α is a numerical factor depending on the normalization of the mode shapes. Writing the same equation for the two first modes, we can define a function G:

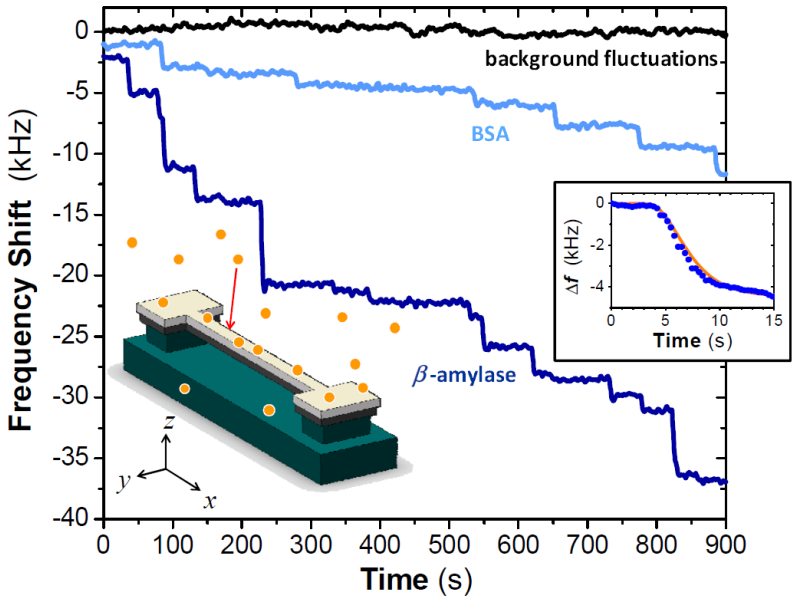

Fig. 5.4 – Real-time records of single-molecule adsorption events upon a NEMS mass sensor. This raw experimental data shows the distinctly-different, precipitous resonance frequency shifts of the NEMS during ESI-induced adsorption of bovine serum albumin (BSA, 66kDa) and β-amylase (200kDa). Each frequency jump downward is due to an individual protein adsorption event on the NEMS mass sensor. The height of the frequency jump is a convolved function of the mass of the protein adsorbed, and its position of adsorption upon the NEMS. Left Inset: Schematic illustrating single-molecule adsorption events on a NEMS resonator, and the coordinate system used to define its position-dependent mass responsivity ; from Naik *et al.* (2009).

$$G(a) = \frac{\Phi_1(a)^2}{\Phi_2(a)^2} = \frac{\alpha_1 \delta f_1}{\alpha_2 \delta f_2} \tag{5.2}$$

If G is invertible, the position a can be obtained in a straightforward fashion. It is unfortunately not the case, see figure 5.5. In the case of a cantilever, two modes are not enough to deduce with no ambiguity mass and position, three modes are then necessary (such conclusions have also been recently published by Stachiv *et al.* (2012)). Experimentally, this means a more complex measurement scheme, but also decreased performance: indeed, the ratios of the second and third mode frequencies over the first one are 6.3 and 17 respectively, more than an order of magnitude, meaning high frequency measurements and discrepancies in the frequency stability. For a doubly clamped beam, G is indeed invertible when limited to half of the beam: thanks to its symmetry, two modes are enough for mass and position determination, and their frequency ratio is roughly 2.75. On the other hand, a doubly clamped beam features a very low dynamic range compared to a cantilever, hence degraded mass resolution (see section 4.3.1). Figure 5.6 shows a device taking advantage of both high dynamic range and symmetry. The device is suspended via flexible beams, hence "relaxing" stress due to non-linear stretching, hence retarding the onset of NL. Those flexible suspensions do decrease the ratio gauge resistance variation over total resistance, but very slightly: both equivalent resistances are in parallel, and their own piezoresistance change due to stress cancel out.

Electrical characterization of this device was performed and 1f downmixing scheme was used, with two parallel and simultaneous channels for both modes, see figure 5.7. This remarkable point

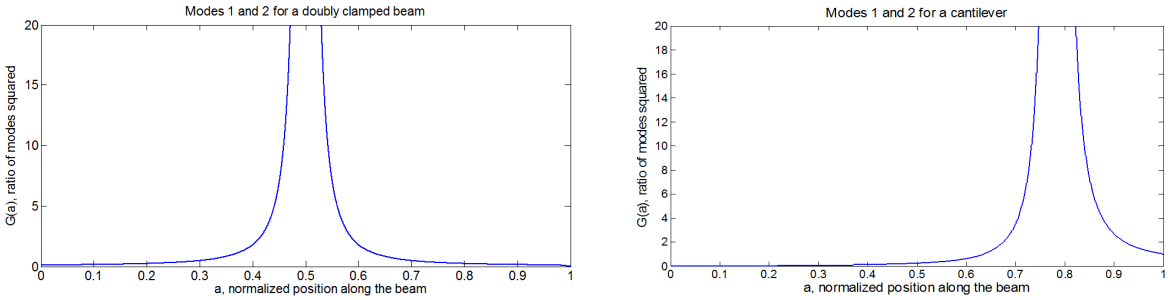

Fig. 5.5 – Function G for a doubly clamped beam (left) and a cantilever (right)

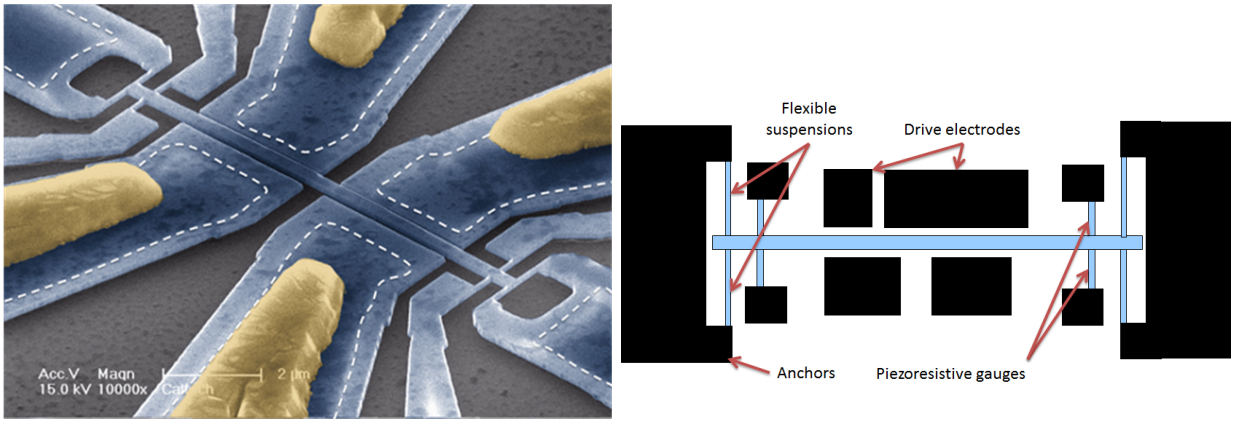

Fig. 5.6 – Device for real-time monitoring of mass and position of particles landing on the NEMS. Typical dimensions are $10\mu m$ long, $300nm$ wide, $160nm$ thick. Gauges and suspensions can be $80nm$ wide.

should be noted: two harmonics add-up in time in the drive circuit, as well as in the bias one. Consistently with Galerkin modal decomposition, the device real-time dynamics is complex, but is simply the sum of two modes in the frequency domain: these two modes mix with the two bias harmonics in the same gauges. The two output signals are recovered, under the condition that two distinct downmixing frequency $\Delta\omega_1$ and $\Delta\omega_2$ are used. Obtained Allan deviations are 8.10^{-8} for the first mode (around 25MHz), and 1.10^{-7} for the second one (around 65MHz), both with 500ms IT and at 80K. Those Allan deviations translate into a mass resolution below 50kDa (when the mass lands at the middle of the beam). This is the best mass resolution achieved in the literature by top-down devices. This device structure is patented (Hentz 2010).

As important as the absolute mass and landing position of the molecule, is the uncertainty of those values for each event. For the first time in the literature, this is the purpose of a probability computation, considering frequency jumps as statistical variables and using joint-probability density formalism (Hanay *et al.* 2012).

5.3 NEMS-MS experiments

The device of figure 5.6 was used for NEMS-MS experiments, in both the ESI setup described figure 5.3 and a new system, see figure 5.8. In the ESI setup, a large proportion of the analytes is lost during transfer by the hexapoles, firstly because the ionization yield is very low, and secondly because transmission of heavy (above the NEMS mass resolution) analytes is difficult. One motivation was

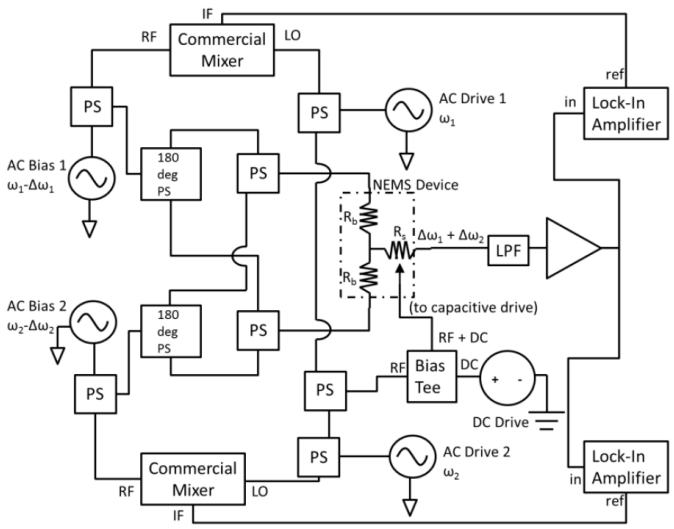

Fig. 5.7 – Diagram of the circuit used for the actuation and the readout of the NEMS device. In the diagram, PS = power splitter/combiner, 180 deg. PS = power splitter with 180 degree phase offset, LPF = low pass filter, in = input port to lock-in amplifier, ref= reference port of lock-in amplifier. The Bias and Drive oscillators are commercial frequency generators.

to switch to a system where the NEMS could be very close to the analyte beam source. This was done by a MALDI (Matrix Assisted Laser Desorbtion Ionization) technique, one of the conventional MS delivery systems (Tanaka 2003). The NEMS is enclosed in a UHV capable chamber equipped with a flow cryostat. The NEMS is placed on the end of the cryostat near the chamber center. Close to the NEMS is the MALDI sample plate on which the analyte solution is placed using the drip-dry method where droplets are applied and allowed to air dry. The MALDI process, in general, relies on a compound known as the matrix to efficiently absorb laser light. The matrix is mixed with the analyte sample so that when the matrix absorbs the laser light and it is ionized, it in turn induces ionization in the analyte and bursts into a plume promoting both to the gas phase. The sample plate was moved relative to the laser spot using a vacuum x-y stage. No ion optics were used, the NEMS collected positive and negative ions and neutrals from the MALDI plume.

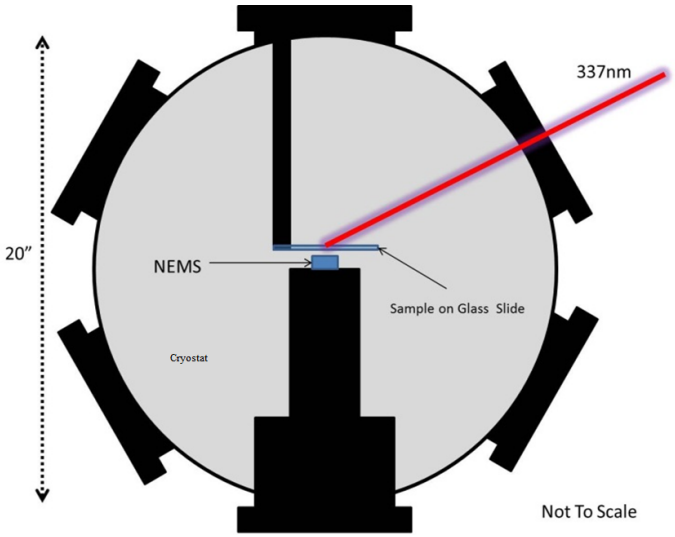

Fig. 5.8 – Diagram of the MALDI experimental system.

For the first time ever, the use of both those setups and the device above has successfully allowed for mass spectra of gold nanoparticles and proteins at the single level (Hanay *et al.* 2012). The event rate is still low though, as the ratio plume area over NEMS capture cross-section is of the order 10^{-8}.

5.4 Noise and mass resolution

One of the specifications of a Mass Spectrometer is the resolving power, that is the ratio measured mass over the mass resolution. Typical FT-ICR-MS may have a resolving power as high as 1.10^6 with masses up to a few 100Da, and may cost $1M\$$. On the other hand, Brücker MicroFlex MALDI-TOF (see figure 5.9) features a resolving power around a few 1.10^4 with masses up to a few 10kDa, and may cost a few $100k\$$. The former has then a resolution below 1mDa, whereas the latter has a mass resolution around 1Da. This question is critical to the application of NEMS-MS. As opposed to conventional MS, gravimetric detection has a constant resolution over its whole mass range: the higher the mass, the better the resolving power.

Fig. 5.9 – Bruker Microflex MALDI-MS

As previously mentioned, our device displays at best a mass resolution around a few 10kDa. The magnetomotive transducted SiC device in Naik *et al.* (2009) displays 10kDa. To find even better resolution, one has to go to bottom-up devices like Carbone Nanotubes (Chiu *et al.* 2008, Jensen *et al.* 2008, Lassagne *et al.* 2008) with a few 100Da or graphene nanoribbons (Chen *et al.* 2009), around 1kDa. Very recently, Chaste *et al.* (2012) claimed an unprecedented 1Da-resolution CNT, looking more like 10Da in practice. Even those impressive figures are very high compared to conventional MS resolutions. What is more, they are obtained with bottom-up devices like CNTs, which even if much progress has been made with their fabrication, may not be fabricated at large scales in VLSI foundries before a long time, and are not currently well suited for real-life devices,

mainly because of reliability issues. The question is then: what is the dominant noise in our devices and how can we decrease it?

Let's go back to section 3.2.3, describing the performance of the silicon piezoresistive device. Without driving the device, we achieved the readout of the thermomechanical noise, see figure 3.13. This noise amplitude in vacuum was evaluated around $S_v = 18nV.\sqrt{Hz}^{-1}$, for an output signal at resonance of about $S_{out} = 1mV$, and a typical quality factor of 10000. Recalling Robin's formula:

$$S_\omega(\omega) = \left(\frac{\omega_0}{2Q}\right)^2 \frac{S_v(\omega_0)}{P_0} \tag{5.3}$$

where P_0 is the carrier power and S_v the noise spectral density. We can then estimate $\sigma_a \simeq \frac{\delta f}{f} \simeq \frac{1}{2Q}\frac{S_v.\sqrt{BW}}{S_{out}}$, where σ_a is the Allan deviation. With 100ms IT, we could expect an Allan deviation around 1.10^{-9}. In general, this is also how the vast majority of studies in the literature assess their theoretical frequency stability, when they do not perform an experimental Allan deviation measurement. In our case, experimental Allan deviation was at best a few 1.10^{-7} at ambient temperature (see figure 3.14), more than 2 orders of magnitude worse.

This issue was thoroughly investigated in the last two years: First of all, the validity of Robins formula was investigated, and it turned out that it is fine for "low" (compared to output signal) white noise, which is the case with our device. The issue does not come from this formula, but from the numbers replaced in it: like everyone in the literature, we assumed our noise floor would remain the same with no drive (usually the thermomechanical noise) and at resonance. Figure 5.10 shows the experimental Allan deviation obtained with electrical downmixing and our 20MHz device as well as the expectation from Robins formula, for different drives. This was a measurement performed by Guillaume Jourdan, post-doc at LETI at the time, now staff member. At low drives, both experimental and expected frequency stabilities are almost identical, at least up to a certain IT. Both diverge at high drives though, and there is an apparent limit to the experimental frequency stability, no matter how much drive or bias voltages are used.

It is hard to get any insight into the spectrum of this noise from this measurement, done on relatively short ITs. Also, this is an electrical measurement, and there is no way to know if this noise limit originates from the electrostatic actuation (voltage fluctuations), from the piezoresistive detection (1/f noise in semiconductor gauges) or from the rack electronic. Figure 5.11 shows experimental Allan deviations versus drive power just like the previous measurement, but this time over very large time range and with optical interferometry detection. This experiment was conducted at Caltech thanks to the help of Rassul Karabalin and Akshay Naik, staff members, and the optical setup is the same as which described in Karabalin *et al.* (2009), Bargatin *et al.* (2012). The device used is a highly doped (around 5.10^{19}) silicon 20MHz, $5\mu m$ long, $300nm$ wide, $160nm$ thick Xbeam, in a vacuum chamber ($P < 1.10^{-4}$ Torr) at ambient temperature. The device in-plane motion, as well as the optical spot size reduced down to roughly $2\mu m$ explained a low detection gain: the dominant additive white noise is the photodetector noise, around $200\mu V.\sqrt{Hz}^{-1}$. The actuation is the electrostatic drive (but piezoshaker actuation tests has made no difference in the results whatsoever). Gauges are grounded. The photodetector signal is measured via a lock-in amplifier, and time acquisition of the phase fluctuations at resonance is performed by simultaneous recordings of X and Y from the LIA with a DAC card. Depending on the drive power, the LIA

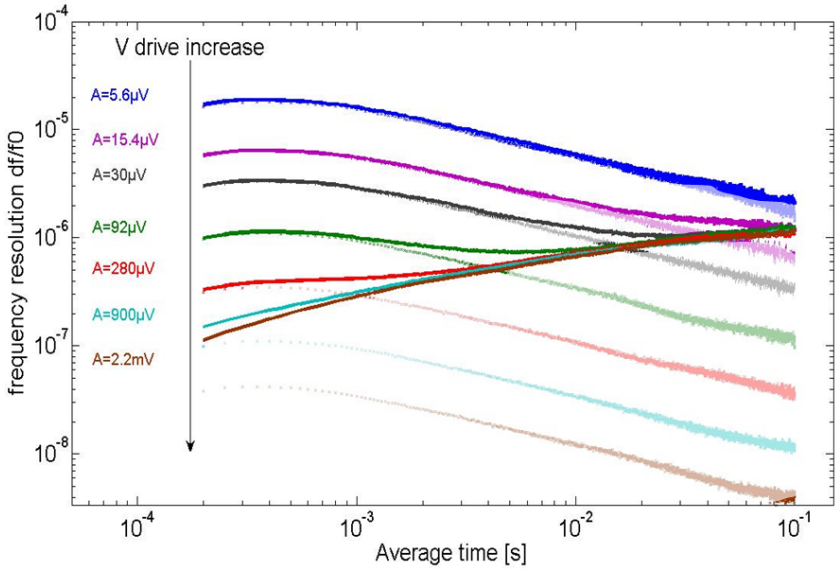

Fig. 5.10 – Open-loop Allan deviation obtained with a 20Mhz Xbeam, with electrical downmixing for various drive levels. The shadowed and dashed curves are the expectations from measured noise level and Robins formula

IT was set between 1ms to 5ms and the DAC sampling time was at least 5 times lower to satisfy Nyquist-Shannon criterion. A few million points were recorded for each drive power, during 2000 to 10000s. Drive powers were chosen in the largest range: the minimum is set by the background floor, and the maximum is set below (-3dB roughly) the onset of NL.

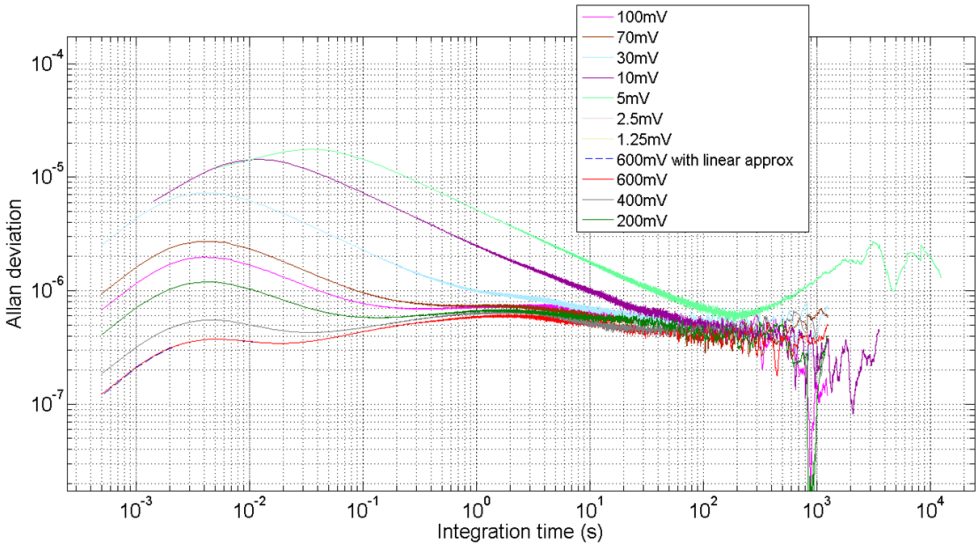

Fig. 5.11 – Open-loop Allan deviation obtained with optical interferometry ; phase acquisition is performed with a DAC card.

Each curve shows a first region where the Allan deviation increases slightly at low ITs (actually 4 times the LIA integration time). This is the visible effect of the LIA low-pass filter. Then the deviation reaches another regime, over a more or less extended IT range depending on the drive power: the Allan deviation is linear with a $-\frac{1}{2}$ power slope, which is very consistent with a dominant additive white noise. In this regime, numbers do correspond very well with the photodetector noise

and the signal at resonance for each drive power from Robins formula. This is true until all curves meet a limit curve which seems common to all drive powers. At high drive, the white noise regime is almost non-existent. The limit curve is not really flat as would have been the case for a dominant 1/f frequency noise, but displays an inversed parabola shape. As this limit does not depend on drive anymore, it may originate from an additional amplitude noise that increases linearly with signal, or directly from a fluctuation source; we would have:

$$S_\omega(\omega) = \left(\frac{\omega_0}{2Q}\right)^2 \frac{S_v(\omega_0)}{P_0} + S_{extra} \tag{5.4}$$

where S_{extra} is an extra frequency noise having the shape in the Allan deviation plot 5.11 of the red curve (at 600mV drive). The second main conclusion is that this frequency (or phase) noise does not originate from the detection or electronics noise, nor from actuation: this extra noise manifests itself in the mechanical domain.

One can think of many possible origins and questions about this extra noise:

- Temperature: the Temperature Coefficient of the Young's modulus of silicon (TCE) is of the order $-70ppm/K$, hence the TC of frequency of our device is around $-35ppm/K$. Our experimental Allan deviation translates into a few mK temperature stability, which seems very little from a general standpoint. But more than this absolute temperature variation, the time constant at which it should happen matters and first studies showed no time correlation between temperature fluctuations and this extra noise.
- crystal defect motion
- charge fluctuations
- gas-surface interactions
- is there a scale effect? The smaller the device, the bigger this extra noise relative to signal? This could be investigated with identical devices of different dimensions. Do bottom-up devices like those mentioned in introduction suffer from this extra noise?
- is there a material effect?
- ...

These observations and guesses are consistent with a very recent paper which investigated very similar issues with silicon nitride resonators and tentatively explained an observed extra phase noise with defect motion through a Two-Level State model, with relatively good success (Fong *et al.* 2012).

While those issues are critical to our device mass resolution, the conventional MS resolution and mass range seems out of reach of the current NEMS-MS.

5.5 Perspectives for NEMS-MS

Figure 5.12 is a graph showing the dynamic range of a mass measurement (a dynamic range of 1.10^4 for the weighing of a mass M means this measurement is performed with a precision equal to

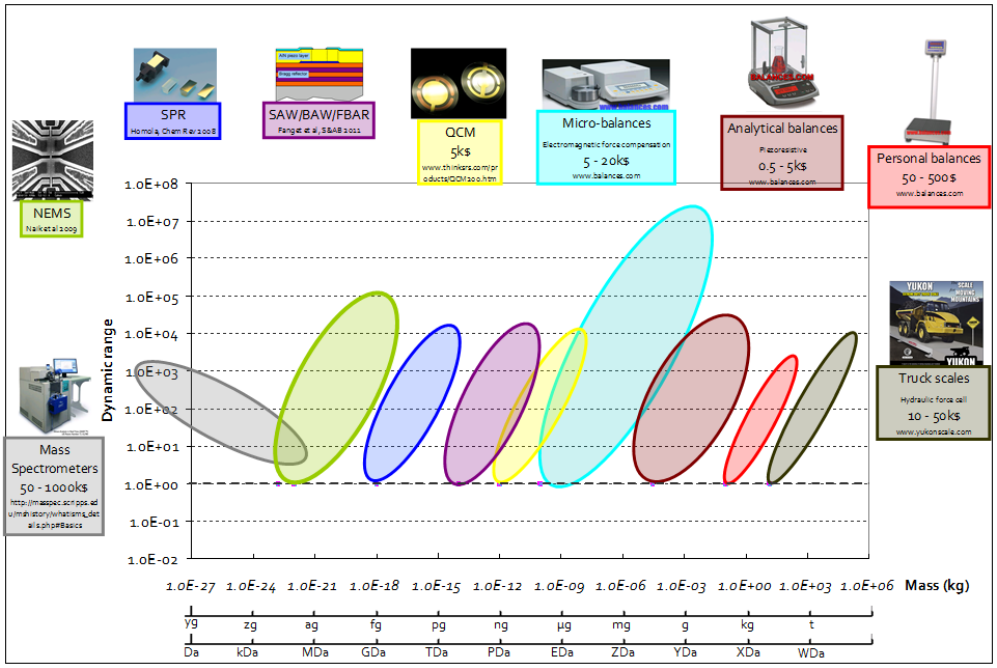

Fig. 5.12 – Measurement dynamic range versus objects mass range and associated commercial and non-commercial weighing technologies.

$M/1.10^4$) versus the measured mass, and the associated weighing technologies. There is an existing commercial technology for almost all mass range, except in the 100kDa-pg range. Above this range, gravimetric techniques display a constant LOD over their own mass range and their dynamic range improves with increasing mass. On the contrary, at the low end of the mass range, conventional MS deals with masses below 100kDa, but its dynamic range collapses at high masses, above a few 100kDa.

A main reason for this is that conventional MS detectors have low detection efficiency for slow-moving, heavy ions (Fraser 2002). Like Chang (2009) states: "This limitation is unfortunate because, beyond this mass range, a variety of bio-macromolecular assemblies and bio-nano-particles such as viruses, bacteria, cellular organelles and whole cells are undetectable by MS. Not only is the study of these entities of major fundamental interest, but also, the detection and characterization of intact biological systems has enormous biomedical significance. Despite a few limited successes, mass spectrometry has not yet been shown to be capable of reliable analysis of intact bioparticles. Compared to ensemble-averaging techniques used in conventional spectrometers, single-particle studies will permit much more accurate MS analyses for biological macromolecules than have previously been possible, as they would be devoid of any complexity arising from an ensemble approach. Such a detection technique is particularly useful for MS analysis of viruses and cells, both of which are genetically diverse agents. Measuring the masses of these bioparticles individually, obtaining their molar masses and mass distributions, and observing how these change with time and environment is expected to dramatically expand our understanding of these simple life forms." With our current mass resolution, NEMS-MS fills a technology void and combines the possibility of weighing those ultra high masses with excellent dynamic range, at the single-level and with intact bioparticles as ionization is not needed. Figure 5.13 shows how current NEMS-MS compares with some examples of experiments performed by researchers trying to circumvent the aforementioned high mass issue

with ion detection. For most of those results, NEMS-MS may provide orders of magnitude improvement in resolving power, as well as in sensitivity (amount of biological material needed to perform a spectrum measurement).

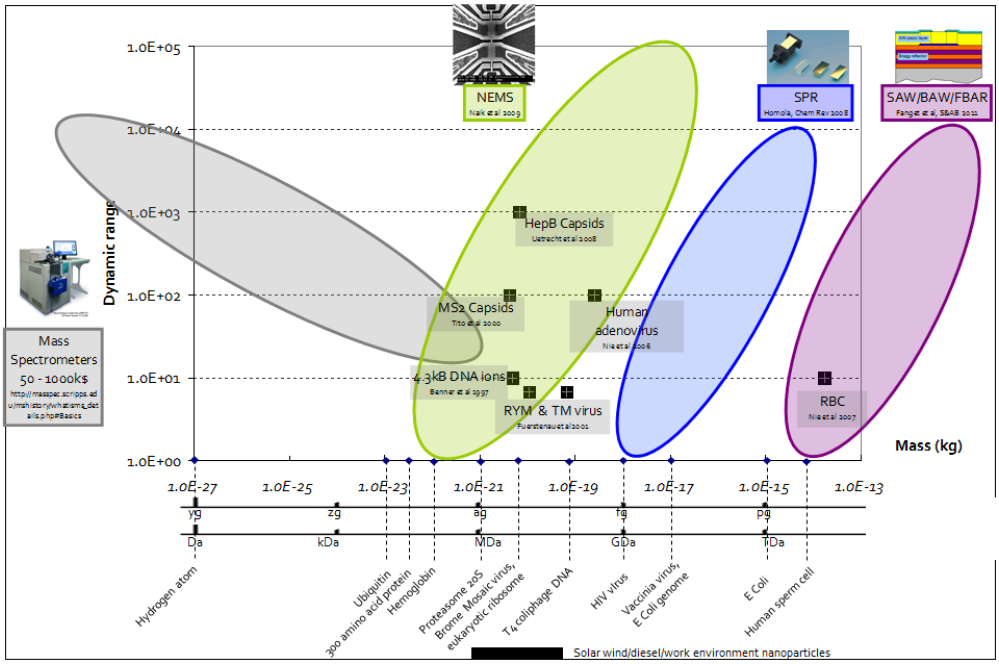

Fig. 5.13 – Measurement dynamic range versus objects mass range. A few results from research ion MS are shown.

Research perspectives

This manuscript has described some of the most representative activities. They all show a more or less present scientific background, with more or less applicative motivations. They are certainly representative of the course of my own research, but I think also of which of the sensor group within LETI, as well as more generally of the NEMS field. Anchored in the large background of research in nanoscience, the NEMS field has been trying to fulfill its promises and to evolve towards nanotechnology. The creation of the APIX Technology start-up is a good example of this evolution. Driven by a technology-push approach, the field gained in maturity and in scientific knowledge: let's make devices we have the means to fabricate, try to understand them, and eventually we will find something to do with them. Thanks to the acquired technological, material, experimental and scientific knowledge, we are probably more likely to accept a part of demand-pull research, which will undoubtedly provide us with as many fruitful scientific challenges.

Device noise Much effort was done on this topic, and there is still much to be understood. In particular, we should investigate the origin of the extra phase noise that limits the performance of our NEMS devices (see section 5). As already mentioned, this will demand surface physics experiments, investigation in materials from silicon to other crystalline materials but also monolayer materials like graphene. Devices with various surface-to-volume ratios should be investigated, extremely well controlled experiments with ultra-clean surfaces and surface treatments should be performed in UHV. Also, this mechanical domain noise should be investigated thanks to close-field optics techniques, as well as ultra-fast measurements to study properly its time-correlation with changes in environment parameters. In this context, a number of collaborations with other groups will have to be pursued.

Device arrays This is a topic which, I think, still remains in its infancy despite research efforts in several fields. Much remains to be done scientifically, and it may have an impact for various applications like gas sensing (Bargatin *et al.* 2012), biological sensing (Braun *et al.* 2009, Guillon *et al.* 2012) and of course NEMS-MS. Collective addressing for noise reduction and average-ensemble measurements still deserve some work: materials, frequency dispersion sources as well as adapted transduction should be studied. It is also the case of large arrays of individually-addressed devices to enhance by orders of magnitude the capture probability for extremely low concentration applications. This will demand studies for new and specific readout strategies and adapted transduction. For this, addressing will obviously be an issue and co-integration possibilities will have to be studied (Ollier *et al.* 2012).

For those arrays, piezoelectric transduction offers several great attributes: it allows for out of

plane motion as opposed to our silicon piezoresistive devices, and hence can lead to very compact layout ; it does not scale with dimensions and keeps its detection gain at the nanoscale, under the condition that parasitics are limited by a nearby amplification. Also, optomechanical transduction may be a good way to obtain ultra-large bandwidth for such arrays, and collaborations have also already started about this.

Alternative sensing methods Studying NEMS non-linear dynamics was an excuse to make different research communities meet. Several collaborations started from there, in France and abroad. We need to investigate alternative sensing techniques in order to circumvent potential limits of the usual frequential detection. A PhD started a couple years ago at INSA de Lyon/Ecole Centrale de Lyon about non-linear dynamics of NEMS. Will be investigated the possibility to use abrupt changes in the bifurcation topology to sense perturbations on the device.

If we are to use arrays of devices, we are not limited by individual device modes: devices can be coupled to each other, and collective patterns can be created within the array. This rich dynamics should be investigated for sensing purposes. This is a starting collaboration with Pr. Lifshitz group in Tel Aviv University (Kenig *et al.* 2009).

System integration and applications System integration, that is putting in place bricks already developed and make a system out of it is something that is usually seen as an engineering activity. But past experience has shown fruitful scientific challenges can be met with integration at the border of different expertise. These expertise and the associated bricks can largely benefit from this confrontation, and integration can happen relatively early in the scientific process ; it does not mean it deals with more applied motivations. This is one more sign of what was mentioned in the introduction: a shift from technology-push approach to some amount of demand-pull approach, thanks to the maturity of the NEMS field. More specifically and as is evident throughout this manuscript, a shift from a device-based approach to a system-based approach, where the device is but a small part of a whole.

In terms of applications, NEMS-MS is a good example: its development has already led to starting collaborations in various fields, including Caltech, INSERM, the Direction des Sciences de la Matière of CEA, Clinatec, Paris VI ; beside device arrays, we need to work on delivery systems taking advantage of no or very little -and soft- ionization with concentrated particle beams. It is also probably representative of the future of sensing: inertial sensing may show only incremental advances, whereas breakthrough may come from the biological, environment monitoring, biomedical or health fields: monitoring of airborne particle contamination, water contamination, biomolecule characterization tools for Point-of-Care diagnostic, cell culture arrays; robotics will also need smart sensors to anticipate the needs of disabled persons. Those are but examples of demand-pull research applications which are likely to provide us with hard challenges and which we could address as a payback for the amount of public money spent in nanoscale research...

Annex

The resonator

Notations

Every mechanical structure has its own eigenmodes ensemble. In the linear world, when actuated by one monofrequency harmonic close to one of these eigen frequencies ω_0, its behavior is equivalent to a linear, second order damped oscillator, satisfying equation 5.5.

$$m_{eff}\ddot{x} + c_{eff}\dot{x} + k_{eff}x = f_r \tag{5.5}$$

or equivalently

$$\ddot{x} + \frac{\omega_0}{Q}\dot{x} + \omega_0^2 x = \gamma \tag{5.6}$$

The frequency response of such a system is then characterized by a Lorentzian peak at $\omega_n = \sqrt{\frac{k_{eff}}{m_{eff}}}$, with a width depending on the quality factor Q. The associated transfer function is

$$\mathcal{H}_r(i\omega) = \frac{X(i\omega)}{F_r(i\omega)} = \frac{1}{m_{eff}} \frac{1}{\left(\omega_0^2 - \omega^2 + i\omega_0\omega/Q\right)} \tag{5.7}$$

If any external perturbation causes the effective stiffness k_{eff} or the effective mass m_{eff}, the resonance frequency shifts. If this variation law is known and if this shift can be measured, a sensor is born. This variation law is called the sensitivity and is an important specification of the sensor.

Besides sensitivity, another important specification is the limit of detection which is given by the amount of noise in the system: the lod will be given by the smallest change in frequency that can be measured. What we are interested in in particular is then the frequency noise.

Noise considerations

Dissipation sources

Systems that dissipate energy are necessarily sources of noise. Each energy dissipation source in a resonator may be characterized by its own quality factor Q_i, and the global quality factor is $Q = \left(\sum_i \frac{1}{Q_i}\right)^{-1}$. Dissipation sources can be intrinsic or extrinsic. Examples of intrinsic dissipation are phonon-phonon (including the well-known thermoelastic dissipation in the continuum limit) or electron-phonon interactions, two-level system effects, surface effects. Much literature exists on those issues, many analytical expressions exist ; we will neglect them in our efforts to assess the noise limitations in our devices (Ekinci & Roukes 2005, Jensen *et al.* 2006).

Extrinsic dissipation sources are friction with a fluid, squeeze-film damping, clamping losses. Again, a number of analytical expressions exist out there. This said, there has been little success as to predict the global quality factor (except maybe in air, where dominant viscous dissipation are easily computed) in nanomechanical systems. More important for us is the noise induced by those dissipation sources, and the total noise.

Noise sources

At each stage of the system (or at each transfer function in a block diagram), there may be a noise source, expressed by its spectral density, function of the frequency. A nice review of noise processes can be found in Cleland & Roukes (2002) ; they include temperature fluctuation noise, adsorbtion/desorbtion noise, which consistently with their results will be neglected in the following. I will detail only those of importance in our experimental conditions.

Thermomechanical noise This is a white noise in force applied to the resonator, of spectral density given by:

$$\mathcal{S}_{th}^{f}(\omega) = \frac{4k_bTm_{eff}\omega_0}{Q} \text{ , expressed in } N^2.Hz^{-1} \tag{5.8}$$

Given the transfer function of the resonator $\mathcal{H}_r(\omega)$, this gives the displacement noise spectral density around the resonance

$$\mathcal{S}_{th}^{X}(\omega) = |\mathcal{H}_r(\omega_0)|^2\mathcal{S}_{th}^{f}(\omega) = \frac{4k_bTQ}{m_{eff}\omega_0^3} \text{ , expressed in } m^2.Hz^{-1} \tag{5.9}$$

Johnson noise This well-known (white) noise is the electronic noise generated by the thermal agitation of the charge carriers (usually the electrons) inside an electrical conductor at equilibrium, of resistance R. Its expression is

$$\mathcal{S}_{j}^{V}(\omega) = 4k_bTR \text{ , expressed in } V^2.Hz^{-1} \tag{5.10}$$

Electronics noise The noise that has to be considered is the noise of the first amplification stage. It is a specification of the commercial apparatus (lock-in amplifier, low-noise amplifier...) given by the manufacturer. It is usually a white noise over a large bandwidth $\mathcal{S}_{elec}$.

Once expressed at the same node and in the same physical domain (example : in mechanical displacement, referred at the output of the resonator), these spectral noise densities sum up to give the total noise density $\mathcal{S}_{tot} = \mathcal{S}_{th} + \mathcal{S}_{j} + \mathcal{S}_{elec}$. Nevertheless, the latter still is an amplitude noise, while we need the frequency noise.

Frequency noise computation

The minimum detectable frequency shift is given by the fluctuation of this frequency, ie its noise. The output signal (in any physical domain) at any point of the loop may be written as:

$$V(t) = (V_0 + \delta V(t))\cos(\omega_0 t + \delta\phi(t)) \tag{5.11}$$

In the case of additive noises, that is to say random white processes added to the useful signal (as opposed to multiplicative noise like Flicker noise, up- or downconverted noise from some nonlinearity), the noise power is equally partitioned between phase noise $\mathcal{S}_{\delta\phi}$ and normalized amplitude noise $\frac{\mathcal{S}_{\delta V}}{V_0^2}$ (Rubiola 2009): $\mathcal{S}_{\delta\phi} = \frac{\mathcal{S}_{\delta V}}{V_0^2} = \frac{\mathcal{S}_{tot}}{V_0^2}$.

Linearizing $arg(\mathcal{H}_r)$ in equation 5.7 close to the resonance, the frequency noise density is written:

$$\mathcal{S}_\omega(\omega) = \left(\frac{\omega_0}{2Q}\right)^2 \mathcal{S}_{\delta\phi} = \left(\frac{\omega_0}{2Q}\right)^2 \frac{\mathcal{S}_{tot}}{V_0^2} = \left(\frac{\omega_0}{2Q}\right)^2 \frac{1}{SNR} \tag{5.12}$$

where SNR stands for Signal to Noise Ratio.

This is a representation of the frequency noise in the frequency domain. To compute the resolution of a sensor, we need the fluctuation of the frequency over time. This is given by the Parseval theorem:

$$\sigma_\omega = \int_{\omega_0-\Delta\omega/2}^{\omega_0+\Delta\omega/2} \mathcal{S}_\omega(\omega) d\omega \tag{5.13}$$

where σ_ω is the variance of the pulsation when the noise is integrated in a bandwidth $\Delta\omega$ around ω_0.

Equation 5.12 is also called the Robins formula (Robins 1984). It shows that a low resolution sensor is obtained thanks to a resonator displaying a low noise, large signal output ; hence the need for a high gain readout transduction.

Experimental noise characterization

Noise can be measured and expressed in the frequency domain and in the time domain. In the first one, the density of the phase noise at an offset of $\Delta\omega$ from the carrier at ω_0 is directly measured. In the second one, an estimator of the phase- or frequency - or normalized frequency variance σ is measured versus a sampling or integration time ; there are many estimators of this variance, the most common is the Allan deviation.

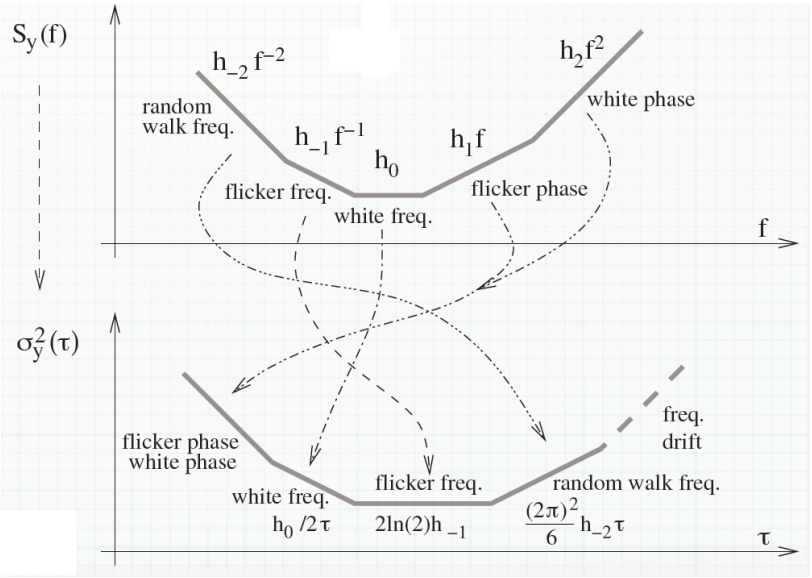

Fig. 5.14 – Power laws for spectra and Allan deviation, from Rubiola (2009)

From a very general point of view, the frequential domain is used for high frequency (or very short term) noise, whereas Allan deviation is more used for low frequency (or long integration times, up until "drifts"). The Allan deviation shown figure 5.14 has a typical parabolic shape. The most commonly encountered type of noise in our systems is amplitude white noise from an external source (thermomechanical, electronic noise), ie an additive noise. The formalism used above for frequency noise computation only takes into account white noises, which is ok to show big trends for scaling like in the core of the manuscript. Additive white noise translate into white frequency noise in feedback loop and it would show in the Allan deviation plot by a $-\frac{1}{2}$ slope. In practice though, there are lower- and higher order terms in the graph, showing the presence of multiplicative noises and drift effects.

True variance

Any quadratic quantity can have an energetic interpretation, therefore one calls the following quantity

$$P(t) = |f(t)|^2 \tag{5.14}$$

the instantaneous random power of the signal f(t). The instantaneous average power is the ensemble average of $|f(t)|^2$, that is by definition its variance σ^2 in the case of a centered signal. (In the case of an ergodic, stationnary and centered signal, the ensemble average of power is equal to $\int \Delta f(t)\Delta f(t)dt = R_f(0) = R_f(\tau)\forall\tau$, hence to its correlation function).

The variance of a signal is then written in function of its spectral density, again thanks to the Parseval theorem:

$$\sigma^2 = P(t) = \int S_f(f)df \tag{5.15}$$

Allowing for easy conversion from the frequency domain to the time domain, this relation allows us as well to characterize our frequency stability. Thus σ^2 is the quadratic average of a random frequency signal. Assuming this signal follows a gaussian law, one finds all associated results, like the signal has 98% probability to be in an interval of $f_0 \pm 3.02\sigma$, which one can use as the LOD definition.

There are two drawbacks though: in all rigor, the integral in equation 5.15 has an infinite integration domain. In practice, of course, one has to reduce this domain to a finite bandwidth, for example the resonator's bandwidth. Secondly, this variance expression does not converge for all negative exponents of the power law. In the quest for a less biased estimator, the Allan deviation was defined.

Allan variance

Experimentally, one never acquires an instantaneous signal, but its average over some integration time τ. In the case of the normalized frequency error $y(t)$: $\overline{y(\tau)} = \frac{1}{\tau}\int_{t_0}^{t_0+\tau} y(t)dt$. Also, the number of samples N is limited. The true variance is

$$\sigma^2 = \lim_{N\to+\infty}\lim_{\tau\to 0}\frac{1}{N}\sum_{i=1}^{N}\left(\overline{y(\tau)}_i - \frac{1}{N}\sum_{j=1}^{N}\overline{y(\tau)}_j\right)^2 \tag{5.16}$$

The determination of this variance demands an average ensemble of an infinite number of samples at the same time, (or from the same sample over an infinite duration). In practice, one can only compute an estimator of this variance from a finite number of samples and a finite time τ:

$$\sigma^2 \simeq \sigma^2(N,\tau) = \frac{1}{N}\sum_{i=1}^{N}\left(\overline{y(\tau)}_i - \frac{1}{N}\sum_{j=1}^{N}\overline{y(\tau)}_j\right)^2 \tag{5.17}$$

A known result in statistics (Vernotte 2006) says that the most probable variance corresponds to the following estimator:

$$\sigma'^2(N,\tau) = \frac{1}{N-1}\sum_{i=1}^{N}\left(\overline{y(\tau)}_i - \frac{1}{N}\sum_{j=1}^{N}\overline{y(\tau)}_j\right)^2 \tag{5.18}$$

This new quantity is itself a random variable one can characterize by its own variance, or more simply by a good estimator, that is its quadratic average, if one can reproduce its measurement on k paquets of N samples (overlapping or not):

$$\sigma^2_{\sigma'} = \frac{1}{k}\sum_{i=1}^{k}\sigma'^2_i(N,\tau) \tag{5.19}$$

The Allan deviation σ_y, or the two-sample variance is defined from equation 5.18 by choosing N=2:

$$\sigma^2_y(\tau) = \frac{1}{2}\frac{1}{k}\sum_{i=1}^{k}(\overline{y_{i+1}} - \overline{y_i})^2 \tag{5.20}$$

The Allan deviation then becomes the quadratic average of gaps between two consecutive measurements.

Allan's works showed that this variance can be expressed in the frequency domain:

$$\sigma^2_y(\tau) = 2\int_0^{+\infty} S_y(f)\frac{\sin^4(\pi\tau f)}{(\pi\tau f)^2}df \tag{5.21}$$

Beside obvious practical reasons, this expression justifies the use of $N = 2$ as it puts into light the fact that this variance converges for most of the power law exponents, and in particular for a white frequency noise (Vernotte 2006). Allan's works also show this estimator does not represent well white phase noise and shot noise ($\alpha = 1$ et $\alpha = 2$). It is best suited for long-term stability, that is low frequency noise.

A number of estimators were defined and are used (Picinbono, Hadamard...). They all give different results but provide for an "image" of each noise type. For all these reasons, a proper frequency stability estimation in the time domain for the nanomechanical devices should be one of those.

Bibliography

Abelé, N., Pott, V., Boucart, K., Casset, F., Séguéni, K., Ancey, P. & Ionescu, A. M. 2005 Comparison of RSG-MOSFET and capacitive MEMS resonator detection. *Electronics Letters* **41** (5), 3–4.

Aikele, M., Bauer, K., Ficker, W., Neubauer, F., Prechtel, U., Schalk, J. & Seidel, H. 2001 Resonant accelerometer with self-test. *Sensors and Actuators A: Physical* **92** (1-3), 161–167.

Alhazza, K. a., Daqaq, M. F., Nayfeh, A. H. & Inman, D. J. 2008 Non-linear vibrations of parametrically excited cantilever beams subjected to non-linear delayed-feedback control. *International Journal of Non-Linear Mechanics* **43**, 801–812.

Andreucci, P., Brianceau, P., Duraffourg, L., Hentz, S., Marcoux, C., Minoret, S., Myers, E. & Roukes, M. M. 2009 NEMS comprising ALSi alloy based transduction means - WO2011006885.

Arcamone, J., Niel, a., Gouttenoire, V., Petitjean, M., David, N., Barattin, R., Matheron, M., Ricoul, F., Bordy, T., Blanc, H., Ruellan, J., Mercier, D., Pereira-Rodrigues, N., Costa, G., Agache, V., Hentz, S., Gabriel, J., Baleras, F., Marcoux, C., Ernst, T., Duraffourg, L., Colinet, E., Myers, E., Roukes, M., Andreucci, P., Ollier, E. & Puget, P. 2011 VLSI silicon multi-gas analyzer coupling gas chromatography and NEMS detectors. *2011 International Electron Devices Meeting* (5), 29.3.1–29.3.4.

Arcamone, J., Van Den Boogaart, M. A. F., Serra-Graells, F., Fraxedas, J., Brugger, J. & Perez-Murano, F. 2008 Full-wafer fabrication by nanostencil lithography of micro / nanomechanical mass sensors monolithically integrated with CMOS. *Nanotechnology* **19**, 305302.

Ardito, R., Frangi, A., Corigliano, A., De Masi, B. & Cazzaniga, G. 2011 The effect of nano-scale interaction forces on the premature pull-in of real-life Micro-Electro-Mechanical Systems. *Microelectronics Reliability* **52** (1), 271–281.

Atalaya, J., Kinaret, J. & Isacsson, A. 2010 Nanomechanical mass measurement using non-linear response of a graphene membrane. *Europhysics Letters (EPL)* **91**, 48001.

Bargatin, I. 2008 High-frequency nanomechanical resonators for sensor applications. PhD thesis, California Institute of Technology.

Bargatin, I., Kozinsky, I. & Roukes, M. L. 2007 Efficient electrothermal actuation of multiple modes of high-frequency nanoelectromechanical resonators. *Applied Physics Letters* **90** (9), 093116.

Bargatin, I., Myers, E. B., Aldridge, J. S., Marcoux, C., Brianceau, P., Duraffourg, L., Colinet, E., Hentz, S., Andreucci, P. & Roukes, M. L. 2012 Large-scale integration of nanoelectromechanical systems for gas sensing applications. *Nano letters* **12** (3), 1269–74.

Bargatin, I., Myers, E. B., Arlett, J., Gudlewski, B. & Roukes, M. L. 2005 Sensitive detection of nanomechanical motion using piezoresistive signal downmixing. *Applied Physics Letters* **86** (13), 133109.

Barois, T., Ayari, A., Siria, A., Perisanu, S., Vincent, P., Poncharal, P. & Purcell, S. 2012 Ohmic electromechanical dissipation in nanomechanical cantilevers. *Physical Review B* **85**, 075407.

Bartsch, S. T., Lovera, A., Grogg, D. & Ionescu, A. M. 2012 Nanomechanical Silicon Resonators with Intrinsic Tunable Gain and sub-nW power consumption. *ACS nano* **6** (1), 256–264.

Bhave, S. A. 2004 Electrostatic Transduction for MEMS Resonators. PhD thesis, University of California, Berkeley.

Bianco, S., Cocuzza, M., Ferrero, S., Giuri, E., Piacenza, G., Pirri, C. F., Ricci, a., Scaltrito, L., Bich, D., Merialdo, a., Schina, P. & Correale, R. 2006 Silicon resonant microcantilevers for absolute pressure measurement. *Journal of Vacuum Science & Technology B: Microelectronics and Nanometer Structures* **24** (4), 1803.

Bordag, M., Klimchitskaya, G. & Mostepanenko, V. 1995 . *Physics Letters A* **200**, 95–102.

Braun, T., Ghatkesar, M. K., Backmann, N., Grange, W., Boulanger, P., Letellier, L., Lang, H.-p., Bietsch, A., Gerber, C. & Hegner, M. 2009 Quantitative time-resolved measurement of membrane protein-ligand interactions using microcantilever array sensors. *Nature Nanotechnology* **4**, 179–185.

Carr, D. W., Evoy, S., Sekaric, L., Craighead, H. G. & Parpia, J. M. 2000 Parametric amplification in a torsional microresonator. *Applied Physics Letters* **77** (10), 1545–1547.

Casimir, H. 1948 . *Kon. Ned. Akad. Wettenschan* **51** (793).

Chae, J., Kulah, H. & Najafi, K. 2004 An in-plane High-Sensitivity, Low-Noise Micro-g Silicon Accelerometer With CMOS Readout Circuitry. *Journal of Microelectromechanical Systems* **13** (4), 628–635.

Chang, H.-C. 2009 Ultrahigh-mass Mass Spectrometry of single biomolecules and bioparticles. *Annual Review of Analytical chemistry* **2**, 169–85.

Chaste, J., Eichler, A., Moser, J., Ceballos, G., Rurali, R. & Bachtold, A. 2012 A nanomechanical mass sensor with yoctogram resolution. *Nature Nanotechnology* **7**, 301–304.

Chen, C., Rosenblatt, S., Bolotin, K. I., Kalb, W., Kim, P., Kymissis, I., Stormer, H. L., Heinz, T. F. & Hone, J. 2009 Performance of monolayer graphene nanomechanical resonators with electrical readout. *Nature Nanotechnology* **4** (12), 861–867.

Chen, F., Harris, B., Roy, A. & Mohideen, U. 2002 . *International Journal of Modern Physics A* **17** (711).

Chiu, H.-y., Hung, P., Postma, H. W. C. & Bockrath, M. 2008 Atomic-Scale Mass Sensing Using Carbon Nanotube Resonators. *Nano Letters* **8** (12), 4342–4346.

Cleland, a. N. & Roukes, M. L. 2002 Noise processes in nanomechanical resonators. *Journal of Applied Physics* **92** (5), 2758.

Cochelin, B. 1994 A path-following technique via an asymptotic-numerical method. *Computers and Structures* **53**, 1181–1192.

Cochelin, B. & Vergez, C. 2009 A high order purely frequency-based harmonic balance formulation for continuation of periodic solutions. *Journal of Sound and Vibration* **324**, 243–262.

Colinet, E., Arcamone, J., Niel, A., Lorent, E., Hentz, S. & Ollier, E. 2010 100 MHz oscillator based on a low polarization voltage capacitive Lamé-mode MEMS resonator. In *International Frequency Control Symposium 2010*.

Colinet, E., Duraffourg, L., Labarthe, S., Hentz, S., Robert, P. & Andreucci, P. 2009 Self-oscillation conditions of a resonant nanoelectromechanical mass sensor. *Journal of Applied Physics* **105** (12), 124908.

Crespo da Silva, M. & Glynn, C. 1978 Nonlinear flexural-flexural-torsional dynamics of inextensional beams I. Equations of motion. *Journal of structural mechanics* **6** (4), 437–448.

Dalal, M. J., Fu, J. L. & Ayazi, F. 2011 Simultaneous dual-mode excitation of piezo-on-silicon micromechanical oscillator for self-temperature sensing. In *IEEE MEMS 2011*, pp. 489–492. Cancun, Mexico, January 23-27.

Defaÿ, E. 2007 Intégration de matériaux pérovskites dans la technologie silicium.

Defoort, M., Lulla, K., Heron, J., Bourgeois, O., Collin, E. & Pistolesi, F. 2011 Audio mixing in a tri-port nano-electro-mechanical device. *Applied Physics Letters* **233107**, 1–4.

Ding, J.-n., Wen, S.-z. & Meng, Y.-g. 2001 Theoretical study of the sticking of a membrane strip in MEMS under the Casimir effect. *Journal of Micromechanics and Microengineering* **11**, 202–208.

Djuric, Z. 2000 Mechanisms of noise sources in microelectromechanical systems. *Microelectronics Reliability* **40**, 919–932.

Dohn, S., Svendsen, W., Boisen, A. & Hansen, O. 2007 Mass and position determination of attached particles on cantilever based mass sensors. *Review of Scientific Instruments* **78**, 103303.

Dohn, S. r., Sandberg, R., Svendsen, W. & Boisen, A. 2005 Enhanced functionality of cantilever based mass sensors using higher modes. *Applied Physics Letters* **86**, 233501.

Duraffourg, L. & Andreucci, P. 2006 Casimir force between doped silicon slabs. *Physics Letters A* **359**, 406–411.

Duraffourg, L., Colinet, E., Ollier, E., Hentz, S., Andreucci, P., Reig, B. & Robert, P. 2008 Compact and explicit physical model for lateral metal-oxide-semiconductor field-effect transistor with nanoelectromechanical system based resonant gate. *Applied Physics Letters* **92** (17), 174106.

Durand, C. 2009 Développement de résonateurs électromécaniques en technologies Silicon On Nothing, à détection capacitive et amplifiée par transistor MOS, en vue d'une co-intégration permettant d'adresser une application de référence de temps. PhD thesis, Université des Sciences et Technologies de Lille.

Durand, C., Casset, F., Renaux, P., Abelé, N., Legrand, B., Renaud, D., Ollier, E., Ancey, P., Ionescu, A. M. & Buchaillot, L. 2008 In-Plane Silicon-On-Nothing Nanometer-Scale Resonant Suspended Gate MOSFET for In-IC Integration Perspectives. *IEEE Electron Device Letters* **29** (5), 494–496.

Ekinci, K. L., Huang, X. M. H. & Roukes, M. L. 2004*a* Ultrasensitive nanoelectromechanical mass detection. *Applied Physics Letters* **84** (22), 4469.

Ekinci, K. L. & Roukes, M. L. 2005 Nanoelectromechanical systems. *Review of Scientific Instruments* **76**, 061101.

Ekinci, K. L., Tang, Y. T. & Roukes, M. L. 2004*b* Ultimate limits to inertial mass sensing based upon nanoelectromechanical systems. *Journal of Applied Physics* **95** (5), 2682.

Ekinci, K. L., Yang, Y. T., Huang, X. M. H. & Roukes, M. L. 2002 Balanced electronic detection of displacement in nanoelectromechanical systems. *Applied Physics Letters* **81** (12), 2253.

Fanget, S., Hentz, S., Puget, P., Arcamone, J., Matheron, M., Colinet, E., Andreucci, P., Duraffourg, L., Myers, E. & Roukes, M. 2011 Gas sensors based on gravimetric detection - A review. *Sensors and Actuators B: Chemical* **160** (1), 804–821.

Feng, X. L., White, C. J., Hajimiri, a. & Roukes, M. L. 2008 A self-sustaining ultrahigh-frequency nanoelectromechanical oscillator. *Nature nanotechnology* **3** (6), 342–6.

Fong, K. Y., Pernice, W. H. P. & Tang, H. X. 2012 Frequency and phase noise of ultrahigh Q silicon nitride nanomechanical resonators. *Physical Review B* **85**, 161410.

Fraser, G. 2002 The ion detection efficiency of microchannel plates (MCPs). *International Journal of Mass Spectrometry* **215**, 13–30.

Gabrielson, T. 1993 Mechanical-thermal noise in micromachined acoustic and vibration sensors. *IEEE Transactions on Electron Devices* **40** (5), 903–909.

Genet, C., Lambrecht, A. & Reynaud, S. 2000 . *Physics Review A* **62** (012110).

Gil-santos, E., Ramos, D., Martinez, J., Fernandez-Regulez, M., Garcia, R., San Paulo, A., Calleja, M. & Tamayo, J. 2010 Nanomechanical mass sensing and stiffness spectrometry based on two-dimensional vibrations of resonant nanowires. *Nature Nanotechnology* **5**, 641–645.

Gouttenoire, V. 2009 Exploitation de nouveaux phénomènes dans les systèmes nanoélectromécaniques: réalisation d'un nanorésonateurs accordable. PhD thesis, Université Claude Bernard Lyon 1.

Gouttenoire, V., Barois, T., Perisanu, S., Leclercq, J.-L., Purcell, S. T., Vincent, P. & Ayari, A. 2010 Digital and FM demodulation of a doubly clamped single-walled carbon-nanotube oscillator: towards a nanotube cell phone. *Small (Weinheim an der Bergstrasse, Germany)* **6** (9), 1060–5.

Gui, C., Legtenberg, R., Tilmans, H. A. C., Fluitman, J. H. J. & Elwenspoek, M. 1998 Nonlinearity and Hysteresis of Resonant Strain Gauges. *Control* **7** (1), 122–127.

Guillon, S., Salomon, S., Seichepine, F., Dezest, D., Mathieu, F., Bouchier, A., Mazenq, L., Thibault, C., Vieu, C., Leïchlé, T. & Nicu, L. 2012 Biological functionalization of massively parallel arrays of nanocantilevers using microcontact printing. *Sensors and Actuators B: Chemical* **161**, 1135–1138.

Hagen, J. B. 1996 *Radio Frequency Electronics: Circuits and applications*. Cambridge University Press.

Hanay, M. S., Kelber, S., Naik, a. K., Chi, D., Hentz, S., Bullard, E. C., Colinet, E., Duraffourg, L. & Roukes, M. L. 2012 Single-protein nanomechanical mass spectrometry in real time. *Nature Nanotechnology* **7** (September), 602–608.

Hentz, S. 2010 Resonant piezoresistive detector having a resonator connected elastically to the supporting member of the detector, and process for manufacturing said detector. WO201234990.

Hentz, S., Duraffourg, L. & Colinet, E. 2008*a* Comparison of capacitive and frequential readout when scaling accelerometers down from Micro- to Nano- Electro Mechanical Systems. *arXiv* (1205.4860v).

Hentz, S., Duraffourg, L., Ollier, E., Andreucci, P., Colinet, E., Fontaine, H. & Robert, P. 2007 Importance of non-linearities and of proximity forces in NEMS design: modeling and experimental comparison. In *Invited conference to APCOM07 in conjunction with EPMESC XI, December 3-6, 2007, Kyoto, JAPAN*.

Hentz, S. & Kacem, N. 2010 Method and device for suppressing resonator hysteresis by simultaneous resonances. EP 2365282 - US 2011221301.

Hentz, S., Nguyen, V. & Robert, P. 2008*b* Resonant-beam accelerometer with rotating articulated lever arm. WO 2008/034788 A1.

Hierold, C. 2004 From micro- to nanosystems: mechanical sensors go nano. *Journal of Micromechanics and Microengineering* **14** (9), S1–S11.

Hung, L.-w. & Nguyen, C. T. 2011 Capacitive-Piezoelectric AlN resonators with Q>12000. In *IEEE MEMS 2011*, pp. 173–176. Cancun, Mexico, January 23-27.

Ivaldi, P., Abergel, J., Arndt, G., Robert, P., Andreucci, P., Blanc, H., Hentz, S. & Defaÿ, E. 2010 50nm thick AlN resonant micro-cantilever for gas sensing application. In *2010 IEEE International Frequency Control Symposium*, , vol. 95. Newport Beach, California, 1-4 June.

Ivaldi, P., Abergel, J., Blanc, H., Colinet, E., Myers, E. B., Roukes, M. L., Robert, P., Andreucci, P., Hentz, S. & Defaÿ, E. 2011*a* DMMP Vapor detection with 50nm thick AlN films based microcantilevers. In *Transducers 2011*. Beijing, June 5-9.

Ivaldi, P., Abergel, J., Matheny, M. H., Villanueva, L. G., Karabalin, R. B., Roukes, M. L., Andreucci, P., Hentz, S. & Defaÿ, E. 2011*b* 50 nm thick AlN film-based piezoelectric cantilevers for gravimetric detection. *Journal of Micromechanics and Microengineering* **21**, 085023.

Jensen, K., Kim, K. & Zettl, A. 2008 An atomic-resolution nanomechanical mass sensor. *Nature Nanotechnology* **3**, 533–537.

Jensen, K., Peng, H. & Zettl, A. 2006 Limits of Nanomechanical Resonators. In *IEEE ICONN 2006*, pp. 68–71.

Jiang, C., Chen, B., Li, J.-J. & Zhu, K.-D. 2011 Mass spectrometry based on a coupled Cooper-pair box and nanomechanical resonator system. *Nanoscale research letters* **6**, 570.

Juillard, J., Arndt, G. & Colinet, E. 2011 Modeling of Micromachined Beams Subject to Nonlinear Restoring or Damping Forces. *Journal of Microelectromechanical Systems* **20** (1), 165–177.

Juillard, J., Bonnoit, A., Avignon, E., Hentz, S. & Colinet, E. 2010 Large amplitude dynamics of micro-/nanomechanical resonators actuated with electrostatic pulses. *Journal of Applied Physics* **107** (1), 014907.

Kaajakari, V., Mattila, T., Oja, A. & Seppä, H. 2004 Nonlinear Limits for Single-Crystal Silicon Microresonators. *Journal of Microelectromechanical Systems* **13** (5), 715–724.

Kacem, N., Arcamone, J., Perez-Murano, F. & Hentz, S. 2010 Dynamic range enhancement of nonlinear nanomechanical resonant cantilevers for highly sensitive NEMS gas/mass sensor applications. *Journal of Micromechanics and Microengineering* **20** (4), 045023.

Kacem, N., Baguet, S., Dufour, R. & Hentz, S. 2011*a* Stability control of nonlinear micromechanical resonators under simultaneous primary and superharmonic resonances. *Applied Physics Letters* **98** (193507).

Kacem, N., Baguet, S., Duraffourg, L., Jourdan, G., Dufour, R. & Hentz, S. 2012*a* High order nonlinearity cancellation and pull-in suppression for ultrasensitive resonant nanoelectromechanical sensors. *Applied Physics Letters, under review* .

Kacem, N., Baguet, S., Hentz, S. & Dufour, R. 2011*b* Computational and quasi-analytical models for non-linear vibrations of resonant MEMS and NEMS sensors. *International Journal of Non-Linear Mechanics* **46** (3), 532–542.

Kacem, N., Baguet, S., Hentz, S. & Dufour, R. 2012*b* Pull-In Retarding in Nonlinear Nanoelectromechanical Resonators Under Superharmonic Excitation. *Journal of Computational and Nonlinear Dynamics* **7** (021011), 1–8.

Kacem, N. & Hentz, S. 2009 Bifurcation topology tuning of a mixed behavior in nonlinear micromechanical resonators. *Applied Physics Letters* **95**, 183104.

Kacem, N., Hentz, S., Fontaine, H., Nguyen, V., Delaye, M.-T., Blanc, H., Robert, P., Driot, N. & Dufour, R. 2008*a* From MEMS to NEMS : Modelling and characterization of the non linear dynamics of resonators , a way to enhance the dynamic range. In *8th World Congress on Computational Mechanics (WCCM8), 5th European Congress on Computational Methods in Applied Sciences and Engineering (ECCOMAS 2008)*. Venice, Italy.

Kacem, N., Hentz, S., Fontaine, H., Nguyen, V., Robert, P., Legrand, B. & Buchaillot, L. 2008*b* From MEMS to NEMS : Modelling and characterization of the non linear dynamics of resonators , a way to enhance the dynamic range. In *NSTI Nanotech 2008, Vol3*, pp. 619–622.

Kacem, N., Hentz, S., Pinto, D., Reig, B. & Nguyen, V. 2009 Nonlinear dynamics of nanomechanical beam resonators: improving the performance of NEMS-based sensors. *Nanotechnology* **20**, 275501.

Kacem, N., Sworowski, M., Hentz, S., Baguet, S. & Dufour, R. 2012*c* Sensitive detection of nonlinear nanomechanical motion using capacitive signal down-mixing for resonant M & NEMS inertial sensors. In *NSTI Nanotech 2012*. Santa Clara.

Karabalin, R. B., Matheny, M. H., Feng, X. L., Defay, E., Le Rhun, G., Marcoux, C., Hentz, S., Andreucci, P. & Roukes, M. L. 2009 Piezoelectric nanoelectromechanical resonators based on aluminum nitride thin films. *Applied Physics Letters* **95** (10), 103111.

Kenig, E., Lifshitz, R. & Cross, M. 2009 Pattern selection in parametrically driven arrays of nonlinear resonators. *Physical Review E* **79** (2), 1–10.

Kharrat, C., Colinet, E. & Voda, A. 2008 H-infinity Loop shaping control for PLL-based mechanical resonance tracking in NEMS resonant mass sensors. In *IEEE Sensors, 26-29 Oct. 2008*, pp. 1135 – 1138.

Knobel, R. & Cleland, A. N. 2002 Piezoelectric displacement sensing with a single-electron transistor. *Applied Physics Letters* **81** (12), 2258–2260.

Koskenvuori, M., Mattila, T., Häärä, A., Kiihamäki, J., Tittonen, I., Oja, A. & Seppä, H. 2004 Long-term stability of single-crystal silicon microresonators. *Sensors And Actuators A* **115**, 23–27.

Kozinsky, I., Postma, H. W. C., Bargatin, I. & Roukes, M. L. 2006 Tuning nonlinearity, dynamic range, and frequency of nanomechanical resonators. *Applied Physics Letters* **88** (25), 253101.

Kumar, V., Miller, J. K. & Rhoads, J. F. 2011 Nonlinear parametric amplification and attenuation in a base-excited cantilever beam. *Journal of Sound and Vibration* **330**, 5401–5409.

Lambrecht, A., Pirozhenko, I., Duraffourg, L. & Andreucci, P. 2007 The Casimir effect for silicon and gold slabs. *Europhysics Letters (EPL)* **77**, 44006.

Lamoreaux, S. 1997 . *Physics Review Letters* **75** (5).

Lamoreaux, S. 1998 . *Physical Review Letters* **81** (4549).

Lassagne, B., Garcia-Sanchez, D., Aguasca, A. & Bachtold, A. 2008 Ultrasensitive Mass Sensing with a nanotube electromechanical resonator. *Nano Letters* **8** (11), 3735–3738.

Lau, S. & Cheung, Y. 1981 Amplitude incremental variational principle for nonlinear vibration of elastic systems. *ASME journal of applied mechanics* **28**, 959–964.

Le Foulgoc, B. 2008 Evaluation du potentiel de performance de micro-accéléromètres inertiels vibrants en silicium. PhD thesis, Université Paris-EST.

Le Foulgoc, B., Bourouina, T., Traon, O. L., Bosseboeuf, A., Marty, F., Breluzeau, C., Grandchamp, J.-P. & Masson, S. 2006 Highly decoupled single-crystal silicon resonators: an approach for the intrinsic quality factor. *Journal of Micromechanics and Microengineering* **16** (6), S45–S53.

Le Traon, O., Janiaud, D., Lecorre, B., Pernice, M., Muller, S. & Tridera, J.-Y. 2005 Monolithic Differential Vibrating Beam Accelerometer within an Isolating System between the Two Resonators. In *Sensors (Peterborough, NH)*, pp. 648–651.

Le Traon, O., Janiaud, D., Muller, S. & Bouniol, P. 1998 The Via Vibrating Beam Accelerometer: concept and performances. In *Position, location and navigation symposium, April 20-23*. Palm Springs.

Lee, H. J., Park, K. K., Oralkan, O., Kupnik, M. & Khuri-yakub, B. T. 2008 CMUT as a Chemical Sensor for DMMP Detection. In *2008 IEEE International Frequency Control Symposium (2008)*, pp. 434–439.

Li, M., Myers, E. B., Tang, H. X., Aldridge, S. J., McCaig, H. C., Whiting, J. J., Simonson, R. J., Lewis, N. S. & Roukes, M. L. 2010 Nanoelectromechanical resonator arrays for ultrafast, gas-phase chromatographic chemical analysis. *Nano letters* **10** (10), 3899–903.

Li, M., Tang, H. X. & Roukes, M. L. 2007 Ultra-sensitive NEMS-based cantilevers for sensing, scanned probe and very high-frequency applications. *Nature nanotechnology* **2** (2), 114–20.

Lifshitz, R. & Cross, M. C. 2003 Response of parametrically driven nonlinear coupled oscillators with application to micromechanical and nanomechanical resonator arrays. *Physics Review B* **67** (13), 134302.

Lifshitz, R. & Cross, M. C. 2008 Nonlinear Dynamics of Nanomechanical and Micromechanical Resonators. In *Nonlinear Dynamics and Complexity*.

Lin, Y.-w., Lee, S., Li, S.-s., Xie, Y., Ren, Z. & Nguyen, C. T.-C. 2004 Series-Resonant VHF Micromechanical Resonator - References oscillators. *IEEE journal of solid state circuits* **39** (12), 2477–2491.

Mahmoodi, S. N., Jalili, N. & Daqaq, M. F. 2008 Modeling , Nonlinear Dynamics , and Identification of a Piezoelectrically Actuated Microcantilever Sensor. *IEEE/ASME transactions on mechatronics* **13** (1), 58–65.

Martin, F., Muralt, P., Dubois, M.-A. & Pezous, A. 2004 Thickness dependence of the properties of highly c-axis textured AlN thin films. *Journal of Vacuum Science & Technology A* **22** (2), 361–365.

Mile, E., Jourdan, G., Bargatin, I., Labarthe, S., Marcoux, C., Andreucci, P., Hentz, S., Kharrat, C., Colinet, E. & Duraffourg, L. 2010 In-plane nanoelectromechanical resonators based on silicon nanowire piezoresistive detection. *Nanotechnology* **21** (16), 165504.

Mohanty, P., Harrington, D., Ekinci, K., Yang, Y., Murphy, M. & Roukes, M. 2002 Intrinsic dissipation in high-frequency micromechanical resonators. *Physical Review B* **66** (8), 1–15.

Mostepanenko 2003 . *Physics Review D* **63**, 033402.

Naik, A. K., Hanay, M. S., Hiebert, W. K., Feng, X. L. & Roukes, M. L. 2009 Towards single-molecule nanomechanical mass spectrometry. *Nature Nanotechnology* **4**, 445–450.

Nayfeh, A. H. 1981 *Introduction to Perturbation Techniques*. New York: Wiley.

Nayfeh, A. H. & Mook, D. 1979 *Nonlinear oscillations*, physics an edn. John Wiley, New York.

Nayfeh, A. H. & Younis, M. I. 2005 Dynamics of MEMS resonators under superharmonic and subharmonic excitations. *Journal of Micromechanics and Microengineering* **15**, 1840–1847.

Nishiyama, H. & Nakamura, M. 1990 Capacitance of a strip capacitor. *IEEE Transactions on components, hybrids and manufacturing technology* **13** (2), 417.

Ollier, E., Dupré, C., Arndt, G., Arcamone, J., Vizioz, C., Duraffourg, L., Sage, E., Koumela, A., Hentz, S., Cibrario, G., Meininger, P., Benotmane, K., Marcoux, C., Rozeau, O., Billiot, G., Colinet, E., Andrieu, F., Philippe, J., Aussenac, F.,

Mercier, D., Blanc, H., Ernst, T. & Robert, P. 2012 Ultra-scaled high-frequency single-crystal Si NEMS resonators and their front-end co-integration with CMOS for high sensitivity applications. In *IEEE MEMS 2012*. Paris, 29 January-2 February.

Park, J., Qin, H., Scalf, M., Hilger, R. T., Westphall, M. S., Smith, L. M. & Blick, R. H. 2011 A Mechanical Nanomembrane Detector for Time-of-Flight Mass Spectrometry. *Nano Letters* **11**, 3681–3684.

Parkin, J. D. & Hähner, G. 2011 Mass determination and sensitivity based on resonance frequency changes of the higher flexural modes of cantilever sensors. *Review of Scientific Instruments* **82**, 035108.

Pinto, D. 2009 Caractérisation électrique d'accéléromètres résonants de type NEMS. PhD thesis, Conservatoire National des Arts et Métiers.

Pinto, D., Mercier, D., Kharrat, C., Colinet, E., Nguyen, V., Reig, B. & Hentz, S. 2009 A Small and High Sensitivity Resonant Accelerometer. In *Proceedings of the Eurosensors XXIII Conference, September 2009*, , vol. 33, pp. 536–539. Lausanne, Switzerland.

Postma, H. W. C., Kozinsky, I., Husain, A. & Roukes, M. L. 2005 Dynamic range of nanotube- and nanowire-based electromechanical systems. *Applied Physics Letters* **86**, 223105.

Rantakari, P., Kaajakari, V., Mattila, T., Kiihamaki, J., Oja, A., Tittonen, I. & Seppa, H. 2005 Low noise, low power micromechanical oscillator. In *Transducers05*, pp. 35–38. Seoul, Korea.

Rinaldi, M., Zuniga, C., Zuo, C. & Piazza, G. 2011 GHz range nanoscaled AlN contour-mode resonant sensors (CMR-S) with self-sustained CMOS oscillator. In *Solid-state Sensors, actuators and microsystems workshop*, pp. 10–13. Hilton head Island, South Carolina, June 6-10.

Robert, P. & Hentz, S. 2009 Sensor for in-plane piezoresistive detection, WO2011048132.

Robert, P., Nguyen, V., Hentz, S., Duraffourg, L., Jourdan, G., Arcamone, J. & Harrisson, S. 2009 M&NEMS: A new approach for ultra-low cost 3D inertial sensor. *2009 IEEE Sensors* pp. 963–966.

Robins, W. P. 1984 *Phase noise in signal sources. Theory and applications*. Institution of Electrical Engineers.

Rubiola, E. 2009 *Phase noise and frequency stability in oscillator*. The cambridge RF and microwave engineering series.

Rugar, D. & Grütter, P. 1991 Mechanical parametric amplification and thermomechanical noise squeezing. *Physical Review Letters* **67** (6).

Sazonova, V., Yaish, Y., Ustünel, H., Roundy, D., Arias, T. a. & McEuen, P. L. 2004 A tunable carbon nanotube electromechanical oscillator. *Nature* **431** (7006), 284–7.

Schmid, S., Dohn, S. r. & Boisen, A. 2010 Real-Time Particle Mass Spectrometry Based on Resonant Micro Strings. *Sensors* **10**, 8092–8100.

Serry, F. M., Dirk, W. & Maclay, G. J. 1998 The role of the Casimir effect in the static deflection and stiction of membrane strips in microelectromechanical systems (MEMS). *Journal of Applied Physics* **84** (5).

Seshia, A. a., Palaniapan, M., Roessig, T., Howe, R., Gooch, R., Schimert, T. & Montague, S. 2002 A vacuum packaged surface micromachined resonant accelerometer. *Journal of Microelectromechanical Systems* **11** (6), 784–793.

Shao, L. C., Wong, C. L. & Palaniapan, M. 2008 Study of the nonlinearities in micromechanical clamped-clamped beam resonators using stroboscopic SEM. *Journal of Micromechanics and Microengineering* **18**, 085019.

Sinha, N., Wabiszewski, G. E., Mahameed, R., Felmetsger, V. V., Tanner, S. M., Carpick, R. W. & Piazza, G. 2009 Piezoelectric aluminum nitride nanoelectromechanical actuators. *Applied Physics Letters* **95** (5), 053106.

Stachiv, I., Fedorchenko, a. I. & Chen, Y.-L. 2012 Mass detection by means of the vibrating nanomechanical resonators. *Applied Physics Letters* **100**, 093110.

Sundaresan, K., Ho, G. K., Pourkamali, S. & Ayazi, F. 2006 A Low Phase Noise 100MHz Silicon BAW Reference Oscillator. In *IEEE 2006 Custom Integrated Circuits Conference*, pp. 841–844.

Tanaka, K. 2003 The Origin of Macromolecule Ionization by Laser Irradiation (Nobel Lecture). *Angewandte Chemie International Edition* **42**, 3860–3870.

Tilmans, H. A. C. & Legtenberg, R. 1994 Electrostatically driven vacuum-encapsulated polysilicon resonators Part II. Theory and performance. *Sensors & Actuators: A. Physical* **45**, 67–84.

Turner, K. L., Miller, S. A., Hartwell, P. G., Macdonald, N. C., Strogatz, S. H. & Adams, S. G. 1998 Five parametric resonances in a microelectromechanical system. *Nature* **396**, 149–152.

Vernotte, F. 2006 Stabilité temporelle et fréquentielle des oscillateurs: outils d'analyse. In *Techniques de l'ingénieur*, p. R681.

Villanueva, L. G., Karabalin, R. B., Matheny, M. H., Kenig, E., Cross, M. C. & Roukes, M. L. 2011 A nanoscale parametric feedback oscillator. *Nano letters* **11** (11), 5054–9.

Walter, B. 2011 Fabrication de micro-résonateurs haute fréquence pour la microscopie à force atomique sur des objets biologiques. PhD thesis, Université des Sciences et Technologies de Lille.

Wong, A.-C., Ding, H. & Nguyen, C. T.-C. 1998 Micromechanical mixer and filters. In *International Electron Devices Meeting 1998. Technical Digest (Cat. No.98CH36217)*, pp. 471–474. Ieee.

Yang, Y. T., Ekinci, K. L., Huang, X. M. H., Schiavone, L. M., Roukes, M. L., Zorman, C. a. & Mehregany, M. 2001 Monocrystalline silicon carbide nanoelectromechanical systems. *Applied Physics Letters* **78** (2), 162.

Yazdi, N., Kulah, H. & Najafi, K. 2004 Precision Readout Circuits for Capacitive Microaccelerometers. In *IEEE Sensors, 2004, 24-27 Oct*, pp. 28–31.

Younis, M. I., Abdel-Rahman, E. M. & Nayfeh, A. 2003 A Reduced-Order Model for Electrically Actuated Microbeam-Based MEMS. *Journal of Microelectromechanical Systems* **12** (5), 672–680.

Zuo, C., Spiegel, J. V. D. & Piazza, G. 2011 Switch-less dual-frequency reconfigurable CMOS oscillator using one single piezoelectric ALN MEMS resonator with Co-existing S0 and S1 Lamb-wave modes. In *IEEE MEMS 2011*, pp. 177–180. Cancun, Mexico.